Central nervous system atlas of larval zebrafish based on the morphology of single excitatory and inhibitory neurons

Xu-Fei Du[1,2,5,]*, Zhi-Feng Yue[1,5], Ming-Quan Chen[1], Wan-Lan Li[1], Tian-Lun Chen[1,2], Han-Yang Hu[1], Hong-Li Wan[1], Ting-Ting Zhao[1], Yong-Wei Zhong[1], Xin-Yu Ning[1], Xiu-Dan Zheng[1], Hong-An Ren[1], Rui-Qi Wang[1], Rong Zhao[1], Xiao-Lan Peng[1], Zhi-Ming Jia[1], Chen-Xi Jin[1], Jia-Wen Huang[1], Wei Deng[1], Liu-Qin Qian[1], Li Wang[1], Mei-Yu Zheng[1], Wei Zhang[1], Xiao-Yu Shen[1], Xiu-Lian Shen[1], Xiao-Ying Qiu[1], Qi-Meng Zhao[1,2], Dan-Yang Li[1,2], Li-Jun Chen[1,3], Si-Jia Wang[1,2], Yu-Chen Gong[1,2], Yan Li[1], Yu Mu[1,2], Peng Ji[4], Jie He[1,2], Yu-Fan Wang[1,2] & Jiu-Lin Du[1,2,3,]*

[1] Institute of Neuroscience, Key Laboratory of Brain Cognition and Brain-Inspired Intelligence Technology, Center for Excellence in Brain Science and Intelligence Technology, Chinese Academy of Sciences, 320 Yue-Yang Road, Shanghai 200031, China

[2] University of Chinese Academy of Sciences, 19A Yu-Quan Road, Beijing 100049, China

[3] School of Life Science and Technology, ShanghaiTech University, 319 Yue-Yang Road, Shanghai 200031, China

[4] Institute of Science and Technology for Brain-Inspired Intelligence, Fudan University, Shanghai, China.

[5] These authors contributed equally

* These authors jointly supervised this work: Xu-Fei Du (xufeidu@ion.ac.cn), Jiu-Lin Du (forestdu@ion.ac.cn)

Comprehensive single-neuron morphology mapping is fundamental to deciphering the brain architecture and function. While invertebrate animal models including *Caenorhabditis elegans* and *Drosophila melanogaster* have achieved complete neuronal maps primarily via electron microscopy reconstructions[1–8], vertebrate efforts remain limited in spatial coverage and/or lack of cell type annotation[9–18]. Here, we present a nervous system-wide, cellular-resolution neuronal morphology atlas for the vertebrate animal model of larval zebrafish, annotated with excitatory (E) and inhibitory (I) neurotransmitter identity and dendrite-axon polarity. The dataset, collected from over 13,400 individual animals, encompasses more than 20,000 neurons spanning the brain, spinal cord, and peripheral ganglia (covering ~ 25% of all E and I neurons in the brain), all integrated into a whole-body common physical space with detailed neuroanatomical parcellations. It reveals over 500 hierarchically classified neuronal morphotypes and enables the construction of directed and weighted inter-cell-type and interregional connectomes, bridging large-scale cellular anatomy with circuit- and system-level organization across spatial scales. Neuronal projection analyses reveal differences between E and I neurons in ipsilateral-contralateral and ascending-descending projection preferences, the combination of projection modes for bilateral innervation, and the modular organization of projection patterns. Network analyses identify structured connectivity motifs, network hubs, and characteristic multimodal sensorimotor pathways. Hosted on the open interactive platform ZExplorer, this resource enables exploration, querying, and integration of multimodal neural data, laying a foundation for understanding functional circuits, developing models, and conducting hypothesis-driven research of the zebrafish brain.

The nervous system, the most complex system in the body, controls how animals sense, represent, and respond to both external and internal worlds through its intrinsic organization and connections with other body parts. This control depends on a myriad of elements and their interactions in this complex system. Since Santiago Ramón y Cajal first identified the neuron as the fundamental unit of the nervous system and proposed the concept of unidirectional information flow through neural circuits[19], it has remained a challenge to understand how the nervous system is organized, both structurally and functionally, and particularly in terms of the relationship between structure and function[20,21]. To tackle this challenge, a critical step is to elucidate the connectome at meso- and microscopic levels, i.e., the comprehensive map of neuron types and their connections.

Over the past decade, advances in light microscopy (LM) and electron microscopy (EM) techniques have enabled extensive efforts to map the connectome of the nervous system by acquiring large-scale structural datasets at cellular or synaptic resolution across various model organisms. For example, whole-body EM connectomes have been reconstructed for adult

nematode *Caenorhabditis elegans*. For *Drosophila melanogaster*, LM-based reconstructions have captured the single-cell morphologies of ~16,000 neurons[4], and full synaptic-resolution EM reconstructions of all neurons in the central brain have been achieved[5–8]. Given the distinct organization of vertebrate and invertebrate nervous systems, connectome mapping in vertebrates is important for advancing our understanding of vertebrate brains. In recent years, substantial progress has been made in reconstructing single-neuron morphologies in the mouse brain: reconstruction time has been reduced from days to hours per neuron, and the number of reconstructed neurons has increased from dozens to ten thousand[12–15]. Nevertheless, due to the large number of neurons (~70 million in the mouse brain) and their morphological complexity, current efforts primarily focus on mapping brain-wide projections of neurons located in a limited number of specific brain regions. Achieving a comprehensive dataset that captures 'whole-brain neurons with whole-brain projections' in vertebrates remains a significant challenge[22–26].

Among vertebrate models, the larval zebrafish (*Danio rerio*) is phylogenetically well positioned and possesses a compact brain, making it ideal for whole-brain connectome mapping. With a scale of one hundred thousand neurons, its brain preserves conserved neurotransmitter types and neuroanatomical regions found in higher vertebrates[27]. Its optical transparency and a wealth of genetic tools[28] make it uniquely suited for live whole-brain structural and functional imaging at single-cell resolution by LM[29–31]. Its small brain volume (< 0.1 mm^3) also facilitates intact-tissue three-dimensional (3D) *in situ* RNA sequencing[32,33] and whole-brain serial-section EM[10,11,34,35]. Combining LM and EM through cross-modality registration[36–38] opens the door to developing an integrative structural-functional connectome with cell type identity, offering a foundation for constructing mechanistic theories and models of vertebrate brain functions. Consequently, the larval zebrafish is widely regarded as a highly promising model for uncovering nervous system organization in vertebrates. Recent LM- and EM-based reconstructions have enabled progress in zebrafish connectome, though existing datasets remain limited in scope and completeness. A pioneering LM-based dataset encompasses 2,143 neurons located exclusively in the brain[9]. EM studies have been constrained either by a lack of requisite synaptic resolution for reconstruction[39] or by incomplete reconstruction of neurons and their connectivity[10,11]. Furthermore, these reported LM and EM datasets do not contain neurotransmitter identity, which is indispensable for a comprehensive understanding of connectome organization.

In this study, we built a whole-nervous-system single-neuron morphology atlas of excitatory (E) and inhibitory (I) neurons in larval zebrafish at 6 days post-fertilization (dpf). First, we established a common physical space (CPS) of the whole nervous system for multimodal data integration and parcellated the entire brain, spinal cord (SC), and peripheral ganglia in 3D. We mapped the cytoarchitecture of E and I neurons and reconstructed the morphologies of over 20,000 individual neurons—covering approximately 25% of all E and I

neurons in the larval zebrafish brain—across both the central and peripheral nervous systems, collected from more than 13,000 individual animals. At the mesoscale, we annotated neurons with dendrite-axon polarity and hierarchical morphotypes, uncovered projection design rules, and constructed a morphotype-based connectome for circuit mining. At the macroscale scale, we constructed directed and weighted interregional E and I connectomes and identified connectivity motifs, network hubs, and sensorimotor pathways across the nervous system. All reference transgenic patterns, region parcellations, cytoarchitectures, and single-neuron morphology reconstructions are available via an interactive online platform (ZExplorer: https://zebrafish.cn/LM-Atlas/EI), which supports 3D visualization as well as location- and projection-based neuron querying and exploration.

Generating a larval zebrafish body-wide CPS with the nervous system parcellated

To build the single-neuron projectome, a cellular-resolution 3D reference atlas is essential for integrating data originating from individual animals. We therefore constructed a larval zebrafish CPS via generating a two-channel volumetric average template from 16 live double transgenic zebrafish *Tg(elavl3:H2B-GCaMP6s)jf5;TgBAC(vglut2a:LOXP-DsRed-LOXP-GFP)ion18h* at 6 dpf. In this line, all neurons express nuclear GCaMP6s driven by the pan-neuronal promotor *elavl3* and the majority of excitatory glutamatergic neurons express cytosolic DsRed driven by the glutamatergic neuronal promotor *vglut2a* (Fig. 1a). Images were acquired at 0.62 × 0.62 × 1 μm^3 and resampled to 1 × 1 × 1 μm^3 for generating the template. We used the symmetric groupwise normalization (SyGN) algorithm in the multivariate template construction tool of the advanced normalization tools (ANTs)[40]. The SyGN method permits concurrent and unbiased generation of an average image for each channel from the corresponding input population through iteration (Extended Data Fig. 1a,b). The resulting CPS contains two original reference templates: pan-neuronal (nuclear) and excitatory glutamatergic (cytosolic) (Fig. 1a), providing two options for subsequent data integration. These templates cover the entire brain, spinal cord (SC) segments 1–11, peripheral ganglia, and body structures inferred from autofluorescence signals on the skin, jaw, eye, ear, and fin. The template dimensions are approximately 636 (left to right) × 1,860 (rostral to caudal) × 360 (dorsal to ventral) voxels, with the nervous system occupying ~64.5 million voxels and the brain ~41.9 million voxels.

To establish standard neuroanatomical parcellations within the CPS, we registered 702 reference expression patterns (Supplementary Table 1) to the CPS to delineate brain regions and nuclei. We first generated reference templates for excitatory, inhibitory, and neuromodulatory neuronal populations, which provide important reference information for anatomical annotation. These include an additional excitatory population labeled by *TgBAC(vglut2b:GAL4FF)ion123d*, two inhibitory populations labeled by

TgBAC(gad1b:GAL4-VP16)ion19h and *Tg(glyt2:GFP)cf3*, and the monoaminergic population labeled by *Tg(vmat2:GFP)pku2* (Fig. 1b, Extended Data Fig. 1c,d, and Supplementary Video 1; see Methods). These templates were generated by creating two-channel averages, using *vglut2a:DsRed* in one channel as a bridge to anchor their alignment to the CPS. To further enrich neuroanatomical information, we incorporated atlas data from Z-Brain (24 lines)[41], ZBB (245 lines)[28,42], and mapzebrain (428 lines)[9,43], yielding a total of 697 expression patterns covering various data types, including enhancer trap, transgene, immunostaining, *in situ* hybridization, and dye backfill (Supplementary Table 1; https://zebrafish.cn/LM-Atlas/EI). We optimized a unified set of ATNs registration parameters that enabled robust alignment between live scans (our ZExplorer and ZBB), fixed scans (Z-Brain and mapzebrain), and between live and fixed scans (see Methods). Based on mean landmark distances (MLDs) derived from six expression patterns, the inter-atlas registration precision between our ZExplorer and other atlases was 7.23 ± 2.29 μm (Extended Data Fig. 1e–k; see Methods). This level of precision is close to the average neuron diameter in larval zebrafish (5.80 ± 0.001 μm; see below).

Guided by the integrated expression pattern atlases, we manually parcellated the nervous system into non-overlapping, gap-free 3D anatomical segments with smooth boundaries (see Methods). Referring to the brain ontologies in Mueller and Wullimann's early zebrafish brain atlas[27] and in the Z-Brain[41], we annotated 68 hierarchically organized neuroanatomical regions, including 54 brain structures, 5 regions for each SC segment, and 9 peripheral ganglia (Fig. 1c–e, and Supplementary Video 2). Accounting for bilateral pairs of certain regions across hemispheres and for multiple SC segments, we obtained a total of 173 regions, including 78 central brain regions and 77 spinal regions (within 11 vertebrae) in the central nervous system (CNS), as well as 18 peripheral ganglia in the peripheral nervous system (PNS). Relevant region information and the reference templates used for delineation are summarized in Supplementary Table 2.

Taken together, these efforts yield a body-wide larval zebrafish CPS with detailed 3D annotations of the nervous system's anatomical structures, forming a foundational spatial framework for single-neuron morphology mapping.

Generating cytoarchitecture atlases of E and I neurons

To map the cytoarchitecture of E and I neurons, we examined their numbers and spatial distributions throughout the nervous system at 6 dpf using the above-mentioned transgenic lines, in which E or I neurons are fluorescently labeled. The marker genes used included the vesicular glutamate transporter genes *vglut2a* (i.e., *slc17a6b*) and *vglut2b* (i.e., *slc17a6a*) for glutamatergic E neurons, the glutamic acid decarboxylase gene *gad1b* for GABAergic I neurons, and the glycine transporter gene *glyt2* for glycinergic I neurons. The total neuronal

population was mapped using the *Tg(elavl3:Hsa.H2B-GCaMP6s)jf5*. For each group, four larvae were imaged, and all labeled neuronal somata were manually identified and localized within the brain, SC and peripheral regions. Each expression pattern was either directly registered into the CPS or trans-registered via co-scanning with one of the two original reference lines used for CPS construction (see Fig. 1a). Digitized neuronal positions were then aligned to the CPS to build cytoarchitecture atlases for the total neuronal population (*elavl3*+), excitatory neurons (*vglut2a/2b*+), GABAergic neurons (*gad1b*+), and glycinergic neurons (*glyt2*+) (Fig. 2a, and Supplementary Video 3).

Quantification revealed that the nervous system contains 122,139 ± 4,171 *elavl3*+ neurons, including ~49,000 excitatory neurons (*vglut2a*+: 39,495 ± 2,755; *vglut2b*+: 9,646 ± 194) and ~27,000 inhibitory neurons (*gad1b*+: 21,956 ± 625; *glyt2*+: 5,227 ± 398), yielding an overall E:I ratio of ~1.8:1. E and I neurons together accounted for ~63% of all neurons, implying the presence of other types of neurons and/or incomplete coverage by transgenic labeling. The neurons in the retina were not included in the quantification. We then mapped these neurons to parcellated anatomical regions in the CPS and analyzed their distributions across the CNS (including the telencephalon (Tel), diencephalon (Di), midbrain (M), hindbrain (H), and SC) and the PNS (primarily the peripheral ganglia (G)) (Fig. 2b). Excitatory neurons were present in both the CNS and PNS, while GABAergic neurons were found predominantly in the CNS and glycinergic neurons in the hindbrain and SC. Notably, the numbers of total (*elavl3*+), excitatory (*vglut2a*+ and *vglut2b*+), and inhibitory (*gad1b*+ and *glyt2*+) neurons progressively increased along the anteroposterior (AP) axis from the telencephalon to hindbrain. We also calculated the regional proportions of E and I neurons relative to the total *elavl3*+ population. The average proportion was 53 ± 3%, with lower values observed in the preoptic area (Po), superior and inferior raphe (SR and IR), and rostral/caudal hypothalamus (Hr and Hc) (Fig. 2c), consistent with these regions containing diverse types of neuromodulatory, neuropeptidergic, or neuroendocrine-related neurons.

Besides cell numbers, we examined cell densities (neurons per 30^3 μm^3) across the nervous system. Among primary nervous system subdivisions (Tel, Di, M, H, SC, G), both E and I neuron densities showed distinct patterns: *vglut2a/2b* neurons were generally enriched in the Tel, M, H, and G; *gad1b*+ cells peaked in the midbrain; and *glyt2* neurons were most abundant in the SC (Fig. 2d). Additionally, significant variations in neuron densities were observed both within and between E and I neuronal populations across regions (Fig. 2e; $P < 0.001$). To further characterize functional balance, we compared E over I cell dominance, calculated as $(N_E-N_I)/(N_E+N_I)$ (N denotes cell number), across the nervous system. At the level of subdivisions (Fig. 2f), while I neurons dominated in the SC, E neurons dominated in

both the brain and peripheral ganglia, with a decreasing gradient of E dominance from Tel to Di to M. At the level of regions (Fig. 2g), some brain regions showed balanced E and I populations, such as the tectal periventricular cell layer (PL) and the nucleus of the medial longitudinal fasciculus (nMLF) involved in sensorimotor processing, while some exhibited I dominance, such as the tectal neuropil layers (NL), pretectum (Pr), tegmentum (T), and interpeduncular nucleus (IPN).

In summary, the number of E and I neurons gradually increases along the AP axis in the brain, with E dominance gradually shifting to I dominance from the brain to the SC.

Atlasing nervous system-wide single E and I neuron morphology

To systematically map the morphology of single E and I neurons across the nervous system, we utilized the inherent mosaicism of transient transgenesis for stochastic sparse labeling. We injected a mixture containing an activator (*tissue-specific promoter:GAL4*), an effector (*UAS:membrane-bound fluorescent protein*), and *Tol2* transposase mRNA into one cell at the 16-cell stage. This approach resulted in stable fluorescent protein expression in only one or a few neurons that are random subsets of the overall GAL4 expression pattern. Labeling density can be tuned by adjusting the amount of injected plasmids. We term this sparse labeling method genetic live "Golgi-Staining" via Transient Expression of Microinjected Plasmids (gSTEMP).

Injected embryos carried the *elavl3:H2B-GCAMP6s* transgene, which serves as a registration reference and fluoresces differently from the neuron-labeling reporter *tdTomato*. 6-dpf larvae with appropriate sparse labeling were live-imaged using confocal microscopy (voxel size $0.5 \times 0.5 \times 1\ \mu m^3$) across three partially overlapping horizontal stacks covering the head and upper trunk. These stacks were stitched into a single volume, and the green channel (*elavl3:H2B-GCAMP6s*) was registered to the CPS using ANTs through a two-step transformation: (1) rigid and affine (RA), followed by (2) nonlinear warp registration. We used the red channel with neuron-morphology labeling to perform semi-manual neuronal morphology reconstruction and aligned individual digitized neuronal skeletons to the CPS by applying the matrices from the two-step transformation (Fig. 3a and Supplementary Video 4; see Methods).

For large-scale labeling of E and I neurons, we primarily used *vglut2a*, *vglut2b*, *gad1b*, and *glyt2* as gene markers. To increase coverage of specific neuronal populations, we additionally employed *isl2b* and *atoh7* for retinal ganglion cells (RGCs, excitatory neurons), and *cbln12* and *cpce* respectively for granule (excitatory neurons) and Purkinje cells (inhibitory neurons) (see Methods). Using a standardized workflow involving sparse neuron labeling, live imaging, neuron reconstruction, and image registration, we built a single-neuron morphology atlas comprising 20,011 E and I neurons (n_E = 12,219, n_I = 7,792; excitatory: $n_{vglut2a/2b}$ = 11,150, n_{cbln12} = 558, $n_{isl2b/atoh7}$ = 511; inhibitory: n_{gad1b} = 5,371, n_{cpce} = 228, n_{glyt2} =

2,193) distributed almost uniformly between hemispheres (n_{left} = 9,962, n_{right} = 10,049), covering the entire central brain (including the retina), partial SC, and peripheral ganglia (Fig. 3b–e and Supplementary Video 5). This dataset covers over 25% of the ~76,000 (see the cytoarchitecture results) E and I neurons in the entire nervous system (excluding the retina) of 6-dpf larval zebrafish. For subsequent analyses, additional markers *isl2b*, *atoh7*, and *cbln12* were integrated into the *vglut2a/2b* group, and *cpce* into the *gad1b* group, ensuring a unified representation of excitatory and GABAergic inhibitory neuron populations.

To validate the registration precision of the reconstructed morphology atlas, we randomly selected 88 fish scans and measured alignment accuracy using a landmark-based approach[44] (see Methods). The resulting MLD across samples was 3.28 ± 0.06 μm (range: 2.2–4.8 μm), which is below the average neuronal diameter in larval zebrafish (5.80 ± 0.001 μm, measured from 20,011 reconstructed neurons), demonstrating cellular-resolution precision (Extended Data Fig. 2a–f; see Methods). We also applied normalized cross correlation (NCC) as a registration quality metric (see Methods), and observed no correlation between NCC and landmark-based registration precision (P = 0.1067). This suggests that landmark evaluation provides a more definitive assessment, while NCC is more suitable for detecting gross misalignments (Extended Data Fig. 2g,h).

To evaluate the unbiasedness of cell sampling, we compared regional distributions of sampled neurons with those of complete neurons in the E and I cytoarchitecture atlases (see Fig. 2a-c). For both E and I neuronal populations, we observed strong correlations (Fig. 3f and Extended Data Fig. 3a–f; *vglut2a/2b*: r = 0.72; *gad1b*: r = 0.84; *glyt2*: r = 0.81; all P < 0.001), suggesting unbiased sampling. We further assessed this by performing 1,000 rounds of random subsampling at varying sizes from the reconstructed neuron pools and analyzing the resulting regional distribution correlations. Even with sampling size of only hundreds of cells, the correlation showed comparable in significance to those obtained at larger sample sizes (Extended Data Fig. 3g), further supporting the highly stochastic sampling achieved by our gSTEMP approach.

In summary, we establish a single-neuron morphology atlas that is annotated with E and I neurotransmitter identities and covers neurons throughout the retina, brain, SC, and PNS areas. Besides neurites within the CNS, the whole body-wide template allows the alignment of neurites from cranial sensory and motor neurons that extend beyond the brain and SC. Therefore, this comprehensive atlas enables the mining of neural circuit pathways from sensory inputs to motor outputs at a whole-body scale.

General morphological and projection features of E and I neurons

We next characterized the morphology of E and I neuronal populations. From *vglut2a/2b* to *gad1b* to *glyt2* neurons, the number of branch points decreased, while the maximum branch

order increased slightly, implying different branching patterns among these three types of neurons (Fig. 4a–c). *vglut2a/2b* neurons were larger in size than both I neuronal populations, as revealed by the total cable length and maximum Euclidian distance from the soma (Fig. 4a,d,e). Among I populations, *glyt2* neurons were larger than *gad1b* neurons (Fig. 4d,e), consistent with their role in connecting hindbrain and SC structures to upper brain regions (see Fig. 3d, typical case). At the population level, the total length positively correlated with the number of branch points, suggesting an interrelation between neuronal size and structural complexity (Fig. 4f). In accordance, the larger the size of the neurites (*vglut2a/2b* > *glyt2* > *gad1b*), the more regions they innervated (Fig. 4g).

To analyze the features of axonal innervation (projection), we annotated the input-output domains of neurites, namely the polarized dendritic and axonal compartments (DA). We inferred the polarity of each branch using a machine-learning algorithm. It was designed and trained based on biological datasets in which axons were identified by the localization of the presynaptic marker protein synaptophysin (Sypb). Specifically, we generated a bidirectional UAS reporter plasmid *Sypb-EGFP-tdKatushka2-CAAX* to simultaneously label the morphology and presynaptic sites of individual neurons (Extended Data Fig. 4a,c,e; see Methods). We applied the gSTEMP method on larvae carrying the *elavl3:H2B-TagBFP* transgene, which differs in fluorescence from the sparsely labeled neurons and has the same nucleus-locating expression pattern as *elavl3:H2B-GCaMP6s*. This provided a bridging channel for accurate registration.

We reconstructed and aligned dozens of cells with DA and presynaptic site annotations for the *vglut2a*, *gad1b*, and *glyt2* neuronal populations (Extended Data Fig. 4b,d,f). Based on these reconstructions, we found three common alternative features that allow the identification of dendritic and axonal compartments of projection neurons: (1) dendrites and axons emerge from the soma as separate primary branches (bipolar or multipolar); (2) a single fiber originating from the soma bifurcates immediately into one dendritic and one axonal arbor (pseudounipolar); or (3) a single fiber extends from the soma and undergoes multiple bifurcations before producing a relatively long daughter branch that forms the axonal arbor stem. We then extracted a set of structural features and developed a machine-learning algorithm to automatically classify the DA compartments of each projection neuron in the large-scale E and I neuron datasets (see Methods). Following automated DA identification, we evaluated its performance using both the training dataset and 12 MBLAST-defined morphotypes with known polarity (Extended Data Fig. 4g-i; see below in Fig. 5 and Extended Data Figs. 5 and 6), achieving accuracies of 93% and 92–100%, respectively. The accuracy is expected to improve with additional ground-truth training data from diverse neuronal subtypes. To ensure reliability, all DA classifications were further manually reviewed and validated across all morphotypes. In total, we validated and annotated 18,615 neurons with DA polarity.

With this DA-annotated single-neuron-morphology dataset, we first obtained a global view of DA (input-output) distribution patterns across the E and I neuronal populations. We extracted all node points along dendritic and axonal branches, and transformed the points into density to visualize the DA distribution map (Fig. 4h,i). The results showed distinct distributions of dendrites and axons among E and I neuronal populations, while also highlighting shared areas of high density, including the tectal neuropil, nMLF, ventral anterior hindbrain, lateral middle hindbrain, and caudal hindbrain. These input-output hotspots are linked to the sensorimotor integration and transformation areas in zebrafish[45–49], and are consistent with the hub regions revealed by the graph theoretical analysis of the interregional connectivity networks (see below in Fig. 8).

After the initial global observation, we investigated the projection features of E and I neurons at the single cell level by analyzing their projection strength (PS) to specific brain regions. Here, we defined the projection strength of each neuron to a target region as the total length of coherent axonal arbors with terminals in that region (see Methods). To verify that this parameter is comparable to the number of presynaptic sites for evaluating projection strength, we calculated the matrices for both the presynaptic site and the terminal-bearing axonal length of reconstructed neurons with presynaptic site labeling (Extended Data Fig. 4j,k). We found a high degree of similarity between the two matrices (Pearson $r = 0.784$, $P < 0.001$), suggesting that the length of terminal-bearing axonal fibers is an alternative parameter for assessing projection strength.

We observed that the prominent architectures of axonal innervation include ipsilateral/contralateral (Ipsi/Contra) and ascending/descending (Asc/Desc) projections (Fig. 4j). Qualitatively, we categorized the neurons into three groups related to Ipsi/Contra (Fig. 4k, left) or Asc/Desc projections (Fig. 4k, right) (see Methods). Approximately 53% and 61% of the three E and I neuronal populations display bilateral (i.e., Ipsi-Contra) or bidirectional (i.e., Asc-Desc) projections, respectively. A notable trend was observed where the percentage of contralateral-only projecting neurons increases, while the percentage of descending-only projecting neurons decreases, in the order of *vglut2a/2b* to *gad1b* to *glyt2* neurons. Quantitatively, we calculated the axonal projection strength of each neuron in the four quadrants: ascending-ipsilateral, ascending-contralateral, descending-ipsilateral, and descending-contralateral. The *vglut2a/2b*, *gad1b*, and *glyt2* neurons displayed significantly stronger projections in the ipsilateral-descending, ipsilateral-ascending, and contralateral-ascending directions, respectively (Fig. 4l), suggesting their different roles in interhemispheric communication.

Next, we examined how many times the contralateral-projecting neurons cross between hemispheres and which major brain commissures they pass through (Fig. 4m). Our analysis showed that most (75% on average) of Contra and Ipsi-Contra projecting neurons from all three E and I populations cross hemispheres only once (Fig. 4n), with the majority of

crossings (69%) occurring within 20 μm of the soma along the anteroposterior axis. Multiple crossings existed, with up to dozens in some cases, contributing to a significant discrepancy in the total number of crossings between the E and I neuronal populations (Fig. 4n). These multiple crossings arose either from the main axon path traversing the midline repeatedly via different commissures and/or from collateral branches extending contralaterally. We analyzed the distribution of crossings through ten different commissural regions for all three E and I neuronal populations at the single cell level and found that the ventral rhombencephalic commissure ("ven") is the most frequently used by all three neuronal populations (Fig. 4o). In terms of differences among the three neuronal populations, the number of crossings was higher for E neurons compared with I neurons for most commissural regions, especially the anterior ("ant"), horizontal & postoptic ("hor&pop"), and posterior tuberculum ("tub") commissures, while the *gad1b* neurons showed a greater number of crossings in the posterior commissure ("post") (Fig. 4o).

Taken together, our single-cell analyses of geometric morphology and axonal projections reveal that, compared with I neurons, E neurons are more structurally complex, larger in size, innervate broader regions, and exhibit more cross-hemispheric projections. The abundance of Ipsi-Contra and Asc-Desc projections in both E and I neurons suggests enriched interhemispheric and feedforward-feedback information processing. Furthermore, the Ipsi/Contra and Asc/Desc projection diagram, combined with the interhemispheric crossing distributions, provides a comprehensive overview of the distinct projection patterns of the three E and I neuronal populations throughout the entire brain.

Morphological classification of E and I neurons

To analyze the morphotypes of E and I neurons, we developed a methodology termed MBLAST (named by referring to NBLAST[50]) to assign cell types to large-scale neuron reconstruction datasets based on morphological similarity (see Methods). Neurons were first mirrored to the left hemisphere. We then implemented the classification algorithm to identify a basal set of neuronal morphotypes for the target neuronal population. Next, the identified types were validated by visually inspecting individual cells within the set, serving as an additional review of neuron reconstruction accuracy. MBLAST classified new reconstructions by assigning them to existing cell types, thereby expanding known clusters, or by using them to define novel types.

We classified 14,301 cells (n_E = 9,774, n_I = 4,527) and organized them hierarchically into five nested levels: divisions (D), categories (K), classes, types, and subtypes. At the two highest levels (divisions and categories), both excitatory (*vglut2a/2b*) and inhibitory (*gad1b*, *glyt2*) neurons were assigned to the same organizational framework, including 5 divisions (D1 to D5) and 12 categories (KA to KM) (Fig. 5a,b). The highest-level division was defined based on sensorimotor information flow and contains sensory, sensory relay, premotor, motor,

and other relays. The first four divisions each contain two categories (Fig. 5a,b). The sensory and sensory relay divisions are categorized according to the modality of sensation, distinguishing between special (including olfaction, vision, audition, and vestibular) and somatic/visceral components. The premotor and motor divisions are categorized based on the location of cells—the premotor division is divided into midbrain and hindbrain categories, while the motor division is divided into head and trunk categories. The fifth division, 'other relays', contains all remaining morphotypes that lie between the sensory and motor parts (Fig. 5a,b). It is divided into six categories based mainly on the range and direction of axonal projections: local (projections within one specific brain region), short (short-range projections across adjacent brain regions within one of the five primary region subdivisions, i.e., Tel, Di, M, H, and SC), long|asc (long-range projections ascending across different primary region subdivisions), long|desc (long-range projections descending across different primary region subdivisions), long|asc-desc (long-range projections both ascending and descending across different primary region subdivisions), and cerebellum-related (morphotypes in the cerebellum and those of cerebellar efferents and afferents).

From the class level downward, neurons were further classified within each neurotransmitter population (glutamatergic, GABAergic, or glycinergic), thereby generating parallel hierarchies for distinct E and I neuronal populations (Fig. 5c and Extended Data Fig. 5). At the level of class, the classification of neurons was largely determined by their functional roles in information processing. For instance, within the special categories in sensory and sensory relay divisions, the classes included specialized morphotypes involved in sensing or relaying information for smell, vision, hearing, and equilibrium. Reticulospinal neurons (RSNs) were assigned as a class in the hindbrain category in the premotor division. Different motor branches of cranial nerves belong to different classes in the head category of the motor division. Classes in the 'other relay' division were mainly defined based on their major distribution and projection regions. Based on MBLAST, we created a type classification reflecting differences in the structural morphology of dendrites and axons. Some types were further divided into subtypes with distinct ipsi-/contralateral projection patterns (see below). In total, we classified 71 classes, 305 types, and 348 subtypes for E neurons (*vglut2a/2b*), 36 classes, 155 types, and 164 subtypes for GABAergic I neurons (*gad1b*), and 19 classes, 84 types, and 88 subtypes for glycinergic I neurons (*glyt2*). The full hierarchical morphotypes at the level of subtypes were displayed in Extended Data Fig. 6, and each subtype was assigned with an ID (up to 11 characters) encoding its neurotransmitter identity (Glu, GABA, or Gly), division (one-digit number), category (A–N), class (two-digit numbers), type (two-digit numbers), and subtype (a lowercase letter).

To further evaluate the sampling coverage of our datasets, we assessed cell type distributions within the sampled population. We repeatedly (1,000 rounds) selected subsets of

cells (incrementing by 10 cells per step) from the classified cell pool and compared the cell type composition between the sampled subset and the overall population. The cell type composition began to show no significant dissimilarity when sampling reached ~17% (on average) of the corresponding E and I classified neuronal populations (Extended Data Fig. 7, start point of the black-only region of the gray/black dot trace), although the overall cell type coverage remained below 50%. To determine the minimal sampling size after which cell type coverage stabilizes, we applied a structural breakpoint detection method[51,52] to the cell type coverage curve and found that coverage stabilized at ~22% (on average) of the corresponding neuronal population (Extended Data Fig. 7, vertical dotted color lines), resulting in an average cell-type coverage rate of nearly 65%.

Next, we characterized the distribution of neurons of each type across regions (Fig. 5c and Extended Data Fig. 5, right) and examined the diversity of types within individual regions (Fig. 5d). This bidirectional relationship between morphotypes and brain regions provides information on the regionalization of cell types and the complexity of connections among different regions (see below). The constructed graphs revealed two prominent features: (1) with the exception of some types in the sensory and motor divisions, most types are not constrained to a single region; however, they are typically distributed within one primary region subdivision (Tel, Di, M, H, or SC) and rarely extend beyond it, as indicated by their shared color tone representing the specific subdivision (Fig. 5c and Extended Data Fig. 5, right); (2) the hindbrain shows a higher degree in both the number of regions occupied by a single type (2.3 ± 1.4) and the number of E and I morphotypes (29.2 ± 6.9). Although these analyses may be sensitive to the granularity of cell clustering, these results indicate that neurons in different primary region subdivisions have distinct projection patterns. In particular, the findings suggest that the hindbrain contains more computing elements for sending premotor output to the SC and efference copy/corollary discharge to upper brain regions[53].

Overall, in light of the complete geometric morphology of individual neurons, we have constructed a hierarchical taxonomy of E and I neurons distributed throughout the CNS and PNS. This provides a comprehensive reference for identifying different types of neurons.

Cabling design of E and I morphotypes

To examine the innervation characteristics of the E and I morphotypes, we constructed type-to-region innervation graphs (Extended Data Fig. 8a–c). The CPS contains 68 nervous system anatomical regions at the lowest level of the ontology tree (see Fig. 1c–e, and Supplementary Table 2). We drew the graphs separately for dendrites and axons, distinguishing ipsilateral and contralateral projections across the 68 regions. Innervation strength was normalized by the number of cells of each type to enable quantitative

comparisons among distinct morphotypes within designated regions (Extended Data Fig. 8a–c; see Methods).

At the level of classes, closely related morphotypes exhibited varying dendritic and axonal morphology (Fig. 6a–e). For instance, the class of mitral cells in the olfactory bulb displayed similar dendritic arborization patterns, but could be classified into two distinct types based on their axonal projection patterns (Fig. 6a,b; Glu-2C0102 *vs* Glu-2C0103). Similarly, two types in the nMLF possessed comparable axonal morphology characterized by multiple collaterals innervating the contralateral SC, yet their dendritic configurations were markedly different (Fig. 6a,d; Glu-3E0104 *vs* Glu-3E0107). Further examination through 3D Sholl analysis revealed that although these types share similar dendritic or axonal morphology, structural differences do exist (Fig. 6c,e). This indicates that within specific cell types, there is an inherent correlation between dendritic and axonal structures, both of which represent the morphological distinctions of neuronal types.

Another feature observed in classes is modularity, manifested as cohesive modules of types sharing common projection trajectories. This was often represented by two types sharing the ascending path, while one of them also gives rise to a descending path (Fig. 6f). For instance, two types (Glu-2C0304 and Glu-2C0305) in the class of vestibular relay neurons[54] (see Fig. 5b, KC, marron, *vglut2a/2b*) in rhombomere 5/6 projected to cranial motor neurons in nIII/nIV through a common ascending path, while one type (Glu-2C0305) also extended a descending path to rhombomere 7/8 (R7/8) in the caudal hindbrain (Fig. 6f, left). The relative proportion of these ascending-only and asc-descending counterparts varied among the three E and I neuronal populations (Fig. 6g), aligning with the higher projection strength in the descending direction for E neurons compared with I neurons (see Fig. 4l). The cell bodies of these two counterparts were typically located close to each other, implying that they may share a similar developmental trajectory but undergo distinct structural differentiation. They may work as a module to implement specific functions.

At the level of types, we found that for some of them, which target homologous regions in both hemispheres, bilateral innervation is not solely mediated by a single ipsilateral-contralateral mode but instead via a combination of distinct projection modes, including ipsilateral (Ipsi), ipsilateral-collateral (Ipsi-C), ipsilateral-contralateral (Ipsi-Contra), contralateral (Contra), and contralateral-collateral (Contra-C) (Fig. 6h,i). These modes involved main axonal paths with or without midline-crossing collaterals and were present in both descending and ascending projections of E and I neurons. The neurons involved in different modes were assigned as subtypes. Quantitative analysis revealed significant differences between E and I neurons in their usage of these modes. The *vglut2a/2b* excitatory neurons employed all five modes, while *gad1b* and *glyt2* inhibitory neurons rarely used collaterals and predominantly relied on ipsilateral-contralateral and contralateral projections (Fig. 6j). These findings indicate the distinct strategies employed by E and I neurons to

achieve bilateral connectivity.

Taken together, these findings reveal three key cabling rules: (1) neuronal types with similar dendritic morphologies but divergent axonal projections—or vice versa—constitute distinct morphological variants within a class, highlighting the need to integrate both dendritic and axonal features for accurate classification (Fig. 6k, left); (2) neuronal types sharing a primary trajectory but differing in additional branches form a modular group (class) that likely support related functions through combinatorial wiring (Fig. 6k, middle); (3) neurons differing only in projection lateralization (ipsilateral, contralateral, or bilateral) while following the same trajectory represent subtypes of a single neuronal type, collectively ensuring bilateral coverage (Fig. 6k, right). Moreover, E and I neurons use distinct combinations of ipsilateral/contralateral projection modes.

Inter-cell-type connectome and neural circuit mining

To investigate the nervous system-wide connectivity of E and I neurons, we constructed a global neural network based on the morphotypes at the type level of morphological classification. We grouped GABAergic and glycinergic neurons with similar morphologies into a single type (see Extended Data Fig. 6b), resulting in 197 I types. Together with 305 E types, this yielded a total of 502 types. The network was built through a systematic analysis of the spatial proximity (< 2 μm) between axonal and dendritic arborizations[55] of each E and I morphotype across the entire CNS. To quantify connectivity, we defined the inter-cell-type (mesoscale) connection strength as the sum of eligible dendrite-axon compartment pairs between each connected neuron pair within each type pair, normalized by the total number of connected neuron pairs (see Methods). This enabled the generation of a directed and weighted inter-cell-type mesoscopic connectome with neuronal morphology and E or I identity (Extended Data Fig. 9).

To ensure the reliability of the connectivity analysis, we employed two filtering criteria. First, we evaluated the participation rate of each morphotype, defined as the proportion of its neurons forming connections with a partner morphotype. For a morphotype pair to be considered, we required that at least one of the two morphotypes exhibits a participation rate of no less than 20%. Then we quantified the divergence (one neuron connecting to multiple downstream neurons) and convergence (multiple neurons connecting to one downstream neuron) indices, calculated as the ratio of connected neuron pairs within a morphotype pair to the number of participating neurons in the input (D index) and output morphotypes (C index), respectively. We then applied a threshold, requiring that the D&C indices for a given pair were both larger than 1. Applying these criteria revealed characteristic distributions of three relevant parameters: (1) in 33,660 of morphotype pairs, over 60% of morphotypes showed >50% neuronal participation, indicating robust inter-cell-type connectivity (Fig. 7a);

(2) the distribution of the divergence or convergence index values for each morphotype in connected pairs followed a single-phase decay (R^2 = 0.99), reflecting a structured organization of D&C within the constructed connectome (Fig. 7b); and (3) connection strengths followed a Gaussian distribution (R^2 = 0.98) with a mean value of 16.7 ± 7.1, reflecting the normal range of variability in morphotype connectivity across the network (Fig. 7c).

We then constructed a morphotype-based connectome (Fig. 7d). Illustrating with the visual system, we identified two distinct pathways that exhibited relatively strong and weak connectivity with RGCs, respectively (Fig. 7d–h, and Supplementary Videos 6 and 7). The pathway 1, characterized by strong connections with RGCs, represents a classical visuomotor circuit (Fig. 7e,g and Supplementary Video 6). After receiving RGC innervation, it begins with tectal projection neurons (i.e., periventricular neurons, PVNs) in the optic tectum (TeO), a central hub for visual information processing. Among the connected PVN morphotypes, the most numerous are tectobulbar neurons with ipsilaterally and laterally positioned projections (iTB-L), which are involved in approach movements of zebrafish[56]. From the TeO, the pathway continues to hindbrain reticulospinal neurons (RSNs), which act as premotor neurons before reaching the motor neurons (MNs) in the SC. Analysis revealed that most of the 28 RSN morphotypes form connections with iTB-L neurons. We highlighted here a RSN morphotype located in rhombomere 1 (R1) with bilateral projections. It exhibited strong connectivity to MNs, marked by the highest convergence index (22.3) in comparison with other RSNs (Fig. 7e,h).

The pathway 2 (Fig. 7f,g and Supplementary Video 7), characterized by relatively weak connections with RGCs, aligns with and corroborates previous research on light-preference behavior in zebrafish[57,58]. After receiving RGC innervation, this pathway begins with eminentia thalami (EmT) neurons, whose dendrites form connections with RGCs at arborization fields 3 and 4 (AF3 and AF4) (Fig. 7f, arrow in top-right image). The single-cell morphology of EmT neurons supports the preferred projection from bilateral EmT to the left dorsal habenula (Ha), consistent with previous functional and dye-tracing studies[57] (Fig. 7f,g). Accordingly, the downstream neurons in the Ha are mainly distributed on the left dorsal side. These neurons connect either directly to the primary inhibitory neurons in the SR, which project ascendingly to the subpallium (S) in the diencephalon, or indirectly to the SR inhibitory neurons via local inhibitory neurons in the interpeduncular nucleus (IPN). The feedforward inhibition motif, involving Ha, IPN, and SR, may underlie the bimodal role of raphe serotonergic neurons in light-preference behavior[58]. Notably, the strongest downstream connection from the SR leads to neurons in the subpallium, a region previously implicated in light/dark choice behavior in adult fish[59]. In addition, we identified a feedback loop from the subpallium to SR, either directly or indirectly via morphotypes in the intermediate hypothalamus (Hi), further highlighting the dynamic regulatory processes within these

circuits (Fig. 7f,g).

Overall, by leveraging the nervous system-wide quantitative network based on neuronal morphotypes, we mapped the detailed cellular composition of a canonical visuomotor pathway and identified a light preference-associated pathway that has not been well characterized previously. This demonstrates the utility of the inter-cell-type mesoscopic connectome in unraveling the intricate complexity underlying brain functions.

E and I neuron-based interregional connectome and information flow framework

While the inter-cell-type connectome provides intricate details about connectivity between neuronal types, it lacks information about brain regions. As brain regions serve as integral units for processing and transmitting information, we further constructed a directed and weighted interregional macroscopic connectome based on the axonal projection of E and I neurons. We defined the macroscale connection strength (CS) from a source to a target region as follows: first, we calculated the total length of coherent axonal arbors with terminals in the target region and normalized this value by the number of sampled neurons in the source region. This normalized value was then scaled by the complete cell count of the source region (see Methods). The retina was not included due to the lack of cell count. This approach produced a comprehensive quantitative macroscopic connectome for the zebrafish nervous system.

We conducted the analysis on 53 anatomical regions, in which the cranial motor nuclei were merged into higher-level brain regions, and the rostral and caudal islands of the same anatomical structures were combined. The wiring diagrams were generated separately for E and I neurons, presenting both ipsilateral/contralateral and ascending/descending connections (Fig. 8a). These diagrams revealed several prominent features. First, the macroscale CS in both E and I networks vary by a factor of 10^6 across the entire nervous system, and follow a one-component lognormal distribution (Fig. 8b). Second, although a weak negative correlation was observed between CS and distance for both E ($P = 0.04$) and I ($P < 0.001$) interregional connections, the effect sizes are minimal ($R^2 = 0.003$ for E, and $R^2 = 0.02$ for I), indicating negligible associations (Fig. 8c). This suggests that long-distance connections are targeted rather than randomly formed. Third, the E dominance, calculated as $(CS_E - CS_I)/(CS_E + CS_I)$, is common for both ipsilateral and contralateral connections in both descending and ascending directions, and applies to both inter-brain region (B-B) connections and mutual brain-SC (B-S) connections (Fig. 8a,d). For B-B connections in particular, the degree of E dominance is greater for descending than for ascending connections. Fourth, both E and I descending connections exhibit a stronger ipsilateral preference, calculated as $(CS_{Ipsi} - CS_{Contra})/(CS_{Ipsi} + CS_{Contra})$, than ascending ones, and B-B connections prefer ipsilateral connections more than B-S connections (Fig. 8a,e).

To further explore the features of this interregional connectome, we applied

graph-theoretical methods[60] to analyze the topological properties of the directed and weighted interregional networks (45 regions, excluding peripheral ganglia due to the lack of input node information). First, we evaluated the node degree, a fundamental network measurement. Given a directed network, we calculated the input degree (D_I), output degree (D_O), and the IO index (calculated as $(D_I - D_O)/(D_I + D_O)$), which reflects node polarity (positive for receivers and convergence, negative for senders and divergence) (Fig. 8f). We found a roughly balanced distribution between receivers and senders. Specifically, 22 nodes had an IO index > 0 (i.e., positioned to the left of the 45-degree diagonal), 4 nodes had an IO index = 0, and 19 nodes had an IO index < 0 (i.e., positioned to the right of the 45-degree diagonal) (Fig. 8f). In addition, nodes with higher total IO degrees exhibited a more balanced input-output ratio (IO index around zero) (Fig. 8f, inset), indicating a shift from polarized to non-polarized nodes as the number of connections increases.

We next examined two-region motifs (E and I interconnections between nodes) by applying the concept of circuit motifs involving E and I neurons[61]. We identified six distinct motifs involving at least two directed connections (Fig. 8g). Quantitative analysis (Fig. 8h) revealed several prominent features: (1) the pure recurrent excitation motif (RE, #1) is present but relatively rare (~12%); (2) the pure mutual inhibition motif (MI, #2) is absent, and even the motif combining MI with a single excitatory connection (MI+E, #5) is uncommon (~2%); (3) motifs involving feedback inhibition (FI, #3–6) are predominant (collectively ~88%), indicating that excitatory connections are frequently accompanied by feedback inhibition; and (4) the most prevalent motif (#6), accounting for ~44% of cases, consists of bidirectional connections for both E and I.

We then examined three-region motifs (three-node connected subgraphs)[62] to further investigate the structural design. Specifically, we employed an algorithm to calculate the number of all 13 distinct motifs for both E and I networks (Fig. 8i). We found that the proportions of motifs in the E and I networks are highly correlated (Fig. 8i, top; $R^2 = 0.6$, $P < 0.01$), reinforcing the coordinated organization between E and I connections. Moreover, motifs featuring reciprocal connections (#3, 6–8, and 10–13) account for a substantial proportion (E, 85%; I, 80%). To assess the significance of these motifs, we compared their occurrences in the real networks against shuffled networks that preserve the same IO degree distribution (Fig. 8i, bottom). The real networks exhibited significantly different motif occurrence patterns compared with the shuffled ones (Fig. 8i; Real *vs* shuffled E: $X^2 = 15{,}564$, $P < 0.001$; Real *vs* shuffled I: $X^2 = 11{,}479$, $P < 0.001$). Notably, the shuffled networks exhibited a markedly lower proportion of motifs containing reciprocal connections (shuffled E, 40%; shuffled I, 33%) compared with the real networks.

We further investigated the information flow (IF) pathways across the entire nervous system network. We quantified the hub distribution by calculating nine centrality metrics for each node, including input strength, output strength, input degree, output degree, weighted

betweenness centrality, weighted closeness, PageRank, clustering, and vitality (Extended Data Fig. 10a; see Methods). We defined a region as a hub if it scored over the mean for all metrics, and identified hubs for the E, I, and two separate I (GABAergic and glycinergic) networks. Using t-SNE visualization[63], we projected the nine metrics into two dimensions and color-coded nodes based on their hub scores (the sum of scores from all metrics) (Extended Data Fig. 10b). This analysis revealed top hubs in the zebrafish nervous system, including the TeO, R1, R6, R7, and R8 (Extended Data Fig. 10b), which are highly connected with both distant and proximal regions (Extended Data Fig. 10c). We then constructed a hub network, in which nodes represent anatomical regions weighted by hub scores, and edges denote directed IF between regions weighted by betweenness centrality (Fig. 8j, Extended Data Fig. 11, and Supplementary Video 8). Betweenness centrality measures the proportion of shortest paths between all node pairs that pass through an edge, indicating its importance in IF pathways. The hub networks provide a comprehensive view of the most efficient and likely pathways for information transfer from any source to any target region.

To illustrate their application, we analyzed the E hub network to investigate sensorimotor IF pathways from sensory regions to the SC, the motor output terminal (Fig. 8k). We observed a convergence of multimodal sensory information, including vision, olfaction, mechanoreception (audition and water flow), and somatic and visceral senses, onto the premotor hubs R1, R7, or R8 in the hindbrain, from which signals are relayed to the SC. The processing depth ranges from 2 to 4 steps. Somatic and visceral sensory pathways are processed most rapidly (2 steps), followed by mechanoreception (3 steps), and then vision and olfaction (4 steps) (Fig. 8k).

Overall, the directed and weighted interregional networks exhibit stronger E connections than I ones, with descending connections favoring ipsilateral connections over ascending ones. At the structural level, both E and I connections form specific subgraph motifs, prominently featuring feedback inhibition and reciprocal connectivity. Furthermore, E and I networks share key hubs, including the TeO, R1, and R8. Functionally, multimodal sensorimotor processing occurs in different steps, with R1, R7, and R8 acting as convergent premotor hubs that facilitate motor outputs.

Discussion

The larval zebrafish serves as a unique model organism in neuroscience research, enabling all-optical structural and functional imaging of the entire brain at cellular resolution in awake animals[64]. To decode how this vertebrate brain works, it is important to develop a comprehensive digital zebrafish holographic atlas integrating multimodal information, including gene expression, neuronal morphology, connectivity, and activity. Here, we generate key datasets in a common coordinate framework, comprising: (1) a whole body-wide CPS of 6-dpf larval zebrafish with two original transgenic reference templates and 3D

neuroanatomical parcellations (173 regions); (2) a gene-expression-pattern image atlas by incorporating relevant reference templates (702 lines) into the CPS; (3) a nervous system-wide cytoarchitecture atlas of E and I neurons; (4) a single-cell morphology atlas of E and I neurons (20,011 cells), characterized by the nervous system-wide coverage of cell distribution, whole body-wide coverage of neuronal projection, neurotransmitter identity annotation, dendrite-axon annotation, and hierarchical morphological classification (600 subtypes); and (5) mesoscale (inter-cell-type) and macroscale (interregional) connectomes. These datasets, publicly available at https://zebrafish.cn/LM-Atlas/EI (Extended Data Fig. 12), offer a platform for integrating, exploring, and interpreting data at a nervous system-wide scale.

Previous brain templates were usually based on tissue autofluorescence[65] or single gene expression pattern[9,41,42]. In this study, we employed the multichannel functionality in ANTs to create dual-channel (dual-color) templates. This approach generated two cellular-resolution reference templates within a common coordinate framework, each characterized by distinct expression patterns and transgenic fluorescence, providing more flexible references and bridges for image registration. Furthermore, our methodology employed shape-based averaged templates directly aligned to the CPS via a single registration step. This approach avoids the conventional method of averaging multiple individually registered scans, offering greater accuracy and efficiency in expanding the reference template set. We also improved the registration process by separating the RA registration and warp registration. This refinement allows for precise RA results before the computationally intensive warp step. In addition, we optimized the registration parameters, enhancing registration accuracy for both live-to-live and live-to-fixed samples. Using a gold-standard landmark evaluation system, we achieve cellular-resolution precision of the inter-atlas (~8 μm, see Extended Data Fig. 1k) and single-cell-morphology-atlas registrations (~3 μm, see Extended Data Fig. 2f). Besides well-resolved nervous system structures, the autofluorescence of the fish body enables a complete spatial layout of the organism. Future developments, such as increased imaging depth and incorporation of visceral structures, will transform the current CPS into a more comprehensive whole-body framework. This will support the building of a projectome and connectome atlas encompassing the central, peripheral (somatic and autonomic), and even the enteric nervous systems[66].

Our cell morphology mapping follows a genetically targeted strategy, focusing on the largest and most fundamental neuronal populations: excitatory and inhibitory neurons. We selected four key gene markers—*vglut2a*, *vglut2b*, *gad1b*, and *glyt2*—which collectively represent the majority of zebrafish E and I neurons[30,67–69]. Future studies could further refine E and I neuron subtypes using intersectional genetic tools[28] informed by single-cell RNA-Seq[70]. As an immediately accessible next step, the single-cell morphology atlas could be expanded

to include neuromodulatory, neuropeptidergic, and hormone-secreting neurons. Our study establishes a standardized pipeline for constructing atlases of genetically defined neuronal types—from reference template generation to cell counting to morphology reconstruction—facilitating systematic characterization of neuronal distribution and morphology.

Co-transmission has emerged as a fundamental neural signaling mechanism[71], with evidence suggesting widespread co-release of GABA or glutamate within zebrafish catecholaminergic systems[69]. Consistently, we identified homologous cell types between published single-cell morphologies of neuromodulatory/neuropeptidergic neurons and our MBLAST-derived E and I neuron morphotypes. Examples include posterior tuberculum/hypothalamus dopaminergic neurons[72], hypothalamus neuropeptide QRFP neurons[73], and preoptic oxytocinergic neurons[74,75] within our *vglut2a/2b* excitatory morphotypes, as well as locus coeruleus norepinephrinergic neurons[72] and superior raphe serotonergic neurons[76,77] within our *gad1b* inhibitory morphotypes. Overall, our single E and I neuron atlas provides a valuable repository for mining potential co-transmission neuron types.

To analyze neuron projection features, build wiring diagrams, and infer information flow across the nervous system, we classified the DA processes of reconstructed E and I neurons' morphology by combining bio-labeling and machine-learning. Utilizing data from the presynaptic site and morphology co-labeling, we summarized three major neurite origin and branching strategies in zebrafish neurons. Notably, the pseudounipolar-like strategy, in which primary axons frequently originate from dendritic branches rather than directly from the soma, is prominent, as exemplified by tectal projection neurons. The trained classifier performed robustly for neuron types with clear polarity, particularly long-range projection neurons, and achieved moderate accuracy for short-range inhibitory neurons and local neurons. Further refinement of the classification algorithm in a cell-type-specific manner will enhance accuracy.

Neuronal morphology, including dendritic and axonal configurations, is a fundamental criterion for cell type classification, as it underlies connectivity specificity and functional diversity in neural circuits. Morphology-based cell-type classification provides key insights into neuronal projection design rules. One important rule is that bilaterally innervating neuronal types can achieve overall symmetry through a combination of distinct ipsilateral and contralateral projection modes, with E and I neurons exhibiting different mode preferences (see Fig. 6h–j). This organization likely reflects the interplay between genetic and environmental influences in neuronal morphogenesis and may contribute to brain lateralization[78,79]. The relative proportions of ipsilateral and contralateral projections may vary across species and individuals, shaping structural correlates of brain asymmetry and individuality. In addition, E and I neuronal populations participate in distinct circuit motifs and large-scale architectures[61]. Variations in ipsilateral-contralateral composition thus add

another layer of hemispheric functional specialization. Investigating these projection patterns within functional circuits will be of great interest. Another rule is that several morphotypes within one class can share one primary projection trajectory while diverging to form distinct trajectories (see Fig. 6a–g), suggesting a modular architecture. Such neuronal types, with partially overlapping and partially distinct projections, may function cooperatively and independently within circuits, acting as a functional module to coordinate target innervation. Structurally, this modularity is reflected in the combination of shared and unique axonal features across morphotypes, supporting the idea that new morphotypes may arise through incremental modifications of existing patterns. This provides a potential developmental mechanism for how neuronal diversity emerges from conserved projection patterns. Further supporting this speculation, we observed neuronal types with similar dendritic arborizations but different axonal projections, and vice versa (see Fig. 6a–e). In addition, neuronal morphology correlates strongly with spatial distribution, with distinct types localized to specific brain subdivisions (see Fig. 5). This regional specialization aligns with the idea that neuronal types are structurally and functionally tailored to specific brain areas, underscoring the role of regional organization of the brain.

Our polarity-annotated neuron datasets enable the construction of directed and quantitatively weighted connectome at both inter-cell-type (mesoscale) and interregional (macroscale) levels (see Figs. 7 and 8). The inter-cell-type connectome, derived from neuronal morphologies, provides insights into circuit mechanisms. As exemplified in Fig. 7, we identified a classical visuomotor circuit as well as a poorly characterized circuit underlying phototactic behaviors. These highlight the value of our directed and weighted mesoscopic connectome in mining novel circuits and bridging structural connectivity with potential functions. In terms of the interregional connectome, two features of E and I connectivity are prominent: (1) E connections dominate interregional communication, and (2) E and I connections are co-organized, forming similar subgraph motifs and featuring feedback inhibition across networks. Together, these findings provide a fundamental framework for understanding E and I network architectures, which may be conserved across vertebrates.

Beyond documenting connectivity features, we transformed the interregional connectivity network into a hub network by assessing both regional and connection centrality. Separate hub networks were constructed for E and I neurons, highlighting their roles in information flow in the process of sensorimotor transformation (see Fig. 8j,k and Extended Data Fig. 11). Key findings include: (1) a strong correlation between hub regions and dendrite/axon distribution hotspots (see Extended Data Fig. 10b and Fig. 4h,i); (2) shared top-ranking hubs in both E and I networks, notably the TeO, R1, and R8; (3) high hub scores across all hindbrain rhombomeres (see Extended Data Fig. 10b), supporting the notion of the hindbrain as a continuous premotor-coordinating structure; (4) convergent sensorimotor transformation areas, specifically R1, R7, and R8 (see Fig. 8k), aligning with those found in

brain-wide neural activity maps related to perception and behavior[41,47,48]. In addition, we mapped the shortest sensory processing pathways leading to motor outputs in the SC. Notably, visual and olfactory modalities involve more intermediate steps before motor execution compared with somatic/visceral and mechanoreceptive modalities, a finding that aligns with the hierarchy of sensory experience[80].

Our study identified hundreds of E and I morphotypes in zebrafish. Integrating transcriptomic datasets with morphologically characterized individual neurons will refine this classification by incorporating genetic determinants[81]. Application of targeted trans-monosynaptic viral tracing[82–85] will amass data on precise neuronal connectivity within specific circuits. Through our nervous system-wide CPS, comprehensive multimodal mesoscopic atlases can be achieved by integrating molecular, structural (projectome and connectome), chemical (neurotransmitter activity), and behavior-related neuronal activity maps. In the coming future, aligning multimodal mesoscopic atlases with zebrafish electron microscopy connectome data will enable the creation of a molecule-structure-function integrated connectome with precise cell-type identity and neuronal connectivity, providing an important framework for neuroscience research.

References

1. J G White 1, E Southgate, J N Thomson, S. B. The structure of the nervous system of the nematode Caenorhabditis elegans. *Philos. Trans. R. Soc. London. B, Biol. Sci.* **314**, 1–340 (1986).
2. Cook, S. J. *et al.* Whole-animal connectomes of both Caenorhabditis elegans sexes. *Nature* **571**, 63–71 (2019).
3. Witvliet, D. *et al.* Connectomes across development reveal principles of brain maturation. *Nature* **596**, 257–261 (2021).
4. Chiang, A. S. *et al.* Three-dimensional reconstruction of brain-wide wiring networks in drosophila at single-cell resolution. *Curr. Biol.* **21**, 1–11 (2011).
5. Zheng, Z. *et al.* Resource A Complete Electron Microscopy Volume of the Brain of Adult Drosophila melanogaster A Complete Electron Microscopy Volume of the Brain of Adult Drosophila melanogaster. *Cell* **174**, 730-743.e22 (2018).
6. Scheffer, L. K. *et al.* A connectome and analysis of the adult drosophila central brain. *Elife* **9**, 1–74 (2020).
7. Winding, M. *et al.* The connectome of an insect brain. *Science* **379**, eadd9330 (2023).
8. Dorkenwald, S. *et al.* Neuronal wiring diagram of an adult brain. *Nature* **634**, 124–138 (2024).
9. Kunst, M. *et al.* A Cellular-Resolution Atlas of the Larval Zebrafish Brain. *Neuron* **103**, 21-38.e5 (2019).
10. Gautam, R. *et al.* Predicting modular functions and neural coding of behavior from a synaptic wiring diagram. *Nat. Neurosci.* **8**, (2024).
11. Svara, F. *et al.* Automated synapse-level reconstruction of neural circuits in the larval zebrafish brain. *Nat. Methods* **19**, 1357–1366 (2022).

12. Winnubst, J. *et al.* Reconstruction of 1,000 Projection Neurons Reveals New Cell Types and Organization of Long-Range Connectivity in the Mouse Brain. *Cell* **179**, 268-281.e13 (2019).
13. Peng, H. *et al.* Morphological diversity of single neurons in molecularly defined cell types. *Nature* **598**, 174–181 (2021).
14. Gao, L. *et al.* Single-neuron projectome of mouse prefrontal cortex. *Nat. Neurosci.* **25**, 515–529 (2022).
15. Qiu, S. *et al.* Whole-brain spatial organization of hippocampal single-neuron projectomes. *Science* **383**, (2024).
16. Schneider-Mizell, C. M. *et al.* Inhibitory specificity from a connectomic census of mouse visual cortex. *Nature* **640**, 448–458 (2025).
17. Gou, L. *et al.* Single-neuron projectomes of macaque prefrontal cortex reveal refined axon targeting and arborization. *Cell* **188**, 3806-3822.e24 (2025).
18. Shapson-Coe, A. *et al.* A petavoxel fragment of human cerebral cortex reconstructed at nanoscale resolution. *Science* **384**, eadk4858 (2024).
19. Santiago, R. y C. Estructura de los centros nerviosos de las aves. *Rev. Trim. Histol. Norm. Patol.* **1**, 1–10 (1888).
20. Swanson, L. W. & Lichtman, J. W. From Cajal to Connectome and beyond. *Annu. Rev. Neurosci.* **39**, 197–216 (2016).
21. Suárez, L. E., Markello, R. D., Betzel, R. F. & Misic, B. Linking Structure and Function in Macroscale Brain Networks. *Trends Cogn. Sci.* **24**, 302–315 (2020).
22. Zeng, H. Mesoscale connectomics. *Curr. Opin. Neurobiol.* **50**, 154–162 (2018).
23. Yao, S. *et al.* A whole-brain monosynaptic input connectome to neuron classes in mouse visual cortex. *Nat. Neurosci.* **26**, 350–364 (2023).
24. Kasthuri, N. *et al.* Saturated Reconstruction of a Volume of Neocortex. *Cell* **162**, 648–661 (2015).
25. Motta, A. *et al.* Dense connectomic reconstruction in layer 4 of the somatosensory cortex. *Science* **366**, (2019).
26. Ngai, J. BRAIN 2.0: Transforming neuroscience. *Cell* **185**, 4–8 (2022).
27. Mueller, D. T. & Wullimann, M. *Atlas of Early Zebrafish Brain Development*. (Elsevier, 2016).
28. Tabor, K. M. *et al.* Brain-wide cellular resolution imaging of cre transgenic zebrafish lines for functional circuit-mapping. *Elife* **8**, 1–21 (2019).
29. Hiraki-Kajiyama, T. *et al.* An atlas and database of neuropeptide gene expression in the adult zebrafish forebrain. *J. Comp. Neurol.* **532**, 1–46 (2024).
30. Cui, W. W. *et al.* The zebrafish shocked gene encodes a glycine transporter and is essential for the function of early neural circuits in the CNS. *J. Neurosci.* **25**, 6610–6620 (2005).
31. Bai, L. *et al.* Volumetric Imaging of Neural Activity by Light Field Microscopy. *Neurosci. Bull.* **38**, 1559–1568 (2022).
32. Wang, X. *et al.* Three-dimensional intact-tissue sequencing of single-cell transcriptional states. *Science* **361**, (2018).
33. Alon, S. *et al.* Expansion sequencing: Spatially precise in situ transcriptomics in intact biological systems. *Science* **371**, (2021).

34. Petkova, M. D. *et al.* A connectomic resource for neural cataloguing and circuit dissection of the larval zebrafish brain. *bioRxiv* 2025.06.10.658982 (2025).
35. Li, F. *et al.* Multiplexed Neuromodulatory-Type-Annotated EM-Reconstruction of Larval Zebrafish. *bioRxiv* 2025.06.12.659365 (2025).
36. Vishwanathan, A. *et al.* Electron Microscopic Reconstruction of Functionally Identified Cells in a Neural Integrator. *Curr. Biol.* **27**, 2137-2147.e3 (2017).
37. Wanner, A. A. & Vishwanathan, A. Methods for Mapping Neuronal Activity to Synaptic Connectivity: Lessons From Larval Zebrafish. *Front. Neural Circuits* **12**, 1–12 (2018).
38. Vergara, H. M. *et al.* Whole-body integration of gene expression and single-cell morphology. *Cell* **184**, 4819-4837.e22 (2021).
39. Hildebrand, D. G. C. *et al.* Whole-brain serial-section electron microscopy in larval zebrafish. *Nature* **545**, 345–349 (2017).
40. Avants, B. B. *et al.* A reproducible evaluation of ANTs similarity metric performance in brain image registration. *Neuroimage* **54**, 2033–2044 (2011).
41. Randlett, O. *et al.* Whole-brain activity mapping onto a zebrafish brain atlas. *Nat. Methods* **12**, 1039–1046 (2015).
42. Marquart, G. D. *et al.* A 3D Searchable Database of Transgenic Zebrafish Gal4 and Cre Lines for Functional Neuroanatomy Studies. *Front. Neural Circuits* **9**, 78 (2015).
43. Shainer, I. *et al.* A single-cell resolution gene expression atlas of the larval zebrafish brain. *Sci. Adv.* **9**, 1–10 (2023).
44. Marquart, G. D. *et al.* High-precision registration between zebrafish brain atlases using symmetric diffeomorphic normalization. *Gigascience* **6**, 1–15 (2017).
45. Barker, A. J. & Baier, H. Sensorimotor decision making in the Zebrafish tectum. *Curr. Biol.* **25**, 2804–2814 (2015).
46. Bianco, I. H. & Engert, F. Visuomotor transformations underlying hunting behavior in zebrafish. *Curr. Biol.* **25**, 831–846 (2015).
47. Chen, X. *et al.* Brain-wide Organization of Neuronal Activity and Convergent Sensorimotor Transformations in Larval Zebrafish. *Neuron* **100**, 876-890.e5 (2018).
48. Privat, M. *et al.* Sensorimotor Transformations in the Zebrafish Auditory System. *Curr. Biol.* **29**, 4010-4023.e4 (2019).
49. Lee, M. M., Arrenberg, A. B. & Aksay, E. R. F. A structural and genotypic scaffold underlying temporal integration. *J. Neurosci.* **35**, 7903–7920 (2015).
50. Costa, M., Manton, J. D., Ostrovsky, A. D., Prohaska, S. & Jefferis, G. S. X. E. NBLAST: Rapid, Sensitive Comparison of Neuronal Structure and Construction of Neuron Family Databases. *Neuron* **91**, 293–311 (2016).
51. Zeileis, A., Leisch, F., Homik, K. & Kleiber, C. strucchange: An R Package for Testing for Structural Change. *J. Stat. Softw.* **7**, 1–38 (2002).
52. Zeileis, A., Kleiber, C., Walter, K. & Hornik, K. Testing and dating of structural changes in practice. *Comput. Stat. Data Anal.* **44**, 109–123 (2003).
53. Straka, H., Simmers, J. & Chagnaud, B. P. A New Perspective on Predictive Motor Signaling. *Curr. Biol.* **28**, R232–R243 (2018).
54. Schoppik, D. *et al.* Gaze-stabilizing central vestibular neurons project asymmetrically to extraocular motoneuron pools. *J. Neurosci.* **37**, 11353–11365 (2017).

55. Cook, S. J., Kalinski, C. A. & Hobert, O. Neuronal contact predicts connectivity in the C. elegans brain. *Curr. Biol.* **33**, 2022.11.13.516316 (2023).
56. Helmbrecht, T. O., dal Maschio, M., Donovan, J. C., Koutsouli, S. & Baier, H. Topography of a Visuomotor Transformation. *Neuron* **100**, 1429-1445.e4 (2018).
57. Zhang, B. bing, Yao, Y. yuan, Zhang, H. fei, Kawakami, K. & Du, J. lin. Left Habenula Mediates Light-Preference Behavior in Zebrafish via an Asymmetrical Visual Pathway. *Neuron* **93**, 914-928.e4 (2017).
58. Cheng, R. K., Krishnan, S., Lin, Q., Kibat, C. & Jesuthasan, S. Characterization of a thalamic nucleus mediating habenula responses to changes in ambient illumination. *BMC Biol.* **15**, 1–21 (2017).
59. Lau, B. Y. B., Mathur, P., Gould, G. G. & Guo, S. Identification of a brain center whose activity discriminates a choice behavior in zebrafish. *Proc. Natl. Acad. Sci. U. S. A.* **108**, 2581–2586 (2011).
60. Bullmore, E. & Sporns, O. Complex brain networks: Graph theoretical analysis of structural and functional systems. *Nat. Rev. Neurosci.* **10**, 186–198 (2009).
61. Luo, L. Architectures of neuronal circuits. *Science* **373**, (2021).
62. Milo, R. *et al.* Network Motifs: Simple Building Blocks of Complex Networks. *Science* **298**, 824–827 (2002).
63. Maaten, L. van der & Hinton, G. Visualizing Data using t-SNE. *J. Mach. Learn. Res.* **9**, 2579–2605 (2008).
64. Loring, M. D., Thomson, E. E. & Naumann, E. A. Whole-brain interactions underlying zebrafish behavior. *Curr. Opin. Neurobiol.* **65**, 88–99 (2020).
65. Wang, Q. *et al.* The Allen Mouse Brain Common Coordinate Framework: A 3D Reference Atlas ll ll Resource. *Cell* **181**, 936-953.e20 (2020).
66. Spencer, N. J. & Hu, H. Enteric nervous system: sensory transduction, neural circuits and gastrointestinal motility. *Nat. Rev. Gastroenterol. Hepatol.* **17**, 338–351 (2020).
67. Higashijima, S. I., Mandel, G. & Fetcho, J. R. Distribution of prospective glutamatergic, glycinergic, and gabaergic neurons in embryonic and larval zebrafish. *J. Comp. Neurol.* **480**, 1–18 (2004).
68. Kidwell, C. U., Su, C. Y., Hibi, M. & Moens, C. B. Multiple zebrafish atoh1 genes specify a diversity of neuronal types in the zebrafish cerebellum. *Dev. Biol.* **438**, 44–56 (2018).
69. Filippi, A., Mueller, T. & Driever, W. vglut2 and gad expression reveal distinct patterns of dual GABAergic versus glutamatergic cotransmitter phenotypes of dopaminergic and noradrenergic neurons in the zebrafish brain. *J. Comp. Neurol.* **522**, 2019–2037 (2014).
70. Raj, B. *et al.* Simultaneous single-cell profiling of lineages and cell types in the vertebrate brain. *Nat. Biotechnol.* **36**, 442–450 (2018).
71. Svensson, E. *et al.* General principles of neuronal co-transmission: Insights from multiple model systems. *Front. Neural Circuits* **12**, 1–28 (2019).
72. Tay, T. L., Ronneberger, O., Ryu, S., Nitschke, R. & Driever, W. Comprehensive catecholaminergic projectome analysis reveals single-neuron integration of zebrafish ascending and descending dopaminergic systems. *Nat. Commun.* **2**, 112–171 (2011).
73. Chen, A. *et al.* QRFP and its receptors regulate locomotor activity and sleep in

zebrafish. *J. Neurosci.* **36**, 1823–1840 (2016).
74. Herget, U., Gutierrez-Triana, J. A., Thula, O. S., Knerr, B. & Ryu, S. Single-cell reconstruction of oxytocinergic neurons reveals separate hypophysiotropic and encephalotropic subtypes in larval zebrafish. *eNeuro* **4**, 1–16 (2017).
75. Lovett-Barron, M. *et al.* Multiple convergent hypothalamus–brainstem circuits drive defensive behavior. *Nat. Neurosci.* **23**, 959–967 (2020).
76. Yokogawa, T., Hannan, M. C. & Burgess, H. A. The dorsal raphe modulates sensory responsiveness during arousal in zebrafish. *J. Neurosci*. **32**, 15205–15215 (2012).
77. Huang, K. W. *et al.* Molecular and anatomical organization of the dorsal raphe nucleus. *Elife* **8**, 1–34 (2019).
78. Güntürkün, O., Ströckens, F. & Ocklenburg, S. Brain lateralization: A comparative perspective. *Physiol. Rev.* **100**, 1019–1063 (2020).
79. Miletto Petrazzini, M. E., Sovrano, V. A., Vallortigara, G. & Messina, A. Brain and Behavioral Asymmetry: A Lesson From Fish. *Front. Neuroanat.* **14**, 1–22 (2020).
80. Sun, W., Ripp, I., Borrmann, A., Moll, M. & Fairhurst, M. Touch-driven advantages in reaction time but not in performance in a cross-sensory comparison of reinforcement learning. *Heliyon* **11**, e41330 (2025).
81. Gouwens, N. W. *et al.* Integrated Morphoelectric and Transcriptomic Classification of Cortical GABAergic Cells. *Cell* **183**, 935-953.e19 (2020).
82. Dohaku, R. *et al.* Tracing of afferent connections in the zebrafish cerebellum using recombinant rabies virus. *Front. Neural Circuits* **13**, 1–15 (2019).
83. Kler, S., Ma, M., Narayan, S., Ahrens, M. B. & Albert, Y. Cre-Dependent Anterograde Transsynaptic Labeling and Functional Imaging in Zebrafish Using VSV With Reduced Cytotoxicity. *Front. Neuroanat.* **15**, 1–10 (2021).
84. Satou, C. *et al.* A viral toolbox for conditional and transneuronal gene expression in zebrafish. *Elife* **11**, 1–24 (2022).
85. Chen, T.-L. *et al.* An applicable and efficient retrograde monosynaptic circuit mapping tool for larval zebrafish. *eLife* 1–32 (2024). doi:10.7554/eLife.100880.1

Methods

Zebrafish husbandry and preparation

Adult zebrafish were maintained at 28 □ in an automatic fish housing system at the National Zebrafish Resources of China (Shanghai, China). All image data were collected from transgenic larval zebrafish at 6 days post-fertilization (dpf), a stage at which sex has not yet been determined. Experimental larvae were raised in 10% Hank's solution consisted of (in mM): 140 NaCl, 5.4 KCl, 0.25 Na_2HPO_4, 0.44 KH_2PO_4, 1.3 $CaCl_2$, 1.0 $MgSO_4$ and 4.2 $NaHCO_3$ (pH 7.2) under a 14-h:10-h light:dark cycle at 28 □. Larvae lacking the *nacre* genetic background were treated with 0.003% 1-phenyl-2-thiourea (PTU) starting from 8–22 hours post-fertilization to prevent pigmentation. The transgenic lines used were listed below: *Tg(HuC[elavl3]:Hsa.H2B-GCaMP6s)jf5*[86], *TgBAC(gad1b:EGFP)ion84*[87], *Tg(glyt2[slc6a5]:GFP)cf3*[88], *Tg(isl2b.2:GAL4-VP16, myl7:EGFP)zc60*[89],

Tg(-7atoh7:GAL4-VP16)s1992t[90], *Tg(cbln12:GAL4FF)ion220d*[85], *Tg(4×nrUAS:GFP)c369*[91], *Tg(elavl3:NES-jRGECO1a)ion72d*[92], *Et(vmat2:GFP)pku2*[93]. All animal protocols were reviewed and approved by the Animal Care and Use Committee of the Center for Excellence in Brain Science and Intelligence Technology, Chinese Academy of Sciences (NA-046-2023).

Genetic tools

To label E and I neurons, we generated DNA constructs and transgenic lines using either short promotor or BAC clone. For *vglut2a:GAL4FF* and *glyt2:GAL4FF*, we PCR amplified the *GAL4FF* fragment with a Kozak sequence and restriction enzyme digestion sites and inserted it into the *Tol2* vector with ~ 2.2 kb *vglut2a* (a gift from Dr. Wei Hu, Institute of hydrobiology, CAS, Wuhan, China) and ~ 6.8 kb *glyt2*[88] promotor, respectively. The *cpce:GAL4FF* construct for generating transgenic fish was previously reported[85]. For *vglut2b:GAL4FF* and *gad1b:GAL4-VP16*, we used BAC recombineering as described previously[94]. First, the BAC clone was transformed into SW105 bacterial strain to enable the heat-inducible homologous recombination. Second, *iTol2* arms in opposing directions flanking an ampicillin resistance cassette were PCR amplified from the *iTol2* plasmid and introduced into the BAC backbone. Third, the reporter cassette was PCR amplified from the constructed *pIGCN21-Left recombination arm-Reporter/PolyA-FRT/Neo/FRT-Right recombination arm* and inserted into the BAC to replace the first exon or that with partial intron I of interested gene. Finally, the successful insertion of the reporter cassette was confirmed by PCR and sequencing. BAC clone sources, primer sequences, and insertion sites of the reporter cassette are listed in Supplementary Table 3. The *TgBAC(vglut2a:LOXP-DsRed-LOXP-GFP)ion18h* line was generated using a previously reported construct[95].

For the generation of *14×UAS-E1b:tdTomato-CAAX*, the tandem-dimer tomato (tdT) was PCR amplified with a 3' membrane tag encoding the *CAAX* box of human Harvey Ras (CTGAACCCTCCTGATGAGAGTGGCCCCGGCTGCATGAGCTGCAAGTGTGTGCTCTCC) and cloned into the *miniTol2-14×UAS-E1b* backbone from plasmid *miniTol2-UAS:GCaMP5*[96,97]. To label cerebellar cells, we generated the *Tg(5×UAS-hsp:lyn-tdTomato)* using zebrafish codon-optimized *lyn* as a membrane-bound signal[98]. For the generation of *14×UAS-E1b:sypb-EGFP,14×UAS-E1b:tdKatushka2-CAAX*, we cloned the PCR amplified *sypb-EGFP*[99] and *de novo* synthesized *tdKatushka2-CAAX* to the two sides of a bidirectional *14×UAS-E1b* in the *miniTol2* backbone.

Imaging

For live imaging, zebrafish larvae at 6 dpf were anesthetized with 0.02% tricaine methanesulfonate or immobilized with pancuronium dibromide (PCD, 1 mM), and embedded in 2–2.5% low-melting point agarose on a custom-made imaging chamber. Imaging was performed on an Olympus FV3000 or a Nikon A1R upright confocal microscope with a 20×

(1.0 N.A.) or a 25× (1.1 N.A.) water-immersion objective, respectively. For reference template construction, three overlapping image stacks along the anteroposterior axis were acquired at a voxel size of ~ 0.62 × 0.62 × 1 μm (*xyz*), covering the brain and approximately one third of the spinal cord. These were stitched together using either native imaging software or the Grid/Collection stitching plugin in Fiji. For single-neuron reconstruction, larvae were scanned at a voxel size of ~ 0.49 × 0.49 × 1 μm in a 1 × 2 or 1 × 3 tiled arrays depending on the projection range of the neuron. Laser intensity was progressively increased along the *z*-axis to compensate for fluorescence attenuation. The 405 nm, 488 nm, 561nm, and 594 nm diode-pumped solid state lasers were used to excite fluorophores of TagBFP, GCaMP6s/EGFP, tdTomato, and tdKatushka2, respectively.

Template generation and image registration

To generate the original dual-channel template *elavl3:H2B-GCaMP6s;vglut2a:DsRed*, we used the open-source Advanced Normalization Tools (ANTs) software running on the CEBSIT's Linux computing cluster. This software allows the creation of a multichannel template by using the shell script antsMultivariateTemplateConstruction2.sh[100]. Confocal images were resampled from ~0.62 × 0.62 × 1 μm (*xyz*) to 1 × 1 × 1 μm resolution before generating the template. In short, the template was created by shape-based averaging from 16 image scans of the double transgenic fish through an iterative process (see Extended Data Fig. 1a). In detail, an average image was first generated from the input fish scans by rigid alignment. Then, an iterative process began, which included deformable registration of each aligned scan to the average image based on the two expression patterns (1×1 weights). The resulting registered scans were then averaged for each expression pattern to form the new average image. This process continued until convergence was attained, as revealed by a growth plateau of the similarity scores between the average templates resulting from adjacent iterations using the normalized cross correlation (NCC) metric (see Extended Data Fig. 1b; see the section "Registration accuracy evaluation" in Methods).

Other reference templates in the common physical space (CPS) were generated similarly by first producing a two-channel, shape-based average, followed by transforming the target channel to the CPS via bridging with the *elavl3:H2B-GCaMP6s* or *vglut2a:DsRed* channel using the antsApplyTransforms function in ANTs. The number of fish used, iteration cycles, and bridging patterns for other reference templates in CPS are listed in Extended Data Fig. 1c. Additional templates, such as *isl2b* and *atoh7:GAL4* lines crossed to *Tg(4×nrUAS:GFP)* for labeling RGCs, were integrated into CPS via the *elavl3:NES-jRGECO1a* bridge template.

Image registration was performed using the antsRegistration function in ANTs[40], with

optimized parameters adapted from a previous study[44] for improved accuracy, particularly between live and fixed fish scans (see the section "Registration accuracy evaluation" in Methods). Registration proceeded in two parallelized steps using Slurm-based bash scripts: (1) rigid and affine (RA) registration (translation, rotation, anisotropic scale and shear), and (2) warp registration. This two-step pipeline enables optimization of the RA transformation before the computationally intensive warp step, thereby improving registration efficiency. To improve registration accuracy, a fish-body mask, created using CMTK's *levelset* and refined manually, was applied to both the reference and RA-registered images during warp registration to remove background fluorescence. For most neuron tracing datasets, the *elavl3:H2B-GCaMP6s* expression pattern in the CPS served as the registration template. For RGC datasets, a composite template (*elavl3:H2B-GCaMP6s* and *isl2b/atoh7:GAL4*) was used to enhance alignment accuracy in the tectal neuropil area.

The ANTs commands used are listed below:

(1) Two-channel template generation:
antsMultivariateTemplateConstruction2.sh -d 3 -b 1 -g 0.1 -i 10 -c 2 -j 16 -k 2 -w 1x1 -r 1 -n 0 -m CC -t SyN ${image-inputs}

(2) Rigid and affine registration:
antsRegistration --verbose 1--dimentionality 3 --float 1 --collapse-output-transforms 1 --output [${image-output}ra,${image-output}ra_warped.nrrd] --interpolation WelchWindowedSinc --use-histogram-matching 0 --initial-moving-transform [${template}, ${image-input},1] --transform Rigid[0.1] --metric MI[${template},${ image-input},1,32,Regular,0.25] --convergence [400 × 200 × 200 × 20,1e-8,10] --shrink-factors 12×8×4×2 --smoothing-sigmas 4×3×2×1vox -transform Affine[0.1] --metric MI[${template}, ${image-input},1,32,Regular,0.25] --convergence [400×200×200×20,1e-8,10] --shrink-factors 12×8×4×2 --smoothing-sigmas 4×3×2×1vox

(3) Warp registration:
antsRegistration -d 3 --float 1 --verbose 1 -o [${image-output}SyN,${image-output}SyN_warped.nrrd] -interpolation WelchWindowedSinc -use-histogram-matching 0 -r [${mask},${mask},1] -t SyN[0.2,6,0] -m CC[${template},${image-output}ra_warped.nrrd,1,2] -c [400 × 200 × 100 × 50 × 0,1e-7,10] -f 12×8×4×2×1 -s 5×3×2×1×0vox -x [${mask},${mask}]

(4) Apply transformation matrix to the image in a second channel:
antsApplyTransforms -d 3 --float -n WelchWindowedSinc -i ${image-input_second channel} -r ${template} -t ${image-output}SyN1Warp.nii.gz -t

${image-output}ra0GenericAffine.mat -o ${image-output_second channel}warped.nii.gz

Registration accuracy evaluation

We assessed the registration precision using the mean landmark distance (MLD) metric[44]. Taking the *elavl3:H2B-GCAMP6s* expression pattern as an example, we identified 13 widely distributed landmarks across the zebrafish brain (see Extended Data Fig. 2a–c). Each landmark was verified for recognizability by three independent annotators and had a mean positional deviation ranging from 1.69 to 5.10 μm (mean = 3.10 ± 1.10 μm). We manually marked the landmarks on both the reference template and unregistered individual scans using ImageJ. For each scan, a secondary mask channel was created by embedding 3-pixel cubes centered at each landmark position. After registering individual scans to the reference template, we applied the resulting transformation matrix to the mask channel. The landmark distance (LD) was calculated as the Euclidean distance between the geometric center of corresponding cubes in the registered and reference stacks. The MLD for each registered scan was calculated as the average of its 13 LD values.

To evaluate the registration accuracy during building the single E and I neuron atlas, we randomly selected 88 *elavl3:H2B-GCAMP6s* fish scans. The resulting MLDs ranged from 2.2 to 4.8 μm (mean = 3.28 ± 0.06 μm; see Extended Data Fig. 2f). For inter-atlas registration accuracy, we evaluated six expression patterns: *elavl3:H2B-FPs* (*FPs* include *GCaMP6s* and *RFP*), *elavl3:GECIs* (*GECIs* include *GCaMP6s*, *NES-jRGECO1a*, *GCaMP5G*, and *CaMPARI*), *vglut2a:DsRed*, *gad1b:EGFP*, *glyt2:GFP*, and *vmat2:GFP*. For each pattern, we marked 6–9 landmarks (45 in total) in the corresponding reference templates in the Z-Brain, ZBB, mapzbrain, and our own ZExplorer atlas (see Extended Data Fig. 1h,i). Not all six expression patterns were available for each comparison. The co-registration precision was computed as the mean of MLDs measured between matched expression patterns. The co-registration precision for Z-Brain, ZBB, and mapzebrain to our ZExplorer is 8.93 ± 2.27 μm, 8.69 ± 2.04 μm, and 7.73 ± 2.36 μm, respectively (see Extended Data Fig. 1k).

The normalized cross-correlation (NCC) was also used as a rapid, quantitative metric for evaluating registration accuracy, calculated via the similarity function in the Computational Morphometry Toolkit (CMTK). During registration using ANTs, we measured NCC after performing the RA registration. Scans with NCC_{RA} >0.55 (empirically determined) proceeded to the next step of warp registration (see Extended Data Fig. 2h), while those below the threshold were inspected manually to determine their suitability for subsequent warp registration.

Brain parcellation

To annotate the nervous system of larval zebrafish in 3D, we manually delineated the brain, partial spinal cord (segments 1–11), and peripheral ganglia into 68 anatomical regions

(comprising 173 parcellations). Segmentations was performed using the 3D slicer (https://www.slicer.org), an open-source platform for image processing and 3D visualization, in 3 orthogonal planes (i.e., horizontal, transverse, and sagittal).

Region boundaries were primarily defined based on established neuroanatomical references[27] and the reported Z-Brain ontology (https://zebrafishatlas.zib.de)[41]. Delineation was guided mainly by expression patterns of three key reference templates generated by ourselves (*elavl3:H2B-GCaMP6s*, *vglut2a:DsRed*, and *gad1b:EGFP*), as well as other transgenic line data incorporated in the CPS. Informative expression patterns were visualized in semi-transparent overlays, and each segmentation was illustrated in coordination with the surrounding ones. Besides, the medial octavolateralis nucleus (MON) was uniquely delineated based on afferent projections from octaval (gVIII) and lateral line (ALLG and PLLG) neurons in our single-neuron morphology atlas.

Initial segmentations were conducted in the horizontal (*xy*) plane, followed by iterative refinements across all three planes to ensure anatomical accuracy and smooth boundaries. The final parcellations were jointly smoothed using a custom multiple 3D median filter, resulting in a comprehensive, non-overlapping, and gap-free set of nervous system regions. The complete ontology of annotated regions in the CPS is listed in Supplementary Table 2.

Cell counting and registration

To construct a nervous system-wide neuronal cytoarchitecture, individual somata were manually annotated based on the centroid of fluorescent signals in 3D image stacks using the Cell Counter plugin in Fiji. We mapped five neuronal populations: *elavl3+*, *vglut2a+*, *vglut2b+*, *gad1b+*, and *glyt2+*, corresponding to the expression patterns of *elavl3:H2B-GCaMP6s*, *vglut2a:DsRed*, *vglut2b:GAL4FF*, *gad1b:EGFP/gad1b:GAL4-VP16*, and *glyt2:GFP*, respectively. For each neuronal population, four individual fish were quantified. Each fish scan was annotated by one researcher and independently reviewed by two others before final confirmation. The counts for *vglut2a+* and *vglut2b+* neurons were combined to represent the excitatory neuronal cytoarchitecture.

To register the cytoarchitecture data into the CPS, the expression pattern used for cell annotation or the alternative imaging channel that matches one of the two original reference templates was first registered to the CPS. The resulting transformation matrix was then applied to the digital cytoarchitecture data (a file containing the coordinates of annotated somata) using the antsApplyTransformsToPoints function in ANTs:

```
antsApplyTransformsToPoints -d 3 -i ${point-input} -o ${point-output}warped.csv -t [${image-output}ra0GenericAffine.mat,1]
antsApplyTransformsToPoints -d 3 -i ${point-output}warped.csv -o ${point-output}warped_SyN.csv -t ${image-output}SyN1InverseWarp.nii.gz
```

Neuronal morphology reconstruction and registration

Individual neurons suitable for reconstruction were manually selected and semi-automatically traced using the Simple Neurite Tracer (SNT) plugin in Fiji[101]. The resulting neuron skeletons, composed of interconnected nodes, were saved as individual SWC files[102]. The soma radius for each neuron was determined by averaging the semi-major and semi-minor axes of the soma in its maximum-intensity-projection image, and this value was written into the SWC file. Each neuron was traced by a single annotator and independently reviewed by two experienced experts. On average, reconstruction of a single neuron required ~1.2 hours, with each fish providing ~1.5 reconstructions (total of 13,429 fish for 20,011 neuron reconstructions). Neurons with deep ventral and/or caudal spinal cord projections extending beyond the imaging volume were marked as incomplete. Their inclusion in analyses was determined on case-by-case basis.

For neurons with presynaptic labeling (Sypb-EGFP), we manually annotated the node closest to the geometric center of each fluorescently discrete Sypb-EGFP punctum as a presynaptic site and assigned the type identifier as 7 in the SWC files. The type identifiers for soma, axon, and dendrite are 1, 2, and 3, respectively.

Prior to registration, each neuron reconstruction was preprocessed using smooth_neuron (σ = 1) and resample (step size = 1) functions in the R package nat. Presynaptic site coordinates were preserved during this step. The preprocessed neuron skeleton was then registered to the CPS using the antsApplyTransformToPoints function in ANTs (see the section “Cell counting” in Methods).

Neuronal polarity identification

To identify neuronal polarity (i.e., dendritic *vs* axonal compartments), we trained a machine learning-based classifier using neuron reconstructions with dendrite-axon (DA) annotations obtained from morphology-presynaptic site (Sypb-EGFP) double-labeling data. Each neuron was represented as a tree graph, from which six morphological parameters were extracted to train the classifier: (1) terminal branch length, (2) branch point order, (3) path distance from soma to terminals, (4) Euclidean distance from soma to terminals, (5) normalized terminal coordinates relative to soma, and (6) maximum branch length along terminal paths. Because each node along a terminal path shares the same polarity identity as the terminal, we classified only the terminals and assigned all upstream nodes accordingly, resulting in some nodes being shared between axonal and dendritic branches.

We implemented this classification model based on the support vector machine (SVM) and used the reconstruction of 70 neurons to train the classifier, achieving over 95% accuracy on a test dataset. This automatic classification method enables rapid and reliable identification of neuronal polarity, particularly suited for large-scale datasets. Final results were manually verified.

Neuron projection analysis

We measured the projection strength of each neuron to target regions using axonal projection length (APL). This measure includes only axon compartments associated with terminals inside the region, excluding those merely passing through the region. To mitigate potential errors caused by registration or parcellation imprecision, we only considered a neuron to project into a region if its axonal length within that region exceeded 10 μm. The neuron cluster-to-region projection strength was calculated by summing the projection strength of all neurons in the cluster and normalizing by cluster size:

Neuron classification

We performed classification analysis using mirrored data[9,50]. Briefly, we horizontally flipped the *elavl3:H2B-GCaMP6s* reference template and registered the flipped stack to the original stack using ANTs to obtain a mirroring transformation matrix. Reconstructed and registered neurons were divided into left and right groups based on soma location relative to a mid-sagittal plane, fitted from scattered midline points across horizontal sections of the brain and spinal cord in the CPS. Neurons on either side were flipped to the opposite side and registered to the CPS using the antsApplyTransformToPoints function in ANTs with the mirroring matrix.

We developed an unsupervised learning-based neuron classification algorithm termed MBLAST by using neuron morphology and soma position properties. Requiring no prior information, this algorithm discovers clusters and detects the noise points on large databases efficiently. It consists of two functions: (1) detecting new clusters from neuronal populations; (2) assigning new neurons to existing clusters. The core of the algorithm is a shape-based distance metric inspired by the Hausdorff distance[103]. We considered each neuron P as a trajectory consisting of tracing points with a size of n_P. The directional distance from P_1 to P_2 was defined as:

$$dist(P_1, P_2) = \sum_{i=1}^{n_{P_1}} \arg\min_{1 \le j \le n_{P_2}} \frac{\| p_i - q_j \|}{n_{P_1}}$$

where $p_i \in P_1$, $q_j \in P_2$. The overall distance between two neurons P_1 and P_2 was defined as:

$$D_{P_1,P_2} = \max(dist(P_1, P_2), dist(P_2, P_1))$$

This metric is sufficiently sensitive to capture the similarity of neuron shapes and easy to compute. Besides, this distance score requires no parameter and thus is easily applied to construct a similarity matrix for any neuron reconstruction dataset.

Morphological clustering was performed using DBSCAN (Density-Based Spatial Clustering of Applications with Noise)[104], a density-based algorithm effective in discovering clusters of arbitrary shape. In order to find clusters with different densities, we implemented a

multiscale DBSCAN approach, iteratively clustering neurons with different global density parameters. To take soma position into account, both morphological and soma-position-based clustering were performed independently; neurons were assigned to the same cluster if both criteria matched. The resulting clusters were manually curated to form the final basic neuron clusters.

To classify newly reconstructed neurons, we developed a probabilistic query method. For each existing cluster *C*, we defined its intra-cluster similarity distribution as *D(C)*. For an unclassified neuron n, we computed its distance to each neuron $n_c \in C$, and evaluated the probability for n belongs to C as: $P(\mathrm{n} \in \mathrm{C}) = \max_{n_c \in C} \int_x^{+\infty} p_{D(C)}(x)dx$, where $x = dist(n, n_c)$. Neuron n was assigned to the cluster with the highest probability above a custom threshold, and then manually reviewed for confirmation.

Descending/ascending and ipsilateral/contralateral projection analysis of morphological clusters

First, we calculated the neuron-to-region projection strength APL_{ij} for each neuron i in morphological cluster c projecting to region j. Second, we annotated each APL_{ij} as either APL_{ij}^{Desc} or APL_{ij}^{Asc} based on the relative anteroposterior position of the neuron soma and the target region centroid. The cluster-to-region descending and ascending projection strength were calculated as $APL_{cj}^{Desc} = \sum APL_{ij}^{Desc}$ and $APL_{cj}^{Asc} = \sum APL_{ij}^{Asc}$, respectively. Then the cluster-to-region desc-/ascending preference index was calculated as:

$$I_{cj}^{Desc/Asc} = \frac{APL_{cj}^{Desc} - APL_{cj}^{Asc}}{APL_{cj}^{Desc} + APL_{cj}^{Asc}}$$

Similarly, each APL_{ij} was also separated into ipsilateral (APL_{ij}^{Ipsi}) and contralateral (APL_{ij}^{Contra}) components, depending on whether the projection was to the same or opposite hemisphere as the soma. We calculated the total ipsilateral and contralateral projection strengths from cluster to region as $APL_{cj}^{Ipsi} = \sum APL_{ij}^{Ipsi}$ and $APL_{cj}^{Contra} = \sum APL_{ij}^{Contra}$, respectively. The cluster-to-region ipsi-/contralateral preference index was calculated as:

$$I_{cj}^{Ipsi/Contra} = \frac{APL_{cj}^{Ipsi} - APL_{cj}^{Contra}}{APL_{cj}^{Ipsi} + APL_{cj}^{Contra}}$$

Neuronal connectivity analysis

We utilized axo-dendritic spatial proximity to infer neuronal connections. The distance was measured between compartments on axonal and dendritic branches. To ensure specificity, only axonal branches with terminal endings were included. A connection was defined when a pair of axonal and dendritic compartments was separated by less than 2 μm. The connection strength between individual neurons was quantified as the number of such compartment pairs

(≥1).

The mesoscale connection strength between neuronal clusters was calculated by summing the connection strength of all connected neuron pairs and normalizing by the number of neuron pairs. Two additional metrics were used to filter the connectivity between neuronal clusters: (1) connection ratio, the percentage of connected neurons in each cluster. The larger of the two percentages must be at least 20%; (2) divergence and convergence (D&C) indices, the number of connected neuron pairs divided by the number of neurons participating in input and output clusters, respectively. The D or C index must be larger than 1.

Interregional connectivity analysis

Interregional connection strength is a concept used to measure the connectivity between any two regions, which can be defined in different ways[9,105]. Here, we proposed a metric termed "complete axonal projection length (CAPL)", representing an estimate of the total macroscale connection strength between brain regions under endogenous neuronal population size. The computation of CAPL involves four main steps:

First, we generated the neuron-to-region projection strength matrix by calculating axonal projection length for each neuron-region pair:

$$APL_{neuron\rightarrow region} = \begin{bmatrix} apl_{00} & \cdots & apl_{0R} \\ \vdots & apl_{ij} & \vdots \\ apl_{N0} & \cdots & apl_{NR} \end{bmatrix}$$

where N is the number of sampled neurons, R is the number of regions, and apl_{ij} is the axonal projection length of neuron i inside region j and calculated as:

$$apl_{ij} = \begin{cases} \sum_{b}^{B} l_{abp} * c, & | \; where\ B\ is\ axon\ branch\ number \\ 0, & | \; if\ neuron\ i\ is\ a\ local\ interneuron\ for\ region\ j \\ 0, & | \; if\ final\ apl_{ij}\ is\ below\ threshold \end{cases}$$

Here, l_{abp} is the length of axon branches of neuron i inside region j, and c is a coefficient which is 0 when axon branch just passes through the region, or 1 otherwise.

Second, we obtained the region-to-region connection strength by summing the axonal projection lengths of all sampled neurons with soma located in the source region and projecting to the target region:

$$APL_{region\rightarrow region} = \begin{bmatrix} apl_{00} & \cdots & apl_{0R} \\ \vdots & apl_{kj} & \vdots \\ apl_{R0} & \cdots & apl_{RR} \end{bmatrix}$$

where $apl_{kj} = \sum_{i}^{N} apl_{ij}$, and N is the number of neurons inside source region k.

Third, we normalized the region-to-region connection strength by dividing the number of sampled neurons inside the source region:

$$NAPL_{region \to region} = \begin{bmatrix} napl_{00} & \cdots & napl_{0R} \\ \vdots & napl_{kj} & \vdots \\ napl_{R0} & \cdots & napl_{RR} \end{bmatrix}$$

where $napl_{kj} = \frac{apl_{kj}}{SNC}$, and SNC is the number of sampled neurons inside source region k.

Finally, we calculated the region-to-region CAPL by scaling the normalized connection strength with the total number of neurons in the source region (from cytoarchitecture data):

$$CAPL_{region \to region} = \begin{bmatrix} capl_{00} & \cdots & capl_{0R} \\ \vdots & capl_{kj} & \vdots \\ capl_{R0} & \cdots & capl_{RR} \end{bmatrix}$$

where $capl_{kj} = napl_{kj} * T$, and T is the total number of neurons inside source region k.

To derive ipsilateral and contralateral CAPL, each neuron's projection strength was partitioned based on its position relative to the aforementioned mid-sagittal plane. The ipsilateral and contralateral CAPL were then calculated separately using the same procedure as for total CAPL. The interregional ipsi-/contralateral preference index was calculated as:

$$I^{Ipsi/Contra}_{region \to region} = \frac{CAPL^{Ipsi}_{region \to region} - CAPL^{Contra}_{region \to region}}{CAPL^{Ipsi}_{region \to region} + CAPL^{Contra}_{region \to region}}$$

Region pairs were annotated as descending or ascending based on the relative anteroposterior positions of the source and target regions.

Network hub analysis

Network hubs are considered as nodes in the network with high centrality for information transfer. In this weighted network, we defined the path distance between two nodes as the sum of the reciprocals of directed connection strength along the path. We scored node centrality based on nine metrics: (1) input strength, total connection strength from directly connected upstream nodes; (2) output strength, total connection strength to directly connected downstream nodes; (3) input degree, number of upstream nodes directly connected to the target node; (4) output degree, number of downstream nodes directly connected to the target node; (5) betweenness centrality, frequency with which a node lies on the shortest paths between all other node pairs; (6) closeness, ratio of the number of reachable downstream nodes to the average shortest path distance to those nodes; (7) PageRank, importance of a node based on the structure of its connections, an algorithm originally developed for ranking web pages[106]; (8) clustering, fraction of bidirectional triangular motifs involving the target node; (9) vitality, change in the total shortest-path distance between all nodes when the target node is removed. Each metric was normalized within its group. The hub score of a node was defined as the sum of its normalized scores across all nine metrics. Nodes with above-mean scores for all metrics were defined as network hubs.

In the interregional hub network, edge width represents the weighted betweenness centrality of directed connections, indicating their influence on the network-wide information

flow. Edges with higher values appear more frequently in the shortest paths and serve as key bridges between subnetworks.

Statistical analysis

No randomization and blinding were used during data collection and analysis as there is a single experimental condition for all acquired data. The statistical analysis was performed using Python or GraphPad Prism. The central mark, bottom, and top of the boxplot indicate the median, first, and third quartiles, respectively. The height and error bars of the bar plots, as well as the descriptive statistics in the main text, represent mean ± SEM. Statistical significance is defined as $P < 0.05$. The specific statistical tests and *P*-value ranges are provided in the corresponding figure legends. Sample sizes (n) refer to the number of samples, fish, or cells, as specified in the relevant figure and/or figure legend.

Reporting summary

Further information on research design is available in the Nature Port-folio Reporting Summary linked to this article.

Data availability

Plasmids and BAC DNA constructs generated in this study have been deposited to Addgene (accession pending) and will be available upon request. Transgenic zebrafish lines generated in this study have been deposited to China Zebrafish Resource Center (CZRC) and are available upon request. All datasets, including reference transgenic line images, neuroanatomical parcellations, cytoarchitectures, and neuron reconstructions, have been deposited in the CEBSIT brain science data archive. They are accessible through the ZExplorer web portal at: https://zebrafish.cn/LM-Atlas/EI.

Code availability

All source codes and algorithms for neuronal polarity identification, morphology-based neuron classification, network motif and hub analysis are available at https://github.com/soaringdu/Proj-AtlasEI. Data visualization was performed using BrainAtlas Viewer (BrAVe)[107], a custom software built on the open-source ParaView. BrAVe supports visualization and analysis of neuron spatial distribution, morphological characterization, interhemispheric crossings, neuron-to-region projection strength, neuron clustering, neuronal wiring, and interregional connectivity.

References (Methods)

86. Freeman, J. *et al.* Mapping brain activity at scale with cluster computing. *Nat. Methods* **11**, 941–950 (2014).
87. Wang, M. *et al.* Different lineage contexts direct common pro-neural factors to specify distinct retinal cell subtypes. *J. Cell Biol.* **219**, (2020).
88. McLean, D. L., Fan, J., Higashijima, S. I., Hale, M. E. & Fetcho, J. R. A topographic

map of recruitment in spinal cord. *Nature* **446**, 71–75 (2007).

89. Ben Fredj, N. *et al.* Synaptic activity and activity-dependent competition regulates axon arbor maturation, growth arrest, and territory in the retinotectal projection. *J Neurosci* **30**, 10939–10951 (2010).
90. Del Bene, F. *et al.* Filtering of Visual Information in the Tectum by an Identified Neural Circuit. *Science* **330**, 669–673 (2010).
91. Akitake, C. M., Macurak, M., Halpern, M. E. & Goll, M. G. Transgenerational analysis of transcriptional silencing in zebrafish. *Dev. Biol.* **352**, 191–201 (2011).
92. Feng, J. *et al.* A Genetically Encoded Fluorescent Sensor for Rapid and Specific In Vivo Detection of Norepinephrine. *Neuron* **102**, 745-761.e8 (2019).
93. Wen, L. *et al.* Visualization of monoaminergic neurons and neurotoxicity of MPTP in live transgenic zebrafish. *Dev. Biol.* **314**, 84–92 (2008).
94. Suster, M. L., Abe, G., Schouw, A. & Kawakami, K. Transposon-mediated BAC transgenesis in zebrafish. *Nat. Protoc.* **6**, 1998–2021 (2011).
95. Satou, C., Kimura, Y. & Higashijima, S. ichi. Generation of multiple classes of V0 neurons in Zebrafish spinal cord: Progenitor heterogeneity and temporal control of neuronal diversity. *J. Neurosci.* **32**, 1771–1783 (2012).
96. Yao, Y. *et al.* Visual Cue-Discriminative Dopaminergic Control of Visuomotor Transformation and Behavior Selection. *Neuron* **89**, 598–612 (2016).
97. Balciunas, D. *et al.* Harnessing a high cargo-capacity transposon for genetic applications in vertebrates. *PLoS Genet* **2**, e169 (2006).
98. Köster, R. W. & Fraser, S. E. Tracing transgene expression in living zebrafish embryos. *Dev. Biol.* **233**, 329–346 (2001).
99. Meyer, M. P. & Smith, S. J. Evidence from In Vivo Imaging That Synaptogenesis Guides the Growth and Branching of Axonal Arbors by Two Distinct Mechanisms. *J. Neurosci.* **26**, 3604–3614 (2006).
100. Avants, B. B. *et al.* The optimal template effect in hippocampus studies of diseased populations. *Neuroimage* **49**, 2457–2466 (2010).
101. Arshadi, C., Günther, U., Eddison, M., Harrington, K. I. S. & Ferreira, T. A. SNT: a unifying toolbox for quantification of neuronal anatomy. *Nat. Methods* **18**, 374–377 (2021).
102. Cannon, R. C., Turner, D. A., Pyapali, G. K. & Wheal, H. V. An on-line archive of reconstructed hippocampal neurons. *J. Neurosci. Methods* **84**, 49–54 (1998).
103. Huttenlocher, D. P., Klanderman, G. A. & Rucklidge, W. J. Comparing images using the Hausdorff distance. *IEEE Trans. Pattern Anal. Mach. Intell.* **15**, 850–863 (1993).
104. Sander, J., Ester, M., Kriegel, H. P. & Xu, X. Density-based clustering in spatial databases: The algorithm GDBSCAN and its applications. *Data Min. Knowl. Discov.* **2**, 169–194 (1998).
105. Oh, S. W. *et al.* A mesoscale connectome of the mouse brain. *Nature* **508**, 207–214 (2014).
106. Page, L., Brin, S., Motwani, R. & Winograd, T. The PageRank Citation Ranking: Bringing Order to the Web. *Tech. Report. Stanford InfoLab.* (1999).
107. Wang, Y.-F. *et al.* BrAVe: a unified framework for 3D interactive and integrative exploration and analysis of cross-modal brain atlas data. ***Co-submitted to Nature.***

108. Koyama, M., Kinkhabwala, A., Satou, C., Higashijima, S. I. & Fetcho, J. Mapping a sensory-motor network onto a structural and functional ground plan in the hindbrain. *Proc. Natl. Acad. Sci. U. S. A.* **108**, 1170–1175 (2011).
109. Wang, W. C. & McLean, D. L. Selective Responses to Tonic Descending Commands by Temporal Summation in a Spinal Motor Pool. *Neuron* **83**, 708–721 (2014).

Acknowledgements

We are grateful to Drs. Shin-ichi Higashijima and Wei Hu for sharing the BAC and plasmid DNA, Misha Ahrens, Joseph Fetcho, Bo Zhang, and Marnie Halpern for sharing fish lines, and Herwig Baier, Harold Burgess, Florian Engert, and Alexander Schier for sharing line atlas data. We would like to thank Florian Engert for feedback on the brain parcellation and Harold Burgess for feedback on the evaluation of registration precision using landmarks. We would like to thank Ji-Wen Bu, Ye Hua, and Shi-Rong Jin for help with fish husbandry and maintenance; Zhi Zeng and Jian He for providing reconstruction assistance; Ying-Ling Chen, Ying-Ying Wu, Chen-Yan Li, Hua-Qing Shi, and Hong-Yu Li for additional reconstruction work; Ying-Jie Ma and Ying Wang for providing imaging and brain parcellation assistance; Jia-Fei Wei for help with data analysis; and Xing Li for help in the early stages of implementing the interactive web portal. This work utilized the high-performance computing capabilities of the Linux cluster at the Center for Data and Computing in Brain Science at CEBSIT. This work was supported by STI2030-Major Projects (2021ZD0204500, 2021ZD0204502, and 2022ZD0209600), the National Natural Science Foundation of China (32321003, 62320106010, and 62276253), the National Key R&D Program of China (2018YFA0801001), Shanghai Municipal Science and Technology Major Project (18JC1410100 and 2018SHZDZX05), and Key Research Program of Frontier Sciences (QYZDYSSW-SMC028) and Strategic Priority Research Program (XDB32010200) of Chinese Academy of Sciences. X.F.D. is also supported by the Youth Innovation Promotion Association, Chinese Academy of Sciences.

Author contributions

J.L.D. conceptualized the project. X.F.D. and J.L.D. conceived the experiments and analysis and wrote the manuscript with input from P.J., Y.F.W., and Y.M.. X.F.D. managed the project with input from J.L.D and Z.F.Y.. Z.F.Y. and X.F.D. managed the development of the ZExplorer online platform. Z.F.Y. developed the two-channel template generation and high-precision alignment of 3D images required for atlasing transgene, cell-counting, and neuron tracing data. W.L.L. developed the methods for neuron polarity identification, neuron morphological classification, and network analysis with input from X.F.D. and Z.F.Y.. Z.F.Y. and T.L.C. performed the registration precision evaluation. X.F.D. and M.Q.C. conducted the brain parcellation and annotation with input from Z.F.Y., Y.F.W., D.Y.L., L.J.C., S.J.W., Y.C.G., T.L.C., and Q.M.Z.. X.Y.N. conducted the nervous system-wide cell counting.

H.Y.H., and J.H. developed genetic tools for transient microinjection and transgenic line generation. X.D.Z., Y.L. and J.H. generated transgenic lines. Z.M.J. and X.D.Z. conducted the microinjection and sample pre-screening with input from X.F.D., X.L.S., X.Y.Q., and W.Z.. H.L.W., H.A.R., R.Q.W., R.Z., X.L.P., L.W., M.Y.Z., T.L.C., and X.Y.S. conducted the sample preparation and acquired the live imaging data with input from W.Z., X.F.D., X.L.S, and Q.M.Z.. T.T.Z., Y.W.Z., and X.Y.N. conducted the neuron reconstruction with input from X.F.D. and X.L.S.. C.X.J. produced the videos about the experimental pipeline and designed the web interface with input from X.F.D., Y.F.W., and J.L.D.. J.W.H., W.D., and L.Q.Q. conducted the implementation of the interactive web portal with input from Z.F.Y.. X.F.D. conducted the analyses and made the illustrations with input from M.Q.C., W.L.L., T.L.C., P.J., X.Y.N., and Y.W.Z..

Competing interests

The authors declare no competing interests.

Figures and Legends

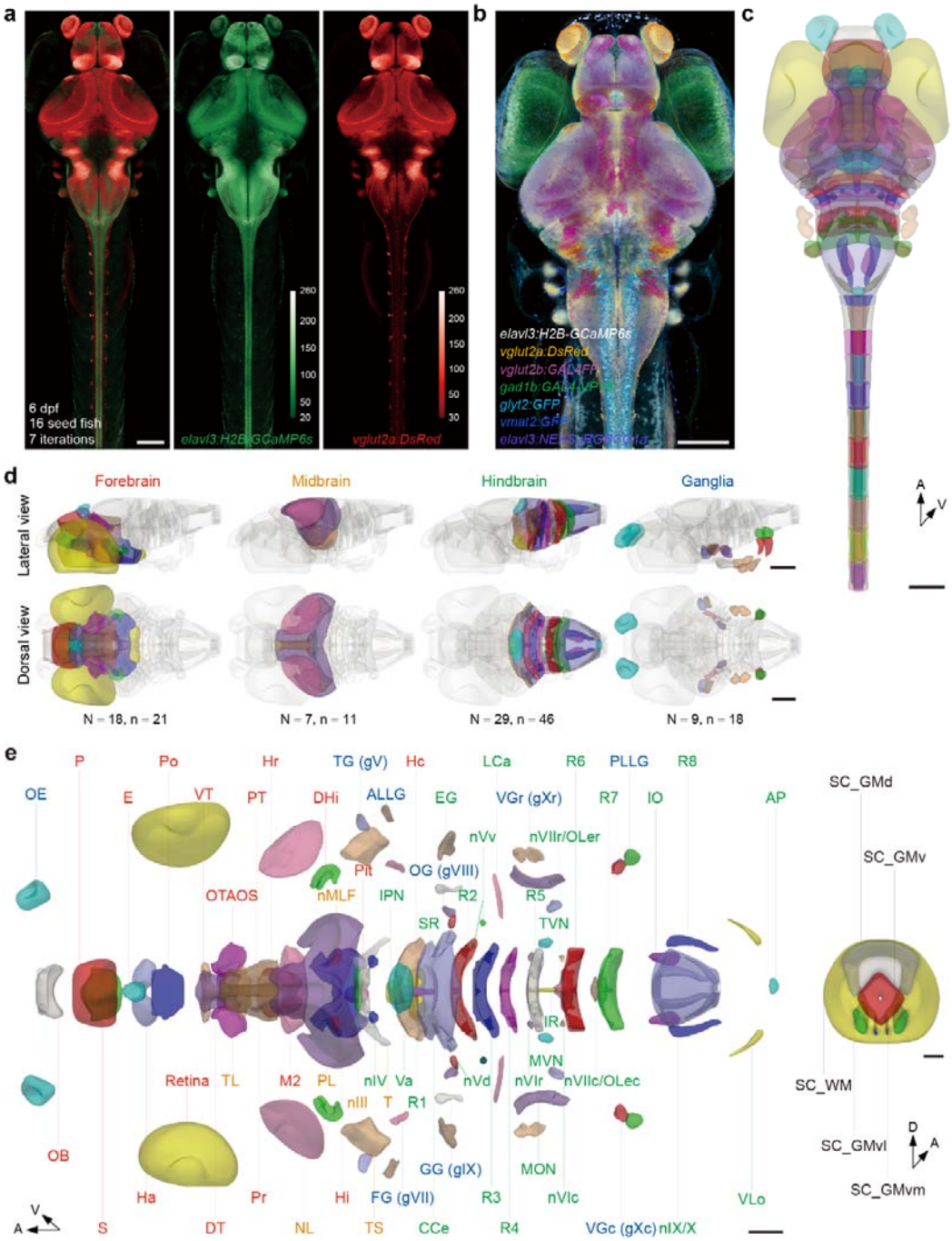

Fig. 1 | The common physical space of the larval zebrafish nervous system.

a, Volume rendering of the zebrafish CPS with two reference templates, derived from two original gene expression patterns (*elavl3:H2B-GCaMP6s* and *vglut2a:DsRed*) at 6 dpf (dorsal view). 16 seed fish images were iterated 7 times. Color-coded scale bars: image intensity encoded as 8-bit values.

b, Composite volume rendering of 7 transgenic reference templates aligned to the CPS (dorsal view). A partial spinal cord (SC) is shown.

c, Dorsal view of 173 non-overlapping, gap-free parcellations (n in **d**,**e**) of the nervous system in the CPS, color-coded by anatomical regions (N in **d**,**e**).

d, Lateral and dorsal views of brain regions in the forebrain, midbrain, hindbrain, and peripheral ganglia. N, number of anatomical regions; n, number of parcellations (bilateral instances counted separately).

e, Dorsal view of the radially disassembled brain and peripheral regions (left) and transverse view of SC regions (right), showing a detailed representation of regions with annotations.

Scale bars: 50 μm (**e**, the transverse view of the SC), 100 μm (**a–d** and **e** left). A, anterior; D, dorsal; V, ventral. See also Extended Data Fig. 1, Supplementary Videos 1 and 2, and Supplementary Table 2.

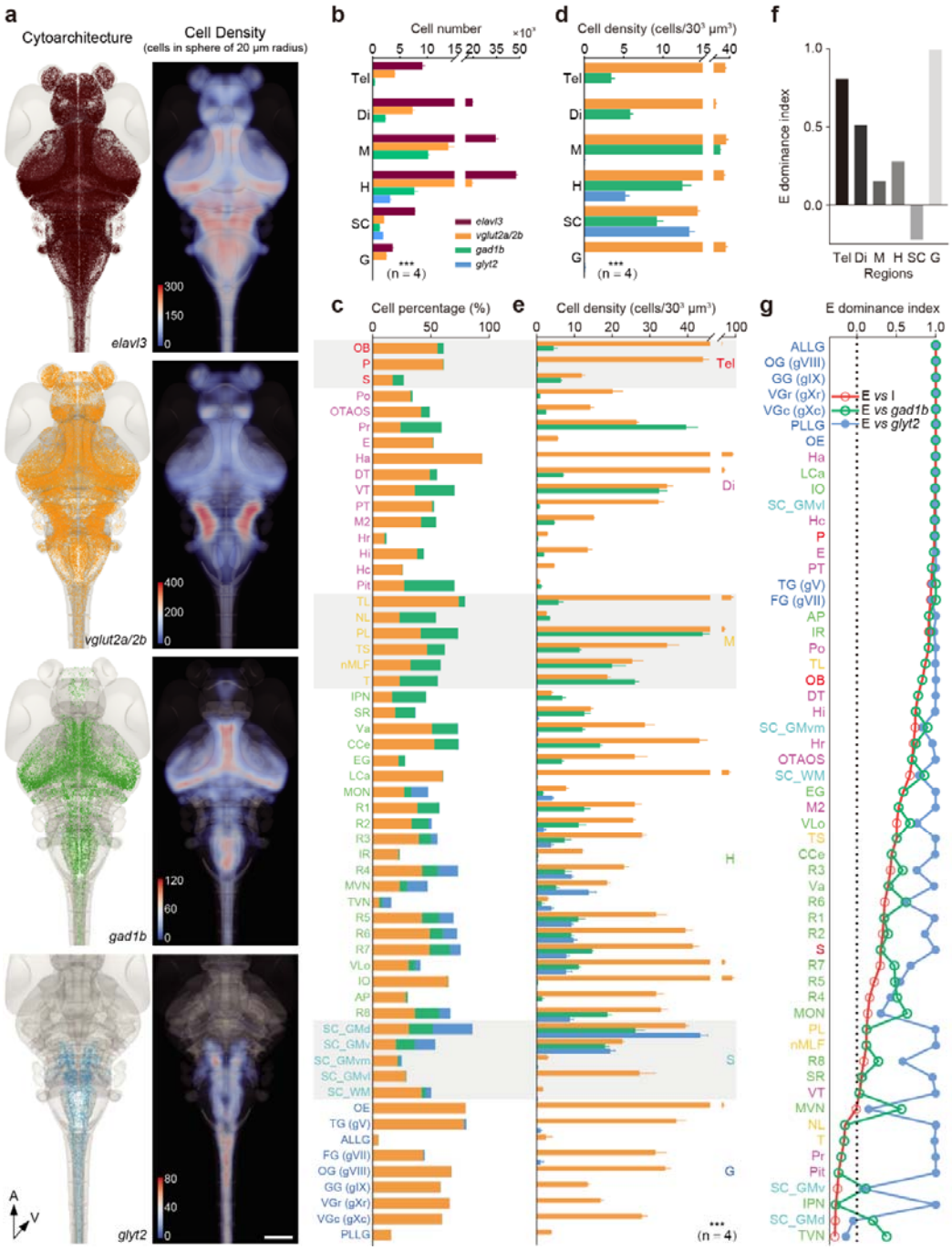

Fig. 2 | Cytoarchitecture atlases of E and I neurons.

a, Volume rendering of cell somata (left) and density maps (right) of for total (*elavl3*), glutamatergic (*vglut2a/2b*), GABAergic (*gad1b*), and glycinergic (*glyt2*) neurons in 6-dpf larvae. Each larva was aligned to the CPS. Only a partial SC is shown.

b, Cell number distributions across primary brain subdivisions (Tel, Di, M, and H), SC segments 1–11, and peripheral ganglia (G), showing global significant differences both among regions and among glutamatergic, GABAergic, and glycinergic neurons. Tel, telencephalon; Di, diencephalon; M, midbrain; H, hindbrain.

c, Percentage composition of E and I neurons (relative to total *elav3* neurons) across 57 anatomical regions. The cranial motor regions are merged into higher order regions, and the retina is not included.

d,**e**, Density (per 30^3 μm^3) of E and I neurons across 6 high-level (**d**) and 57 low-level regions (**e**), showing global significant differences both among regions and among glutamatergic, GABAergic, and glycinergic neurons.

f,**g**, E neuron dominance index, calculated as $(N_E-N_I)/(N_E+N_I)$, across 6 high-level (**f**) and 57 low-level regions (**g**). N_E, number of excitatory neurons; N_I, number of inhibitory (GABAergic + glycinergic, **f**), or GABAergic and glycinergic neurons (**g**). In (**g**), the indices are ranked in descending order of their values. Red: E *vs* I; Green, E *vs* GABAergic; Blue, E *vs* glycinergic.

Scale bar: 100 μm (**a**). A, anterior; V, ventral. Region labels on the *y*-axis are color-coded by the attribution of high-level regions (**c**,**e**,**g**). Data are averaged from 4 animals per group. ***$P < 0.001$ (Two-way ANOVA with Tukey's post hoc multiple comparison test). Error bars represent mean ± SEM. See also Supplementary Video 3 and Supplementary Table 2.

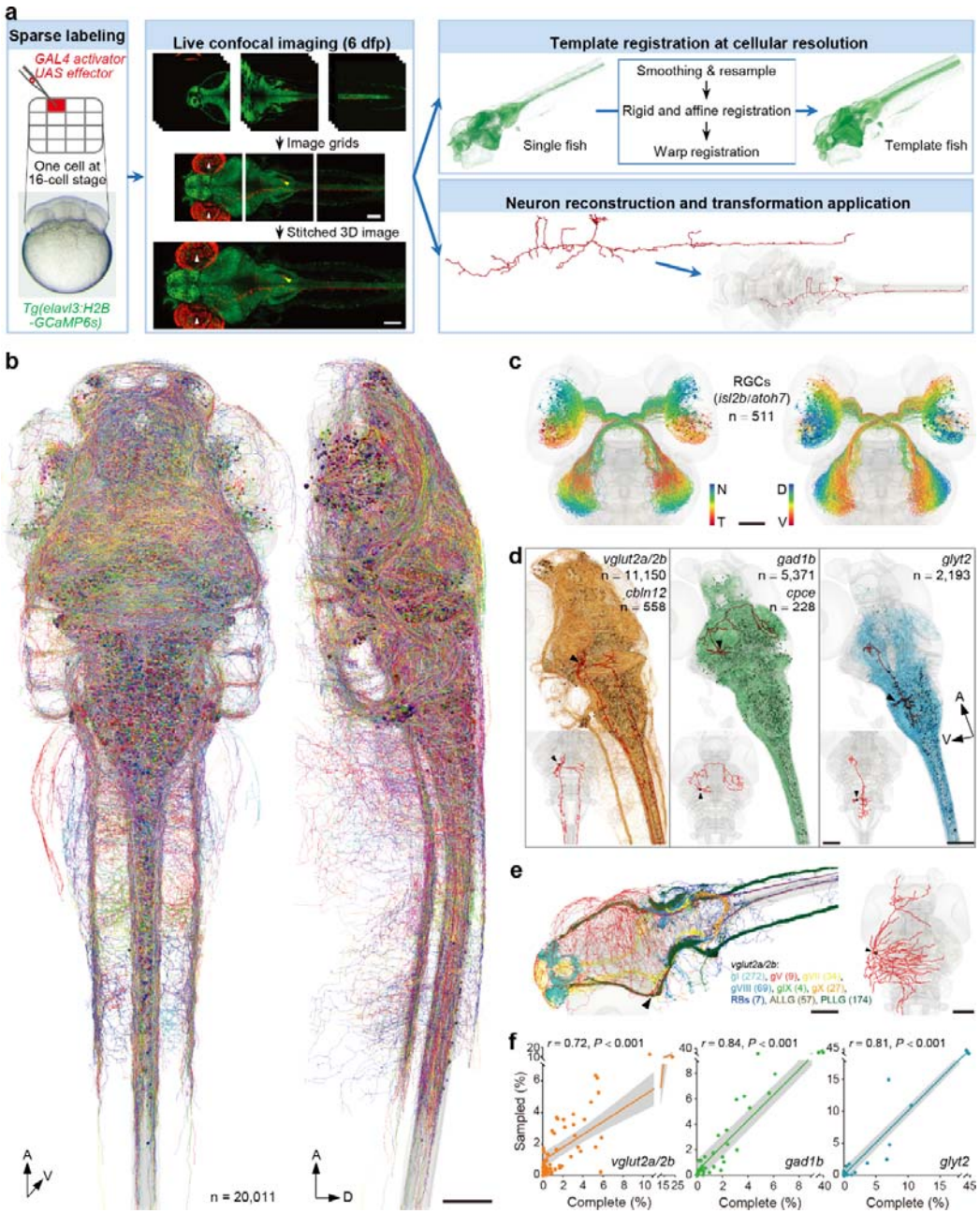

Fig. 3 | Single E and I neuron morphology atlases.

a, Pipeline of building single-neuron morphology atlases, including sparse labeling of neurons, 3D live imaging, neuron reconstruction, and alignment to the CPS. White arrowheads: autofluorescence of the eyeballs.

b, 3D visualization (left, dorsal view; right, lateral view) of 20,011 reconstructed E and I neurons from 13,429 fish, aligned to the CPS. Neurons are randomly color-coded.

c, RGCs (*isl2b*, n = 470; *atoh7*, n = 41) color-coded by soma position along the nasal-temporal (left) and dorsal-ventral (right) axes, displaying spatial topography.

d, Single-neuron atlases of excitatory (left: *vglut2a/2b*, n = 11,150; *cbln12*, n = 558), GABAergic (middle: *gad1b*, n = 5,371; *cpce*, n = 228) and glycinergic (right: *glyt2*, n = 2,193)

inhibitory neurons. Example neuron tracings are shown in red in the main panels and in the insets, with black arrowheads indicating the soma.

e, Map of sensory neurons including color-coded cranial sensory (including gI, gV, gVII, gVIII, gIX, and gX), Rohon-Beard (RB), and lateral line ganglion neurons (including ALLG and PLLG). Right, example neuron tracing. All sensory neurons are marked by *vglut2a/2b*. The number in the parentheses indicate the neuron number. gI, gV, gVII, gVIII, gIX, gX: ganglion of the cranial nerve I, V, VII, VIII, IX or X; ALLG, PLLG: anterior or posterior lateral line ganglion.

f, Correlation of relative regional distributions between sampled and complete neurons across 52 anatomical regions (sub-regions in the SC and vagal ganglia were merged). Left, glutamatergic; Middle, GABAergic; Right, glycinergic. Each dot represents the data for a single anatomical region. Pearson correlation and linear fitting revealed a significant correlation. Sampled and complete neurons refer to the reconstructed neurons (**d**) and counted neurons in cytoarchitectures (see Fig. 2a–c), respectively.

Scale bars: 50 μm (**c**), 100 μm (**a**,**b**,**d**,**e**). n, the number of neurons shown. A, anterior; D, dorsal; N, nasal; T, temporal; V, ventral. See also Extended Data Figs. 2 and 3, and Supplementary Videos 4 and 5.

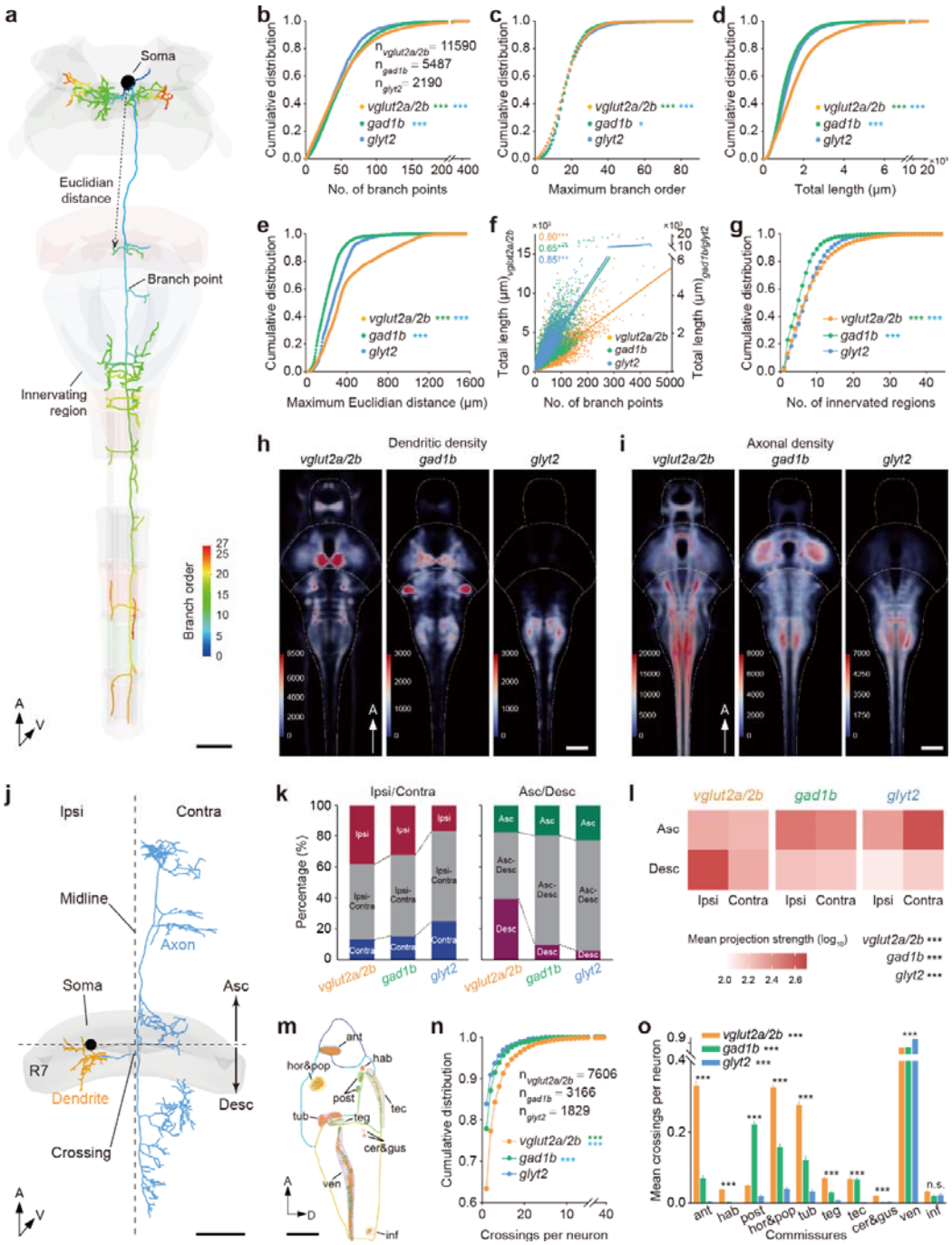

Fig. 4 | Distinct morphological features, dendrite-axon distribution and axonal projection patterns of E and I neurons.

a, Volume rendering of a single reconstructed *vglut2a* neuron in the nucleus of the medial longitudinal fasciculus (nMLF) and its innervating brain regions. Neurites are color-coded by branch order.

b–**e**, Cumulative distribution of four morphological parameters in E (*vglut2a/2b*) and I (*gad1b* and *glyt2*) neurons, showing differences in structural complexity (**b**,**c**) and size (**d**,**e**). Color asterisks represent corresponding inter-cell population comparison (Kolmogorov-Smirnov test). Mean number of branch points in **b**: *vglut2a/2b* (54.2 ± 0.4) > *gad1b* (53.2 ± 0.5) > *glyt2*

(48.2 ± 0.7); Mean maximum branch order in **c**: *glyt2* (18.5 ± 0.2) > *gad1b* (17.9 ± 0.1) > *vglut2a/2b* (17.4 ± 0.1); Mean total length in **d**: *vglut2a/2b* (1764 ± 13 μm) > *glyt2* (1296 ± 18 μm) > *gad1b* (1236 ± 15 μm); Mean maximum Euclidian distance in **e**: *vglut2a/2b* (410.8 ± 2.6 μm) > *glyt2* (289.6 ± 3.1 μm) > *gad1b* (218.2 ± 1.7 μm). Neurons with truncated SC-innervating axons were excluded.

f, Scatterplot showing the correlation between the number of branch points and the total branch length for the three neuronal populations. Correlation was assessed using the Pearson correlation and linear fitting ($r_{vglut2a/2b}$ = 0.80, r_{gad1b} = 0.65, r_{glyt2} = 0.85).

g, Cumulative distribution of the number of innervated regions. Pairwise comparison among the three neuronal populations was performed using Kolmogorov-Smirnov test, and *P* values are represented by color asterisks.

h,**i**, Volume rendering of the density maps of dendritic (**h**) and axonal (**i**) branches. Colors indicate point density within a 5 μm-radius sphere. The maximum number of calibration bars indicates the density value at which the heat map saturates.

j, Volume rendering of a single reconstructed *vglut2a* cranial relay neuron with the soma located in the R7[108], illustrating the definition of ipsilateral ("Ipsi")/contralateral ("Contra") and ascending ("Asc")/descending ("Desc") axons (light blue).

k, Proportions of neurons with Ipsi, Contra, or bilateral (Ipsi-Contra) axonal projections (left), or with Asc, Desc, or bidirectional (Asc-Desc) axonal projections (right).

l, Heatmap of mean projection strengths across four axonal trajectory quadrants. Asterisks represent comparison among the four quadrants (nonparametric Friedman test with Dunn's post hoc multiple comparisons.

m, Sagittal view of 10 commissural regions with midline-crossing points of contralateral and ipsilateral-contralateral projections.

n, Cumulative distributions of the number of crossings per neuron. Color asterisks represent corresponding inter-cell population comparison (Kolmogorov-Smirnov test).

o, Distribution of the mean number of crossings through different commissures at single cell level. Asterisks indicate inter-commissure difference within each cell population (shown beside of the name of neuron types) and inter-cell-population differences within each commissure (shown above bars) (Two-way ANOVA with Tukey's post hoc multiple comparison test).

Scale bars: 100 μm (**a**,**h-j**,**m**). The n represents the number of neurons examined. A, anterior; D, dorsal; V, ventral. Spatially adjacent commissures were treated as a single commissural region for quantification, including the hor and pop, and the cer and gus. ant, anterior commissure; cer&gus, cerebellar and secondary gustatory commissures; hab, habenular commissure; hor&pop, horizontal and postoptic commissures; inf, commissure infima of Haller; post, posterior commissure; tec, intertectal commissure; teg, ventral tegmental commissure; tub, posterior tuberculum commissure; ven, ventral rhombencephalic commissure. n.s., not significant; **P* < 0.05; ****P* < 0.001. See also Extended Data Fig. 4.

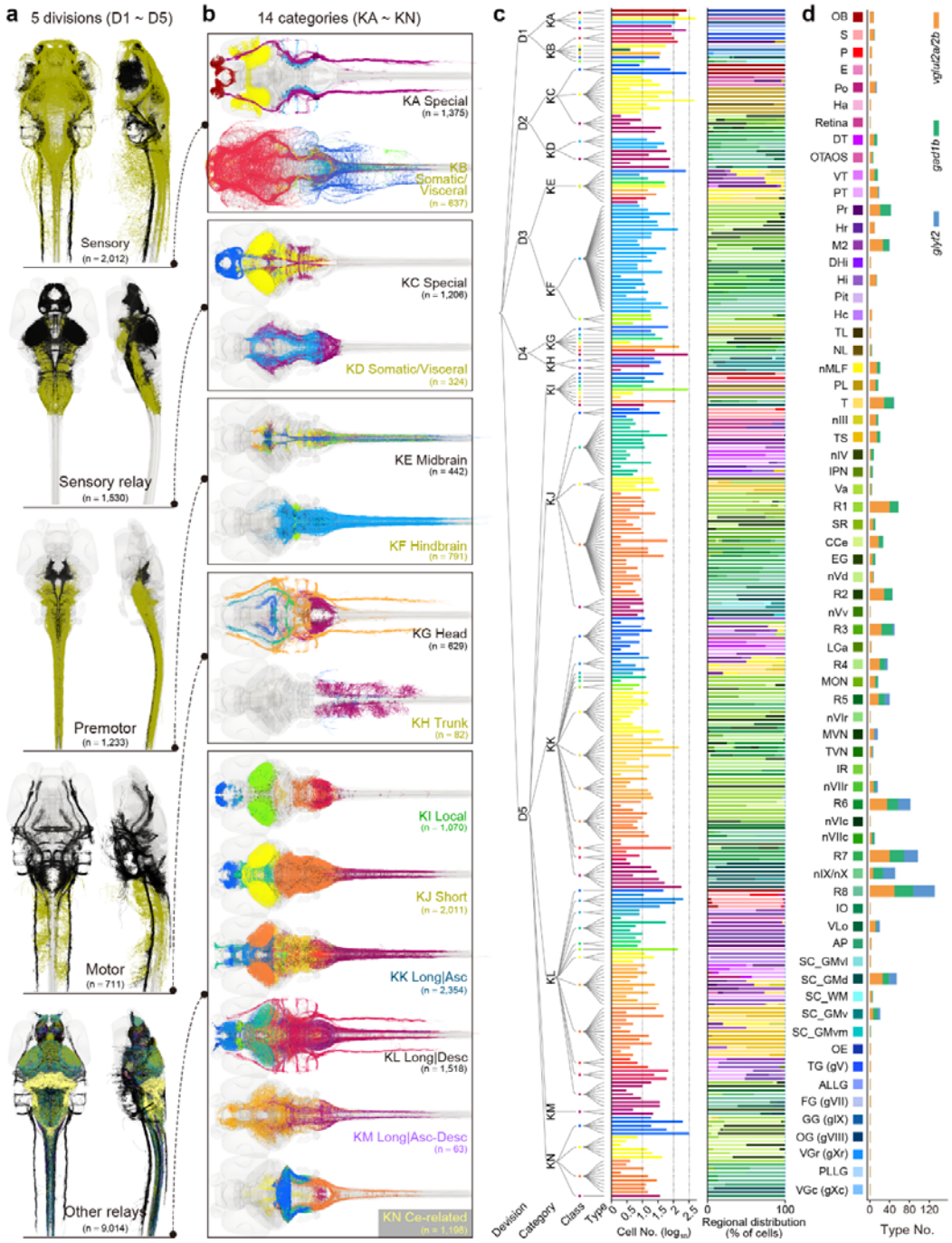

Fig. 5 | Hierarchical morphological classification of E and I neurons.

a,**b**, Volume rendering of all E and I morphotypes grouped into 5 divisions (**a**, dorsal and lateral views) and 14 categories (**b**, KA to KM, dorsal view). Neuronal tracing colors in **a** match the color of category names in **b**, and neuronal tracing colors in **b** match the color of class symbols in **c**. Cells in the midbrain category are color-coded by type, as their class and category are the same

c, Dendrogram of E neurons comprising 5 divisions, 14 categories, 71 classes, and 305 types, with bar plots showing cell number and regional distribution. The color codes for brain

regions are shown in **d**.

d, Bar plot showing the number of E and I morphotypes per region, ordered by the anteroposterior centroid within primary brain subdivisions, spinal cord, and peripheral ganglia.

The n represents the number of cells. See also Extended Data Figs. 5 and 6, and Supplementary Table 2.

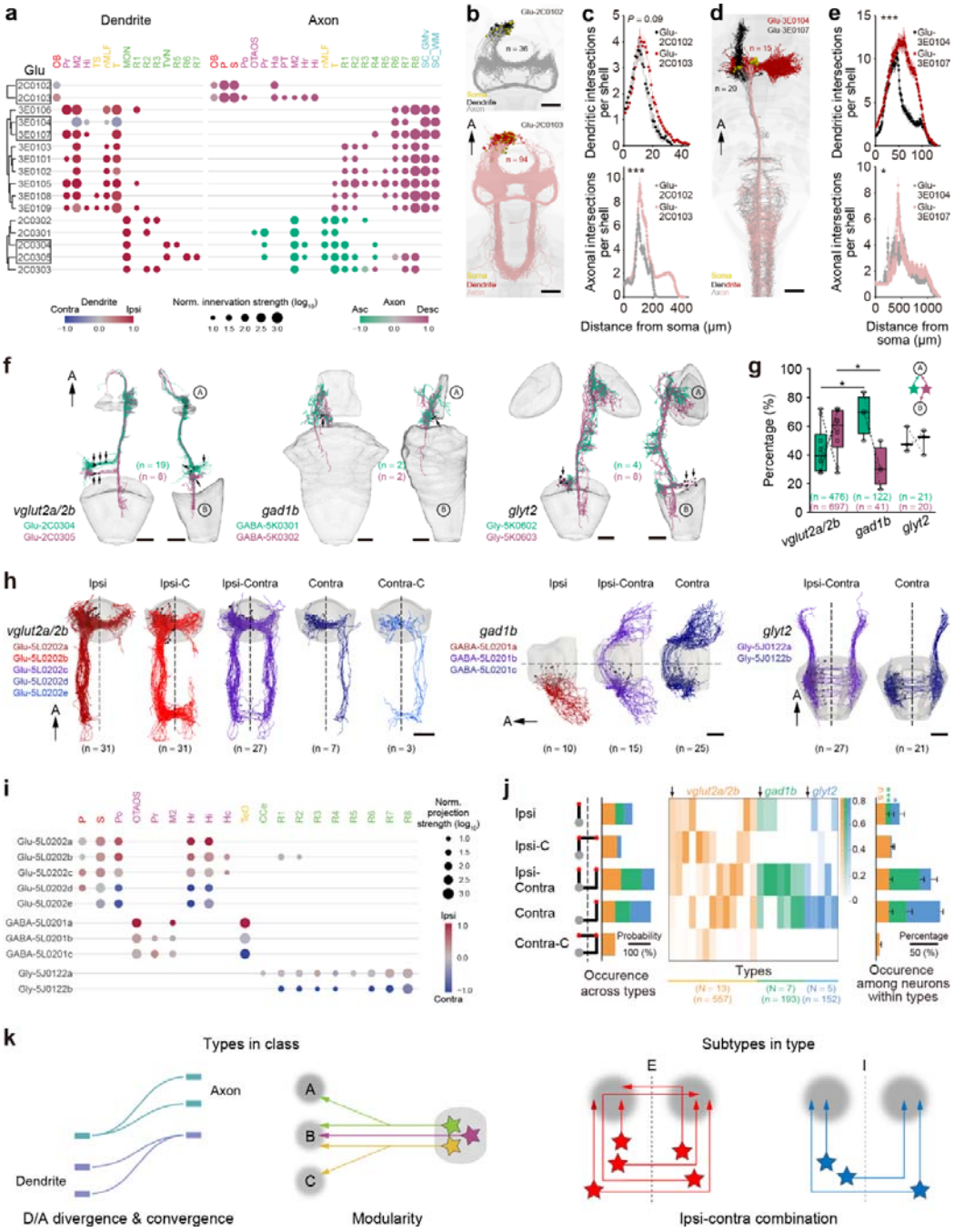

Fig. 6 | Projection design of E and I morphotypes.

a, Dot plot showing dendritic (left) and axonal (right) innervation strength (IS, dot size) and preference (dot color) for ipsilateral/contralateral (dendrite, $(IS_{ipsi}–IS_{contra})/(IS_{ipsi}+IS_{contra})$) or descending/ascending (axon, $(IS_{desc}–IS_{asc})/(IS_{desc}+IS_{asc})$) innervations of neuronal types from three classes across regions. Black boxes indicate example types shown in **b**,**d**,**f**.

b,**d**, Examples of two *vglut2a/2b* neuronal types within one class showing similar dendritic but different axonal innervations (**b**, mitral cells in the OB), or similar axonal but different dendritic innervations (**d**, MeL (black) *vs* MeM (red) neurons in nMLF[109]).

c,**e**, 3D Sholl analysis of dendrites (top) and axons (bottom) from types shown in **b**,**d**. The radius increment is 1 μm. Two tailed Mann-Whitney test was used.

f, Volume rendering of two types (seagreen and marron) within one class in each E and I neuronal population, featured by their common ascending projection pathways. Somata (arrows) in black. Ⓐ and Ⓑ represent two innervated regions.

g, Boxplot showing the proportion of cells with ascending-only (seagreen) *vs* ascending-descending (marron) projection types in each case across the three E and I neuronal populations. Inset: schematic illustrating two types sharing an ascending projection trajectory. The central mark, bottom, and top of the boxplot indicate the median, first, and third quartiles, respectively. Two-way ANOVA with Tukey's post hoc multiple comparison test was performed.

h, Examples showing ipsilateral/contralateral projection subtypes within one type with targeted bilateral projections in *vglut2a/2b* (left), *gad1b* (middle), and *glyt2* (right) neurons. Dendrites in darker color. Midline indicated by a dotted line.

i, Dot plot showing projection strength (PS, dot size) and preference (dot dolor) for ipsilateral/contralateral projections ($(PS_{ipsi}–PS_{contra})/(PS_{ipsi}+PS_{contra})$) of subtypes in **h**.

j, Heatmap (middle) of cell proportions of five ipsilateral/contralateral projection modes (subtypes) in each type (column, N = type count) from E and I neuron populations, and summary of mode occurrence probability across types (left) and among individual neurons within types (right). Arrows indicate the examples shown in **h**. Asterisks represent intra-neuronal population comparisons (nonparametric Friedman test with Dunn's post hoc multiple comparisons).

k, Schematic illustrating the rationale behind hierarchical classification from class to type (left, middle) and from type to subtype (right), and the associated projection design rules. A, B, and C denote targeted regions.

Scale bars: 50 μm (**b**,**d**,**f**,**h**). Regions in **a**,**i** are ordered by their centroid positions along the anteroposterior axis within high-level region divisions indicated by different colors. IDs of corresponding morphotypes are shown. Numbers in parentheses indicate the number of neurons shown or examined. A, anterior. Ipsi, ipsilateral; Ipsi-C, ipsilateral-collateral; Ipsi-Contra, ipsilateral-contralateral; Contra, contralateral; Contra-C, contralateral-collateral. n.s., not significant; $*P < 0.05$; $***P < 0.001$. See also Extended Data Figs. 7 and 8, and Supplementary Table 2.

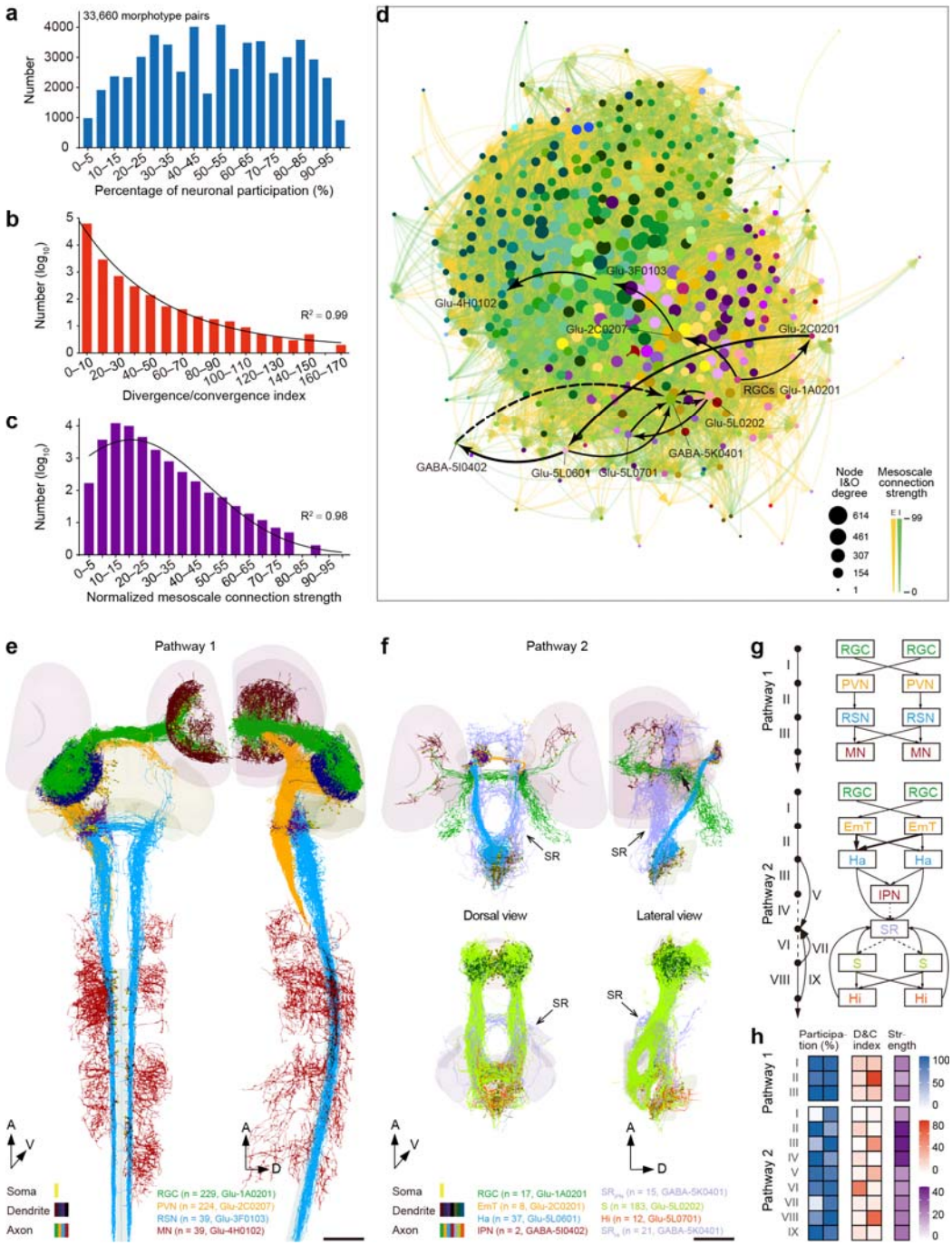

Fig. 7 | Directed and weighted inter-cell-type connectome supporting neural circuit mining.

a–**c**, Distributions of the percentage of neuronal participation (**a**), divergence/convergence index (**b**), and normalized mesoscale connection strength (**c**), which are calculated based on 33,660 connected morphotype pairs within 502 morphotypes (see Extended Data Fig. 9). For each connected morphotype pair, two values were calculated from the input and output morphotypes for the metrics in (**a**) and (**b**). Distributions of (**b**) and (**c**) were fitted respectively with a one-phase decay (R^2 = 0.99) and Gaussian (R^2 = 0.98), and plotted with the *y*-axis in log scale.

d, Graph visualization of the inter-cell-type E and I network with 502 nodes and 33,660 edges. Node size represents the total degree (total number of input and output connections), and node color indicates its primary distributed region, following the coloring scheme shown in Fig. 5d. The thickness of edges with arrows represents normalized directed connection strength, color-coded by E (orange) or I (green) attribute. Black edges highlight two visual pathways shown in **e**,**f**.

e,**f**, 3D visualization of two visual pathways starting from RGCs, rendered by morphologies of participating E and I morphotypes. Dendrites and axons (DA) are color-coded differently, and only connected neurons are shown, with distributed regions serving as the background. In **e**, only the right retina-involved pathway is shown. In **f**, the pathway is split into two parts (top and bottom), linked via a morphotype in the superior raphe (SR, open arrow). Black arrow (**f**) points to the arborization fields 3 and 4 (AF3 and AF4). Involved morphotypes with their cell numbers and IDs are annotated at the bottom.

g, Wiring diagrams of the two pathways in **e**,**f**, with each morphotype node named by attributed neuronal class or distributed brain region. The two hemisphere layout displays ipsilateral, contralateral, or bilateral projections. The coloring scheme matches the axon colors shown in **e**,**f**, and solid and dashed edges indicate E and I connections, respectively. Notably, EmT-to-Ha connections show left-side preference.

h, Connection metrics for the two pathways in **e**,**f**, including the percentage of neuronal participation ("Participation (%)") for input (left) and output (right) types, divergence/convergence index ("D&C index") for input (left) and output (right) types, and normalized connection strength ("Strength") between input and output types.

Scale bars: 50 μm (**e**,**f**). A, anterior; D, dorsal; V, ventral. EmT, eminentia thalami; Ha, habenula; Hi, intermediate hypothalamus; IPN, interpeduncular nucleus; MN, motor neuron; PVN, periventricular neuron; RGC, retinal ganglion cell; RSN, reticulospinal neuron; S, subpallium; SR, superior raphe. See also Extended Data Fig. 9, and Supplementary Videos 6 and 7.

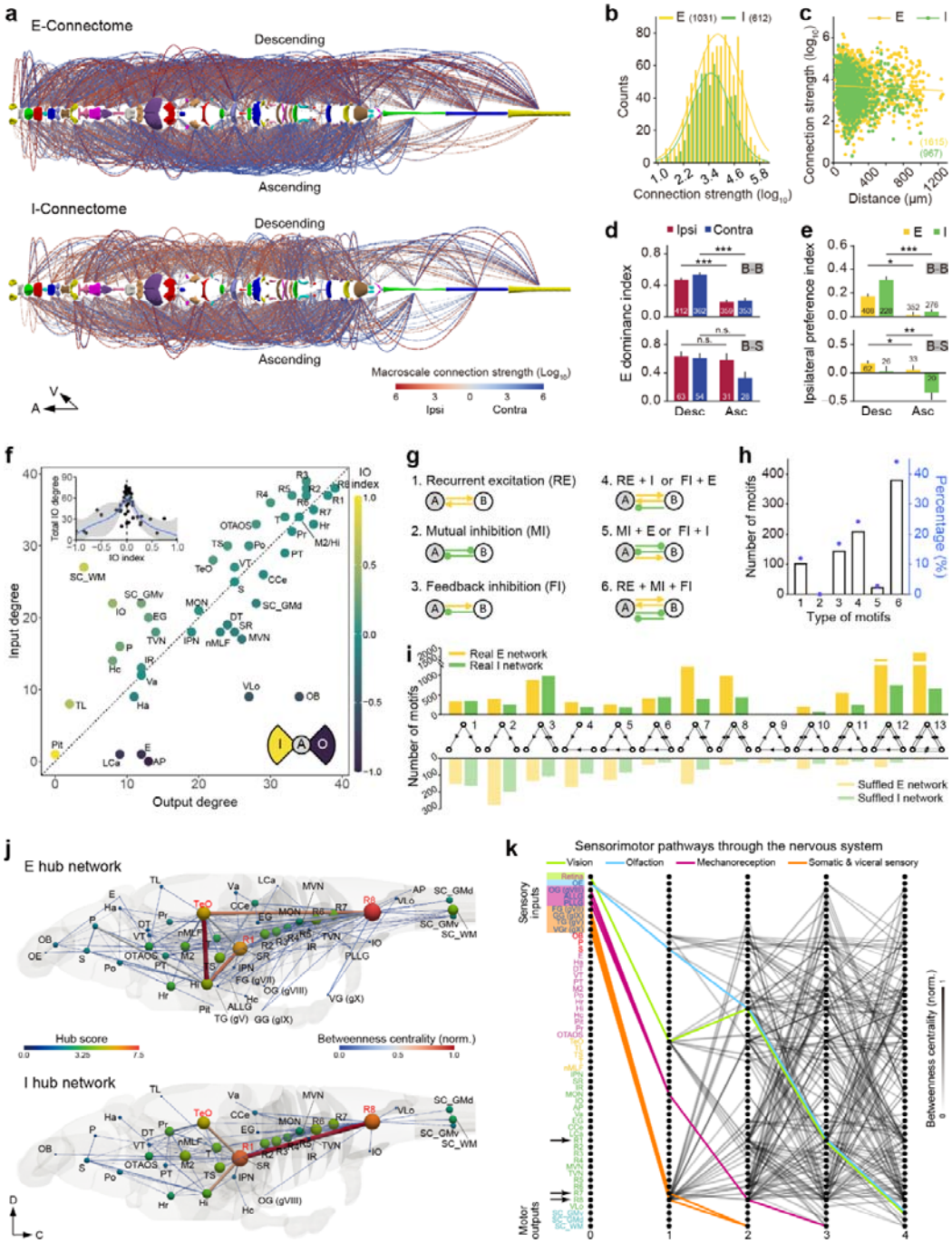

Fig. 8 | E and I neuron-based interregional connectome supporting network motif, hub, and information flow analyses.

a, Wiring diagram across 53 anatomical regions, based on the morphology and cytoarchitecture of E or I neurons (see Methods). Parabolas represent directed ipsilateral (red) and contralateral (blue) connection between regions, which are arranged linearly based on their anteroposterior centroid coordinates. Upper parabolas indicate descending connections, while lower parabolas indicate ascending connections. The parabola's height and color tone both represent macroscale connection strength (CS).

b, Histogram showing distribution of log-scaled interregional connection strength for E

(yellow) or I (green) neurons, each fitted by a Gaussian curve (solid lines; E neurons: R^2 = 0.91; I neurons: R^2 = 0.89).

c, Correlation between interregional distance and directed connection strength. E neurons: r = –0.05, P = 0.04; I neurons: r = –0.13, P < 0.001.

d, Summary of E dominance index, calculated as $(CS_E–CS_I)/(CS_E+CS_I)$, in ipsilateral (red) or contralateral (blue) descending and ascending interregional connections. B-B, inter-brain regions; B-S, mutual brain-spinal cord.

e, Summary of ipsilateral preference index, calculated as $(CS_{Ipsi}–CS_{Contra})/(CS_{Ipsi}+CS_{Contra})$, in E (yellow) or I (green) descending and ascending interregional connections.

f, Relationship between the input (I) degree and output (O) degree for 45 brain and SC regions (excluding the ganglia and retina). The IO index, calculated as $(D_I–D_O)/(D_I+D_O)$, is color coded. Positive IO index indicates input dominance (receiver), and negative one indicates output dominance (sender). Inset: scatterplot of IO index *vs* total IO degree, fitted by a Gaussian distribution (R^2 = 0.77).

g, Schematic of six two-node motifs with ≥2 directed connections with E and I identities. Yellow, E connection; Green, I connection.

h, Numbers (bar) and percentages (dot) of the two-node motifs in **g** in the interregional network.

i, Counts of 13 three-node motifs in the E (yellow) or I (green) interregional networks (top) and corresponding shuffled networks with the same IO degree distribution (bottom). Motif distributions in real networks significantly differ from shuffled networks, with expected counts derived from the average of 1,000 shuffles and scaled to the total motif count of the real network. Real *vs* shuffled E: X^2 = 15,564, P < 0.001; Real *vs* shuffled I: X^2 = 11,479, P < 0.001.

j, Constructed E and I hub networks. Each node (sphere) represents one of 53 regions (retina excluded), with its color and size indicating its hub score. R8, R1, and TeO are the top three hub regions for both E and I hub network. The color-coded edge width (normalized betweenness centrality) reflects its importance in the information flow among regions.

k, Flat connectivity map (based on the E hub network in **j**) showing sensorimotor pathways from the retina and peripheral sensory ganglia to the SC within 4 steps. The shortest pathway from the starter sensory region to the SC is highlighted with colors. The retina-to-TeO connection is knowledge-based. Arrows point to the premotor hubs R1, R7, or R8.

A, anterior; C, caudal; D, dorsal; V, ventral. Numbers in parentheses (**b**,**c**) or on bars (**d**,**e**) represent the number of source-target pairs. n.s., not significant; *P < 0.05; **P < 0.01; ***P < 0.001 (nonparametric Kruskal-Wallis test with Dunn's post hoc multiple comparisons in **d**,**e**). See also Extended Data Figs. 10 and 11, and Supplementary Video 8.

Extended Data Figures and Legends

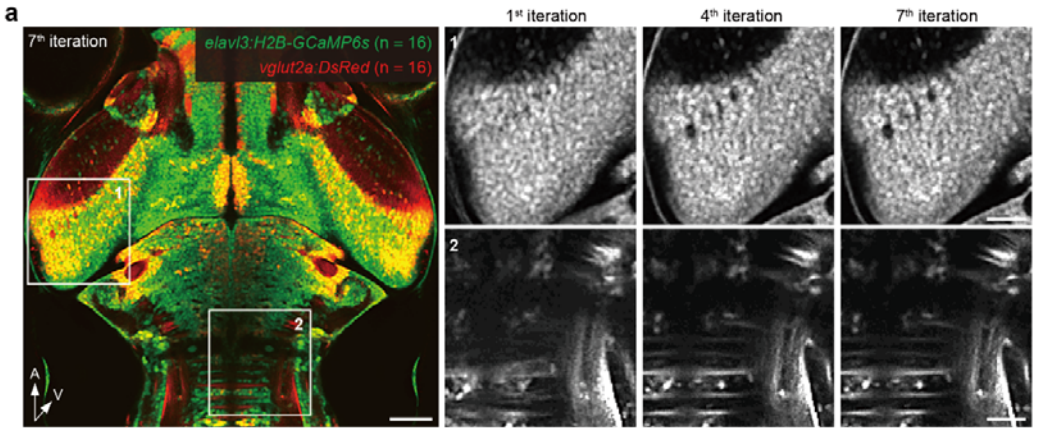

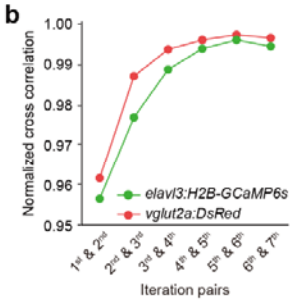

c

Bimodal transgenic line	Fish No.	Iteration times	Bridging line
elavl3:H2B-GCaMP6s;vglut2a:DsRed	16	7	-
*vglut2a:DsRed;**vglut2b:GAL4FF**;UAS:GFP*	6	6	*vglut2a:DsRed*
***gad1b:EGFP**;vglut2a:DsRed*	11	9	*vglut2a:DsRed*
***gad1b:GAL4-VP16**;UAS:GFP*	17	12	*gad1b:EGFP*
***glyt2:GFP**;vglut2a:DsRed*	10	11	*vglut2a:DsRed*
*vglut2a:DsRed;**vmat2:GFP***	9	8	*vglut2a:DsRed*
*elavl3:H2B-GCaMP6s;**elavl3:NEXS-jRGECO1a***	11	11	*elavl3:H2B-GCaMP6s*

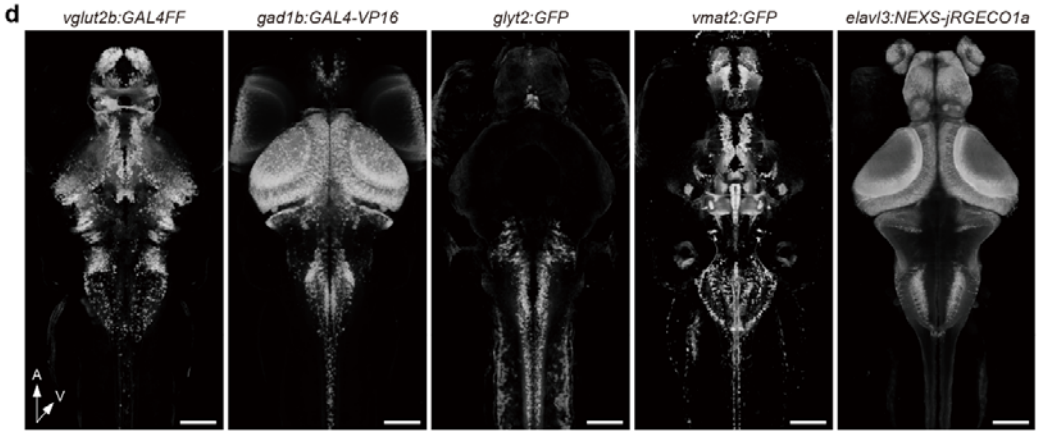

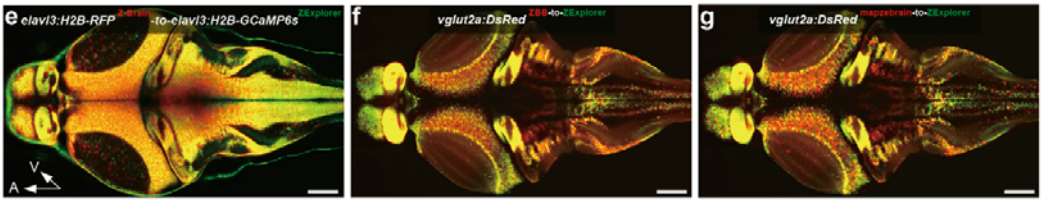

h

#	Landmarks	Coordinates
	elavl3:H2B-GCaMP6s ZExplorer/mapzebrain *elavl3:H2B-RFP* Z-Brain	
1	Joint point of cell stripe immediately medial to ventral eminentia granularis [R]	453, 583, 163
2	Dorsal exit point of tract from cerebellum [L]	211, 581, 141
3	Mid-point of ventral medial extent of tectum	327, 494, 92
4	Joint point of cell clusters in caudal most medulla [R]	342, 900, 63
5	Midline joint point of cell clusters in subpallium	322, 218, 167
6	Anterior joint point of nIV ventral cell clusters [R]	357, 505, 145
7	Joint point of cell clusters in lateral corpus cerebelli and R2 [L]	179, 612, 87
8	Mauthner cell nucleus in R4 [L]	281, 648, 130
9	Midline joint point of cell clusters in anterior torus longitudinalis	326, 313, 74
	elavl3:NES-jRGECO1a ZExplorer *elavl3:GCaMP5G* Z-Brain/mapzebrain *elavl3:CaMPARI* ZBB	
1	Middle of anterior commissure	325, 219, 179
2	Middle of habenular commissure	324, 288, 83
3	Middle of ansulate commissure	329, 504, 222
4	Middle of commissure below AP in caudal most medulla	326, 902, 58
5	Entry point of optic nerve to tectal neuropil [R]	471, 383, 160
6	Dorsal medial point of griseum tectale	241, 330, 81
7	Entry point of projections from corpus cerebelli to MON [L]	202, 595, 123
8	Midline tip of ventral most cell bands at R2/R3	327, 603, 172
9	Bifurcation point of the lateral tract in M2	225, 426, 163
	vglut2a:DsRed ZExplorer/ZBB/mapzebrain *vglut2a:GFP* Z-Brain	
1	Middle of left nerve from olfactory epithelium to brain [L]	259, 111, 197
2	Middle of anterior commissure	322, 221, 178
3	Medial joint point of cell clusters surrounding griseum tectale [R]	434, 342, 110
4	Dorsal exit point of nerve from torus semicircularis [L]	190, 519, 178
5	Mid-point of projections to caudal hypothalamus	325, 596, 239
6	Middle of R5 commissure	325, 691, 131
7	Ventral-most cluster of cells in medial/caudal medulla	328, 796, 170
8	Anterior-most midline cell in ventral/caudal medulla	327, 888, 119
9	Ventral-most boundary of valvula cerebelli/corpus cerebelli gray matter [L]	278, 566, 45
	gad1b:GFP ZExplorer/ZBB	
1	Middle of tract lateral to preoptic area [R]	374, 290, 178
2	Lateral extent of ventral thalamus [R]	414, 295, 111
3	Ventral projection from Hi [R]	413, 560, 255
4	Lateral extent of R1 dorsal cell cluster [L]	204, 532, 129
5	Medial cell cluster in R6 [R]	361, 696, 132
6	Middle of posterior commissure	326, 370, 105
	glyt2:GFP ZExplorer/ZBB	
1	Dorsal exit point of nerve from torus semicircularis [R]	452, 509, 176
2	Base of commissure in R4 [L]	254, 642, 124
3	Lateral extent cell cluster in R5 [L]	205, 705, 87
4	Caudal/medial cell cluster in R6 [L]	279, 719, 101
5	Ventral-most boundary of pallium/habenula gray matter [R]	401, 275, 113
6	Middle of R4 commissure	326, 638, 142
	vmat2:GFP ZExplorer/ZBB	
1	Dorsal/caudal midline tip of cell bands in pretectum	326, 396, 112
2	Lateral cell cluster in Hi [R]	447, 451, 219
3	Rostral midline of dorsal raphe	325, 503, 144
4	Locus coeruleus, middle of cell cluster [L]	257, 557, 151
5	Exit point of dorso-caudal tract from Hc [R]	374, 577, 248
6	Inferior raphe, large cell cluster, caudal MO	326, 737, 142

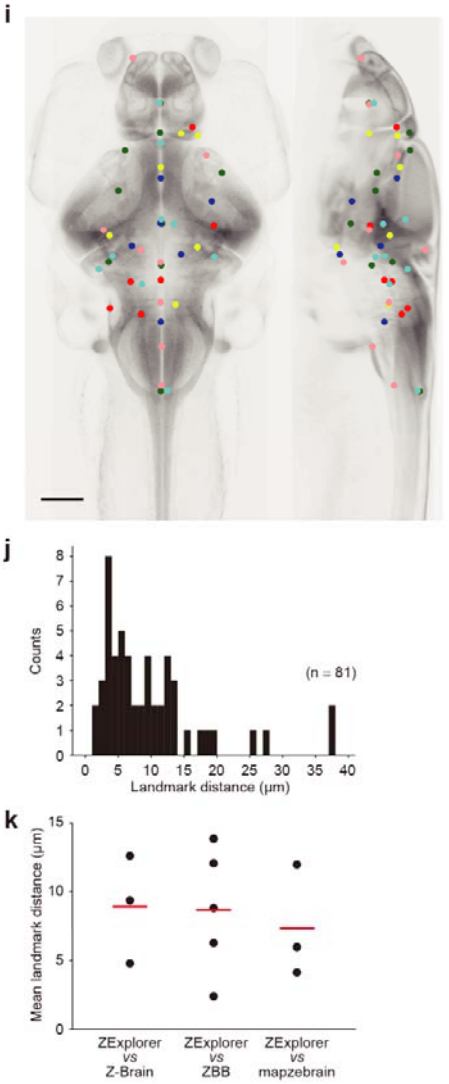

Extended Data Fig. 1 | Template creation and inter-atlas registration accuracy evaluation. a, Iterative template refinement. Two cropped areas (1,2) from a horizontal section (left) show increased anatomical clarity in the average images (right) with iteration. Area 1: *elavl3:H2B-GCaMP6s* pattern around region boundaries; Area 2: *vglut2a:DsRed* pattern in neuronal fiber-enriched regions.

b, Improved similarity measured by normalized cross correlation (NCC) between successive iterations, showing convergence to a stable average template.

c, Summary of lines, fish numbers, iteration counts, and bridging lines for generating the original dual-channel template (*elavl3:H2B-GCaMP6s;vglut2a:DsRed*) and six additional reference templates (in bold).

d, Volume rendering (dorsal view) of five additional reference templates in the CPS. Partial spinal cord shown.

e–**g**, Horizontal sections showing merged images of our bridge template (ZExplorer, green) and the registered counterpart from another atlas (red). The notation above each image indicates the name of the bridge template and its source atlas (as superscripts). The "to" denotes the registration direction between two atlases. Specifically, Z-Brain (**e**) was registered via the *elavl3:H2B-RFP* template to our ZExplorer *elavl3:H2B-GCaMP6*s template, ZBB (**f**) and mapzebrain (**g**) were registered via the *vglut2a:DsRed* template to our corresponding *vglut2a:DsRed* template.

h, Point-based landmarks identified in the template counterparts across ZExplorer and three other atlases. A total of six expression patterns were used, comprising 11 pairs of comparisons, with each pattern indicated by a distinct background colors. The name of each template counterpart for each expression pattern is shown, with its source atlas indicated as a superscript. Coordinates are reported in our CPS reference frame.

i, Landmark positions for each template (**h**) overlaid on the horizontal (left) and sagittal (right) maximum projections of *elavl3:H2B-GCaMP6s*. Coloring scheme follows that in **h**.

j, Distribution of landmark distances (LDs) across 81 inter-atlas landmark pairs (24 from 3 expression patterns for Z-Brain *vs* ZExplorer; 34 from 5 expression patterns for ZBB *vs* ZExplorer; 23 from 3 expression patterns for mapzebrain *vs* ZExplorer).

k, Mean landmark distance (MLD) for 11 pairs of comparisons used in evaluating inter-atlas registration precision. ZExplorer *vs* Z-brain and mapzebrain: *elavl3:H2B-FPs*, *elavl3:GECIs*, and *vglut2a:DsRed*; ZExplorer *vs* ZBB: *elavl3:GECIs*, *vglut2a:DsRed*, *gad1b:GFP*, *glyt2:GFP*, and *vmat2:GFP*. Red lines indicate the mean MLDs.

Scale bars: 50 μm (**a**, left), 20 μm (**a**, right), 100 μm (**d-g**,**i**). A, anterior; D, dorsal; V, ventral.

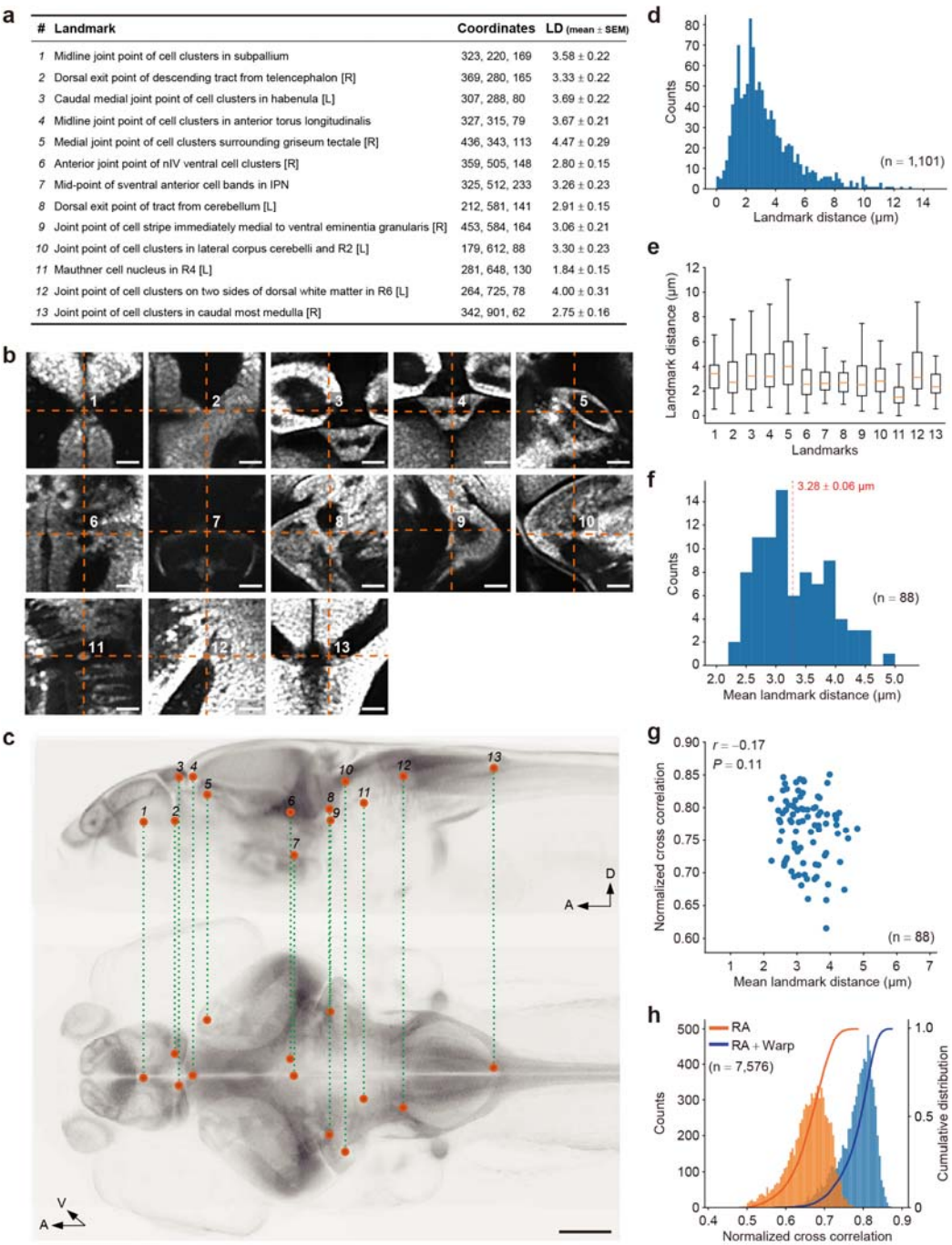

#	Landmark	Coordinates	LD (mean ± SEM)
1	Midline joint point of cell clusters in subpallium	323, 220, 169	3.58 ± 0.22
2	Dorsal exit point of descending tract from telencephalon [R]	369, 280, 165	3.33 ± 0.22
3	Caudal medial joint point of cell clusters in habenula [L]	307, 288, 80	3.69 ± 0.22
4	Midline joint point of cell clusters in anterior torus longitudinalis	327, 315, 79	3.67 ± 0.21
5	Medial joint point of cell clusters surrounding griseum tectale [R]	436, 343, 113	4.47 ± 0.29
6	Anterior joint point of nIV ventral cell clusters [R]	359, 505, 148	2.80 ± 0.15
7	Mid-point of sventral anterior cell bands in IPN	325, 512, 233	3.26 ± 0.23
8	Dorsal exit point of tract from cerebellum [L]	212, 581, 141	2.91 ± 0.15
9	Joint point of cell stripe immediately medial to ventral eminentia granularis [R]	453, 584, 164	3.06 ± 0.21
10	Joint point of cell clusters in lateral corpus cerebelli and R2 [L]	179, 612, 88	3.30 ± 0.23
11	Mauthner cell nucleus in R4 [L]	281, 648, 130	1.84 ± 0.15
12	Joint point of cell clusters on two sides of dorsal white matter in R6 [L]	264, 725, 78	4.00 ± 0.31
13	Joint point of cell clusters in caudal most medulla [R]	342, 901, 62	2.75 ± 0.16

Extended Data Fig. 2 | Evaluation of registration precision for the single E and I neuron atlas.

a, Thirteen point-based landmarks identified in the *elavl3:H2B-GCaMP6s* reference template for evaluating registration precision. Coordinates refer to positions on sagittal (*x*), transverse (*y*), and horizontal (*z*) planes in the CPS. LD (mean ± SEM) represents averaged registration precision for each landmark from 88 randomly selected individual fish.

b, Horizontal sections showing landmark positions (cross center) in the *elavl3:H2B-GCaMP6s* expression pattern.

c, Spatial distribution of the 13 landmarks overlaid on sagittal (top) and horizontal (bottom) maximum projections of the *elavl3:H2B-GCaMP6s* reference template.

d, Distribution of 1,101 LDs from 88 individual fish, with less than 13 landmarks detected in some fish.

e, Boxplot of LDs for each of the 13 landmarks, with 78–88 fish per landmark. The central mark, bottom, and top of the boxplot indicate the median, first, and third quartiles, respectively.

f, Distribution of MLDs across 88 fish. Red dashed line indicates the overall mean.

g, Scatterplot showing no correlation between MLD and normalized cross correlation (NCC) among 88 fish (Pearson correlation).

h, Histogram and cumulative distribution of NCC values from 7,576 *elavl3:H2B-GCAMP6s* fish scans following two-step RA (orange) and warp (blue) registration.

Scale bars: 20 μm (**b**), 100 μm (**c**). A, anterior; D, dorsal; V, ventral.

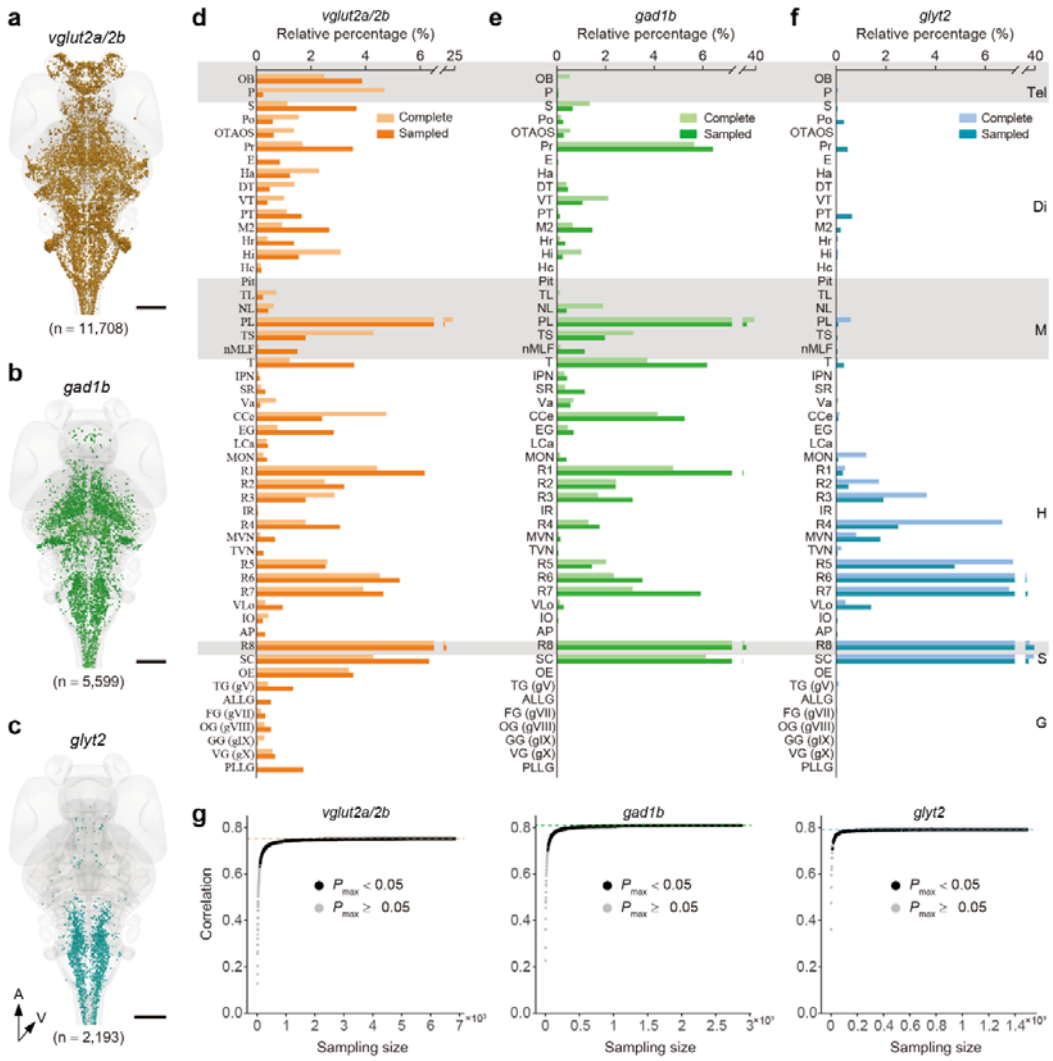

Extended Data Fig. 3 | Evaluation of neuron sampling randomness.

a–**c**, Volume rendering (dorsal view) of somata from reconstructed *vglut2a/2b* (**a**), *gad1b* (**b**), and *glyt2* (**c**) neurons in the CPS. Sphere size reflects measured soma diameter. Partial SC shown.

d–**f**, Bar plots comparing the regional distributions of complete (light color) and sampled (dark color) neurons across 52 anatomical regions (with subregions in the SC and vagal ganglia merged) for each E and I neuron populations.

g, Scatterplot showing the average Pearson correlation between the regional distributions of complete and randomly sampled neurons (sampled 1,000 times) from E and I neuron populations, with sampling size increasing from 1 cell to ~50% of the total by one-cell increment. Dotted line indicates the Pearson *r* at the maximum sampling size.

Scale bars: 100 μm (**a**–**c**). A, anterior; V, ventral.

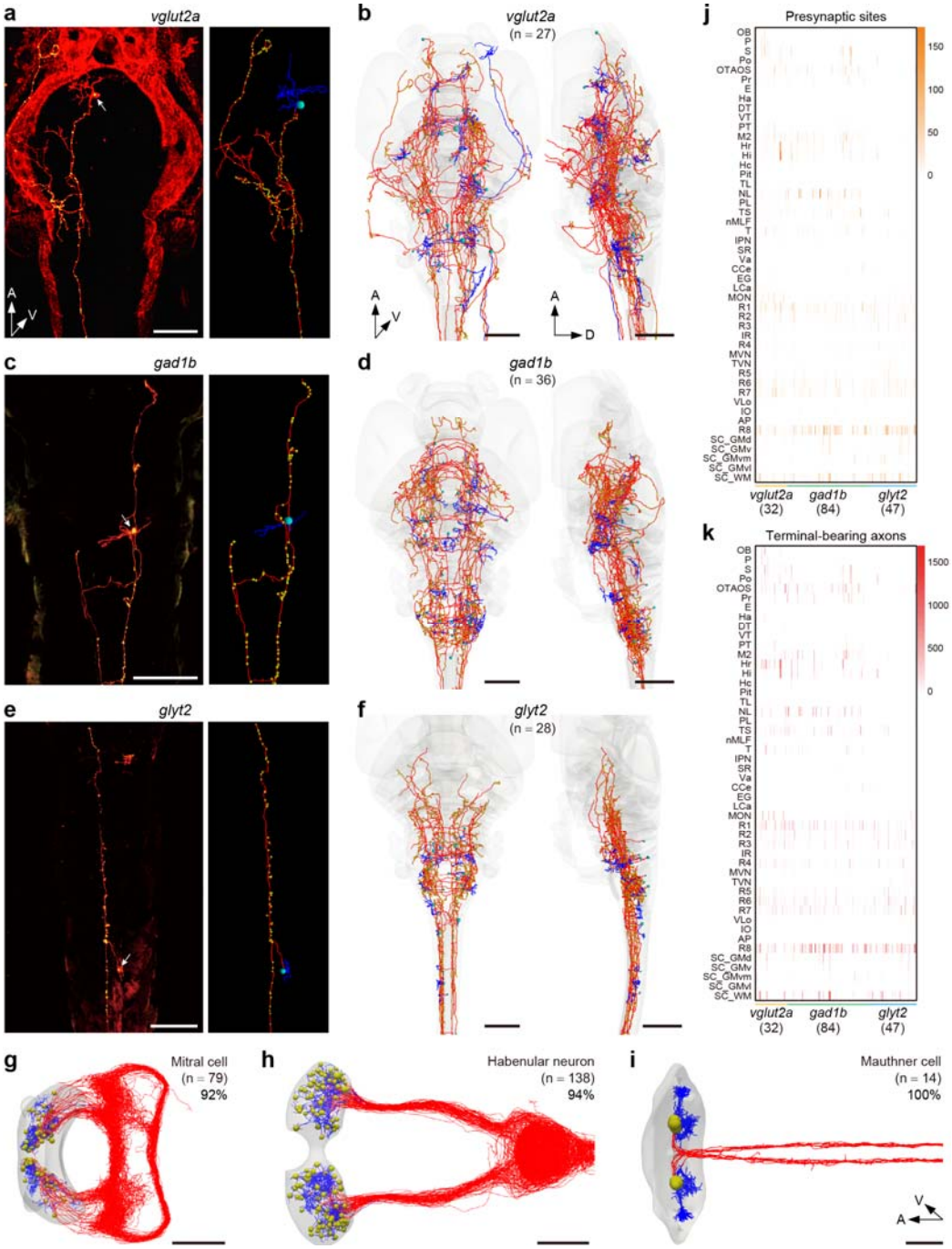

Extended Data Fig. 4 | Dendrite-axon identification and validation of projection strength metrics.

a,**c**,**e**, Volume rendering (dorsal view) of image stacks (left) with a single *vglut2a* (**a**), *gad1b* (**c**), or *glyt2* (**e**) neuron labeled by *Sypb-EGFP-tdKatushka2-CAAX* and corresponding reconstructions (right) showing soma (cyan), dendrites (blue), axons (red), and presynaptic puncta (yellow).

b,**d**,**f**, Dorsal (left) and lateral (right) 3D views of single-neuron reconstructions for *vglut2a* (**b**), *gad1b* (**d**), and *glyt2* (**f**) neurons labeled by *Sypb-EGFP-tdKatushka2-CAAX*, with

substructures color-coded s in **a**.

g–**i**, Machine learning-based dendrite-axon classification for three known cell types: mitral cells (**g**), habenular neurons (**h**), and Mauthner cells (**i**), with the classification accuracy indicated by the percentage. The background is the brain regions where the soma locates. Soma, yellow; dendrite, blue; axon, red.

j,**k**, Neuron-to-region projection matrices generated using two metrics: presynaptic site count (**j**) and terminal-bearing axon length (**k**). These two metrics display high similarity (Pearson $r = 0.78$, $P < 0.001$), analyzed by *corrcoef* function in MATLAB.

Scale bars: 100 μm (**a**–**f**), 50 μm (**g**–**i**). A, anterior; D, dorsal; V, ventral. The number in parentheses indicate the number of neuron examined.

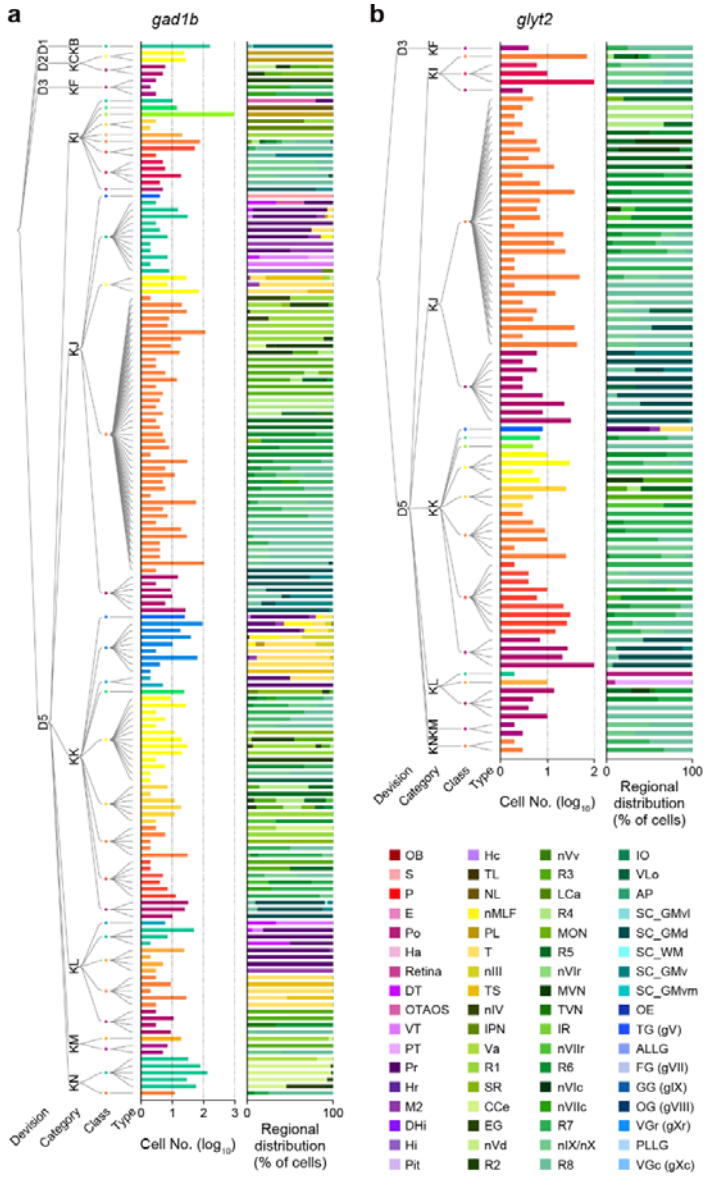

Extended Data Fig. 5 | Hierarchical morphological classification of I neurons.

a, Dendrogram of GABAergic (*gad1b*) inhibitory neurons comprising 4 divisions, 9 categories, 36 classes, and 155 types, with bar plots showing cell number and regional distribution.

b, Dendrogram of glycinergic (*glyt2*) inhibitory neurons comprising 2 divisions, 7 categories, 19 classes, and 84 types, with bar plots showing cell number and regional distribution.

Color schemes for brain regions are shown in the bottom right corner.

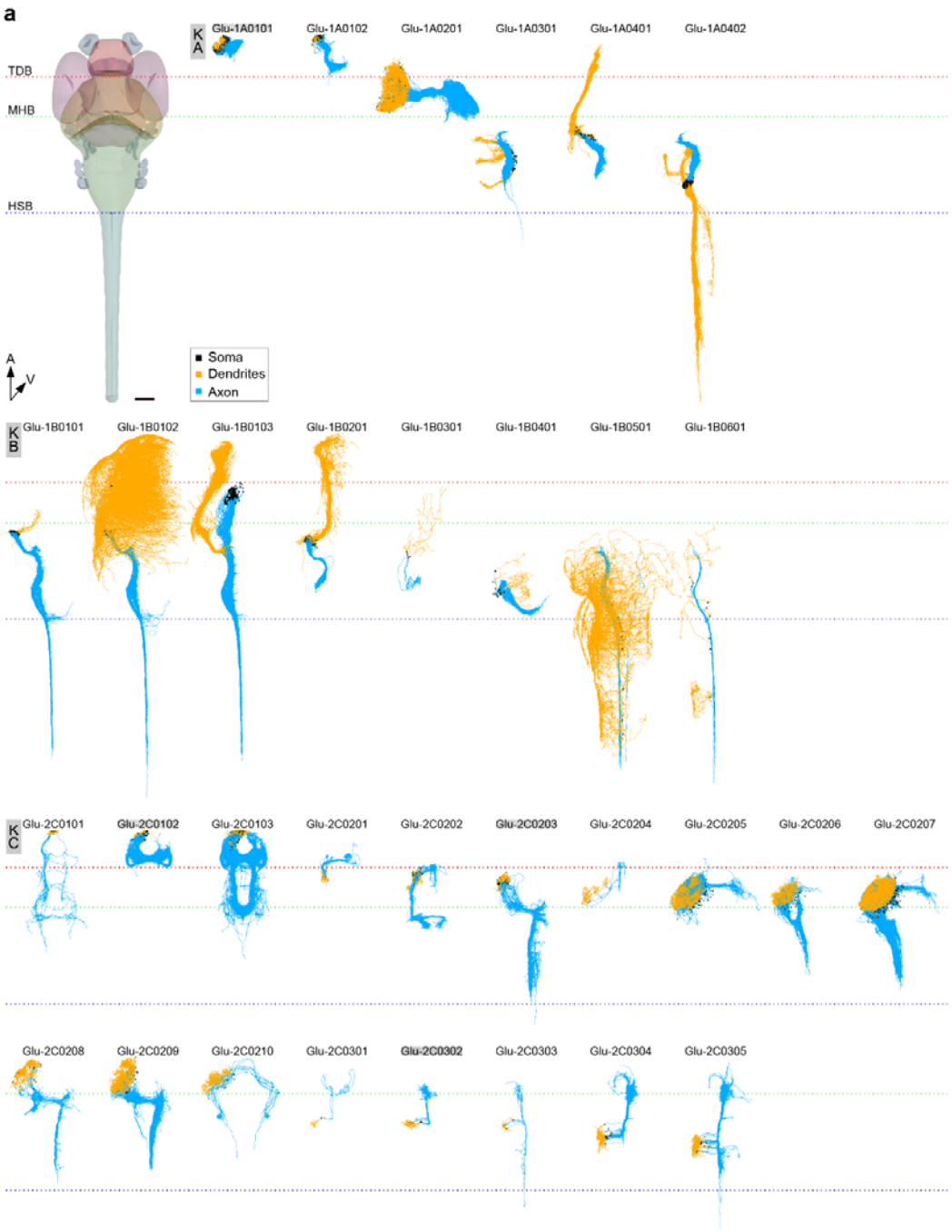
a
TDB
MHB
HSB
A
V
Soma
Dendrites
Axon
KA
Glu-1A0101
Glu-1A0102
Glu-1A0201
Glu-1A0301
Glu-1A0401
Glu-1A0402
KB
Glu-1B0101
Glu-1B0102
Glu-1B0103
Glu-1B0201
Glu-1B0301
Glu-1B0401
Glu-1B0501
Glu-1B0601
KC
Glu-2C0101
Glu-2C0102
Glu-2C0103
Glu-2C0201
Glu-2C0202
Glu-2C0203
Glu-2C0204
Glu-2C0205
Glu-2C0206
Glu-2C0207
Glu-2C0208
Glu-2C0209
Glu-2C0210
Glu-2C0301
Glu-2C0302
Glu-2C0303
Glu-2C0304
Glu-2C0305

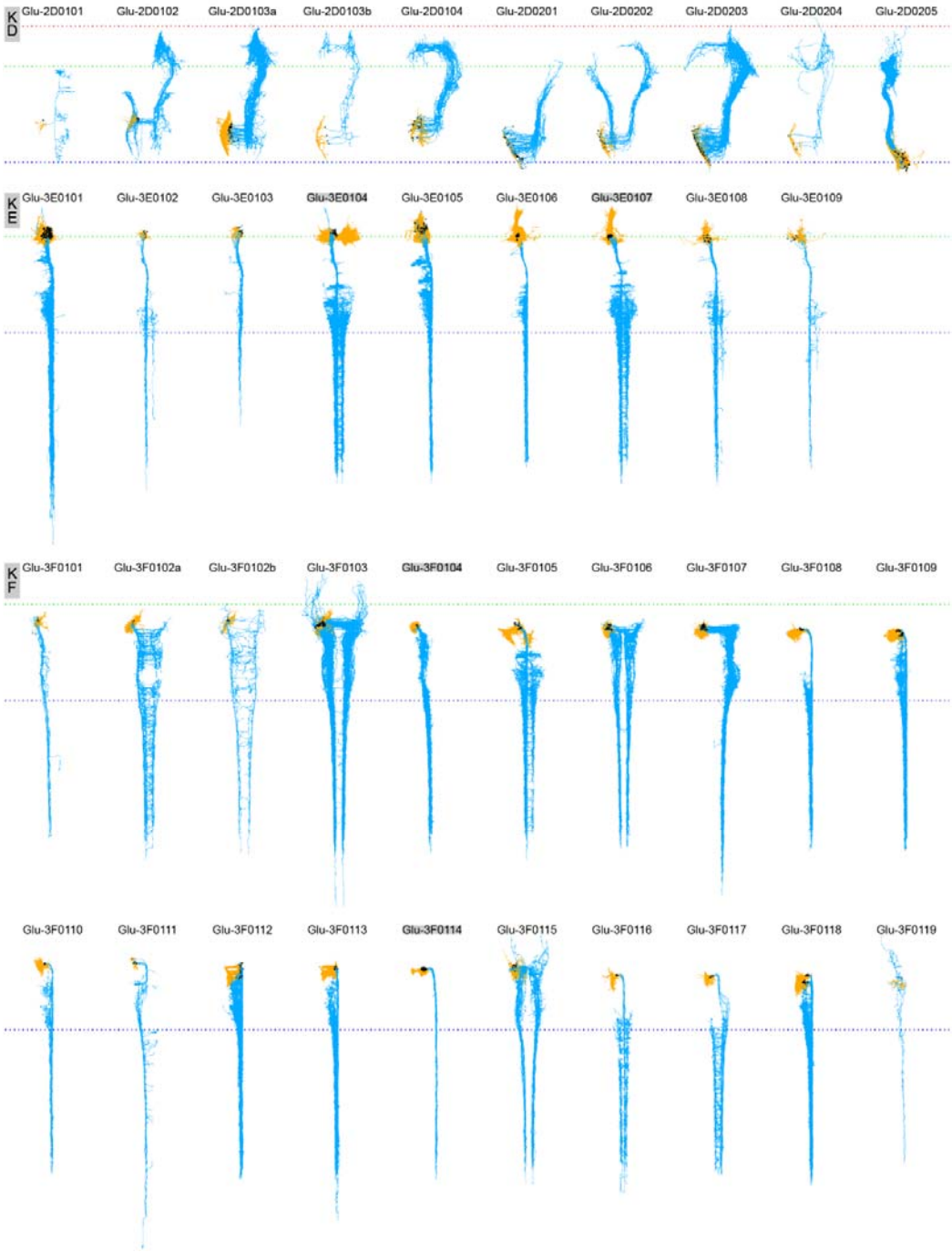
KD
Glu-2D0101
Glu-2D0102
Glu-2D0103a
Glu-2D0103b
Glu-2D0104
Glu-2D0201
Glu-2D0202
Glu-2D0203
Glu-2D0204
Glu-2D0205
KE
Glu-3E0101
Glu-3E0102
Glu-3E0103
Glu-3E0104
Glu-3E0105
Glu-3E0106
Glu-3E0107
Glu-3E0108
Glu-3E0109
KF
Glu-3F0101
Glu-3F0102a
Glu-3F0102b
Glu-3F0103
Glu-3F0104
Glu-3F0105
Glu-3F0106
Glu-3F0107
Glu-3F0108
Glu-3F0109
Glu-3F0110
Glu-3F0111
Glu-3F0112
Glu-3F0113
Glu-3F0114
Glu-3F0115
Glu-3F0116
Glu-3F0117
Glu-3F0118
Glu-3F0119

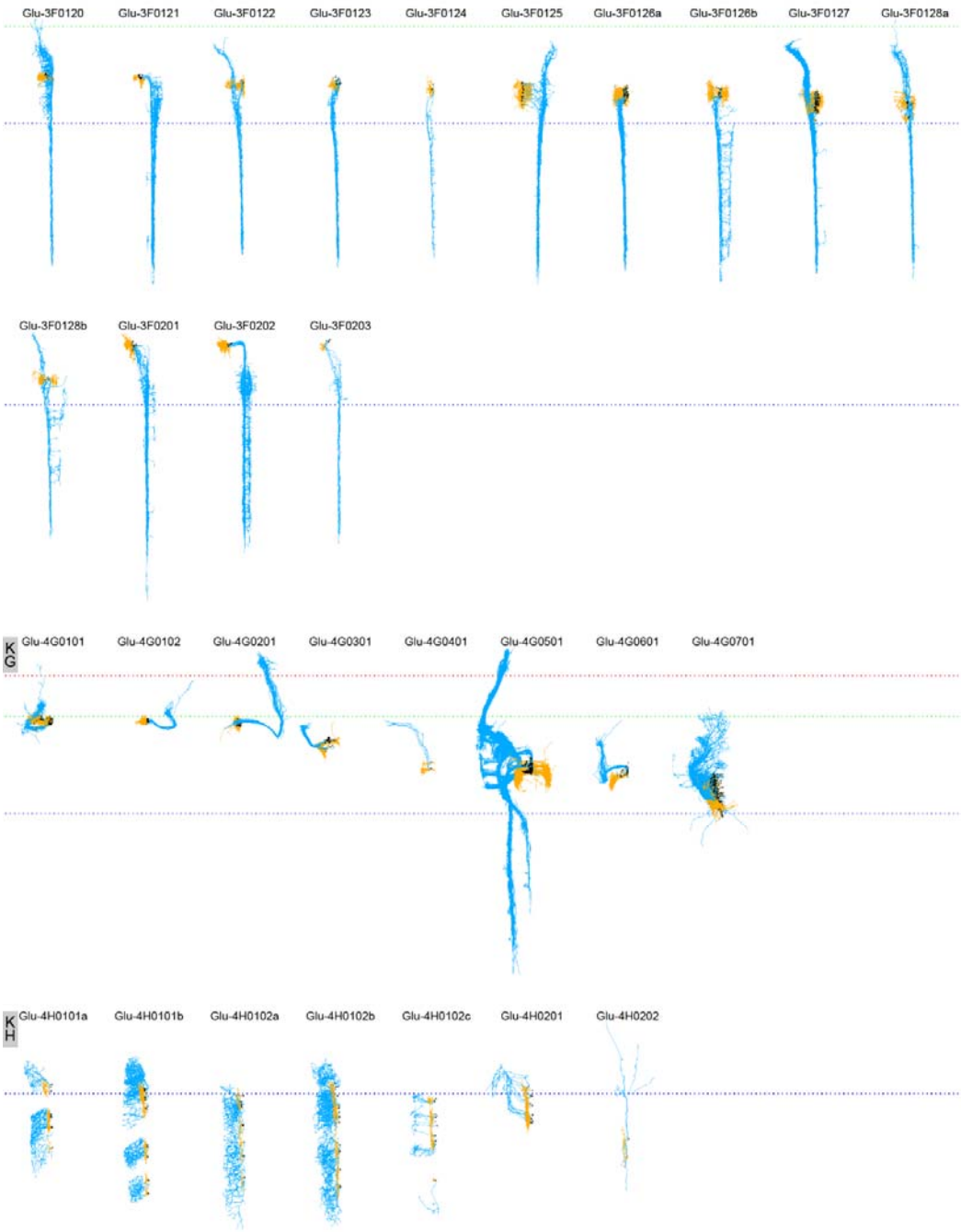
Glu-3F0120
Glu-3F0121
Glu-3F0122
Glu-3F0123
Glu-3F0124
Glu-3F0125
Glu-3F0126a
Glu-3F0126b
Glu-3F0127
Glu-3F0128a
Glu-3F0128b
Glu-3F0201
Glu-3F0202
Glu-3F0203
KG
Glu-4G0101
Glu-4G0102
Glu-4G0201
Glu-4G0301
Glu-4G0401
Glu-4G0501
Glu-4G0601
Glu-4G0701
KH
Glu-4H0101a
Glu-4H0101b
Glu-4H0102a
Glu-4H0102b
Glu-4H0102c
Glu-4H0201
Glu-4H0202

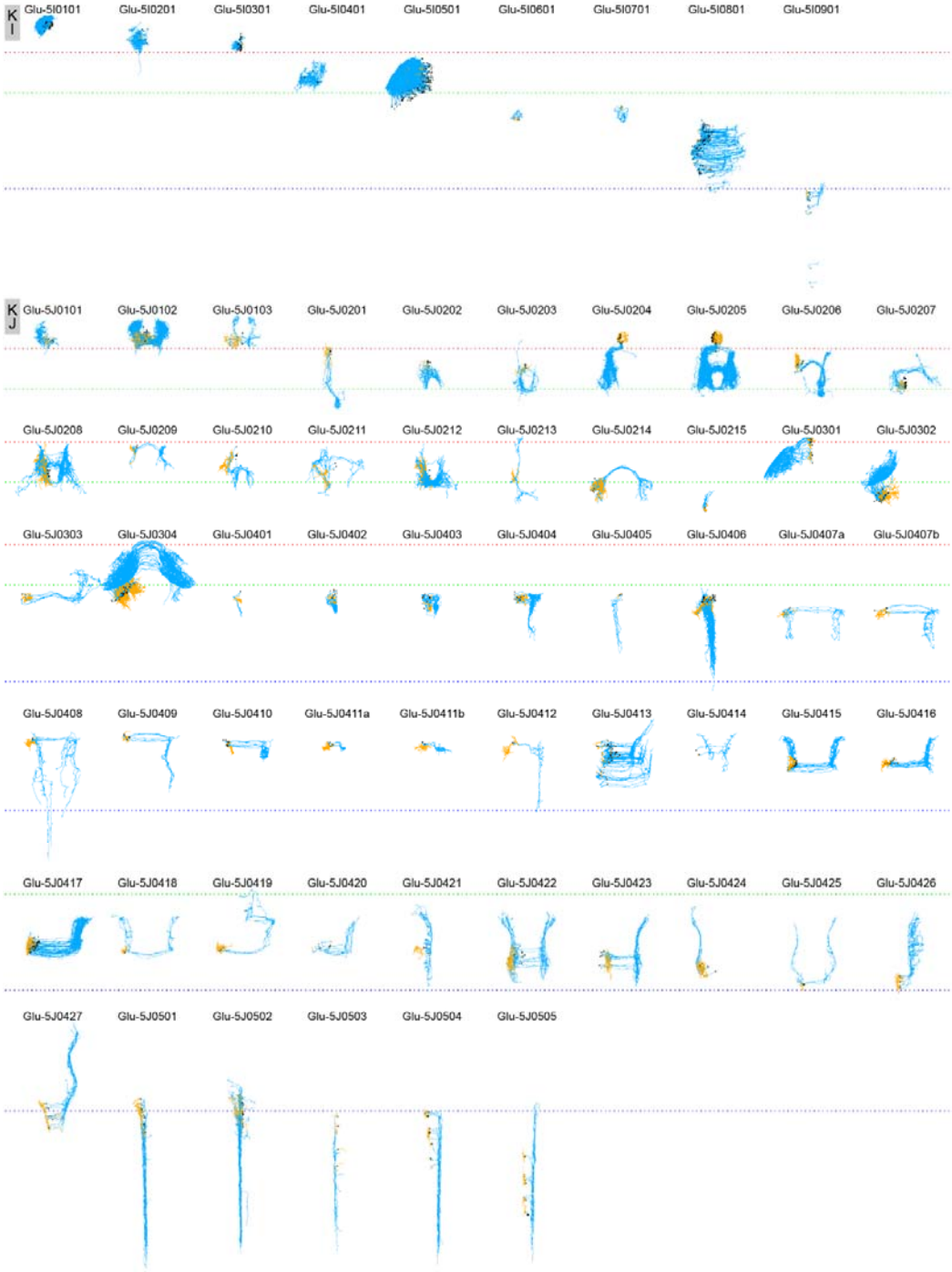
K I
Glu-5I0101
Glu-5I0201
Glu-5I0301
Glu-5I0401
Glu-5I0501
Glu-5I0601
Glu-5I0701
Glu-5I0801
Glu-5I0901
K J
Glu-5J0101
Glu-5J0102
Glu-5J0103
Glu-5J0201
Glu-5J0202
Glu-5J0203
Glu-5J0204
Glu-5J0205
Glu-5J0206
Glu-5J0207
Glu-5J0208
Glu-5J0209
Glu-5J0210
Glu-5J0211
Glu-5J0212
Glu-5J0213
Glu-5J0214
Glu-5J0215
Glu-5J0301
Glu-5J0302
Glu-5J0303
Glu-5J0304
Glu-5J0401
Glu-5J0402
Glu-5J0403
Glu-5J0404
Glu-5J0405
Glu-5J0406
Glu-5J0407a
Glu-5J0407b
Glu-5J0408
Glu-5J0409
Glu-5J0410
Glu-5J0411a
Glu-5J0411b
Glu-5J0412
Glu-5J0413
Glu-5J0414
Glu-5J0415
Glu-5J0416
Glu-5J0417
Glu-5J0418
Glu-5J0419
Glu-5J0420
Glu-5J0421
Glu-5J0422
Glu-5J0423
Glu-5J0424
Glu-5J0425
Glu-5J0426
Glu-5J0427
Glu-5J0501
Glu-5J0502
Glu-5J0503
Glu-5J0504
Glu-5J0505

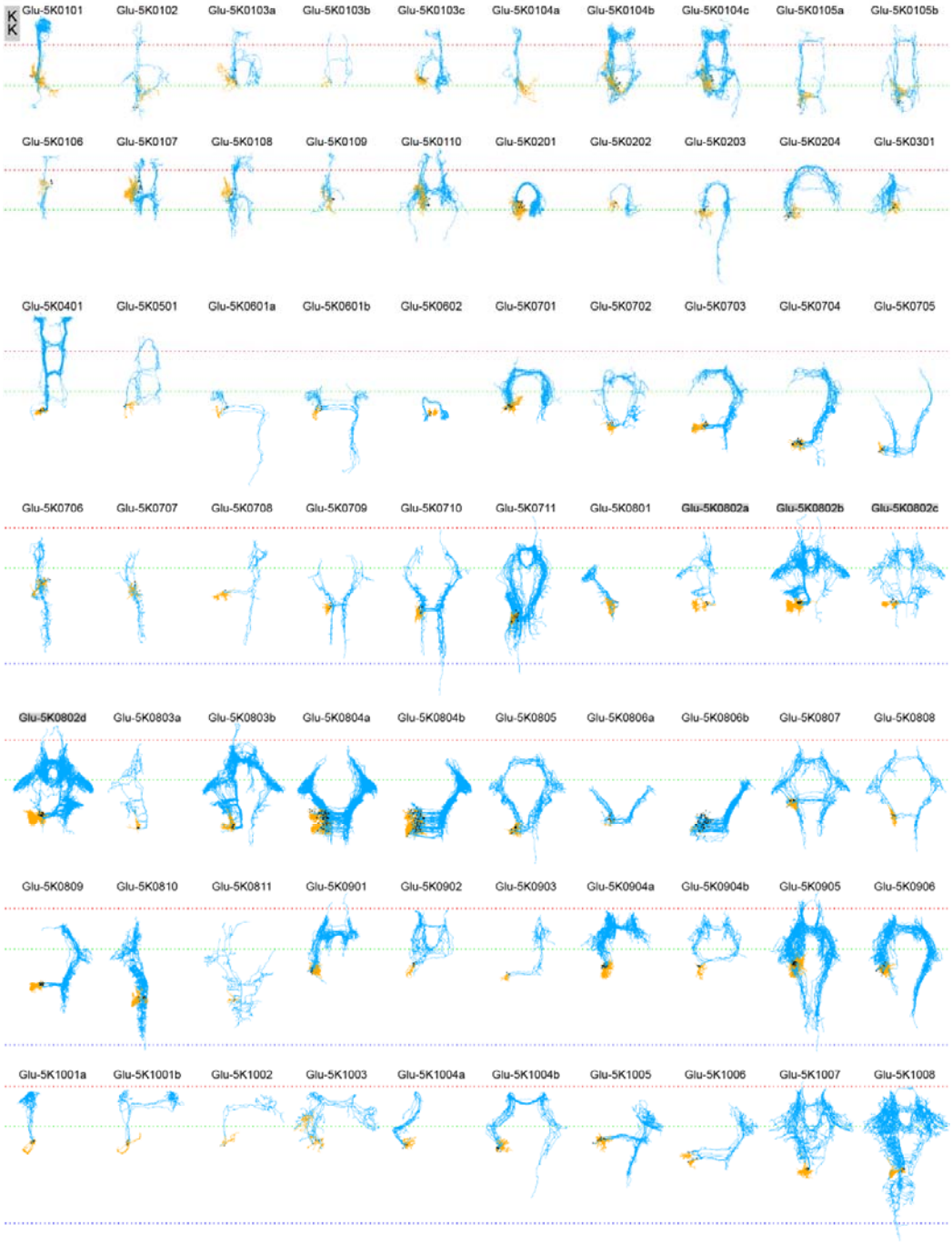
KK
Glu-5K0101
Glu-5K0102
Glu-5K0103a
Glu-5K0103b
Glu-5K0103c
Glu-5K0104a
Glu-5K0104b
Glu-5K0104c
Glu-5K0105a
Glu-5K0105b
Glu-5K0106
Glu-5K0107
Glu-5K0108
Glu-5K0109
Glu-5K0110
Glu-5K0201
Glu-5K0202
Glu-5K0203
Glu-5K0204
Glu-5K0301
Glu-5K0401
Glu-5K0501
Glu-5K0601a
Glu-5K0601b
Glu-5K0602
Glu-5K0701
Glu-5K0702
Glu-5K0703
Glu-5K0704
Glu-5K0705
Glu-5K0706
Glu-5K0707
Glu-5K0708
Glu-5K0709
Glu-5K0710
Glu-5K0711
Glu-5K0801
Glu-5K0802a
Glu-5K0802b
Glu-5K0802c
Glu-5K0802d
Glu-5K0803a
Glu-5K0803b
Glu-5K0804a
Glu-5K0804b
Glu-5K0805
Glu-5K0806a
Glu-5K0806b
Glu-5K0807
Glu-5K0808
Glu-5K0809
Glu-5K0810
Glu-5K0811
Glu-5K0901
Glu-5K0902
Glu-5K0903
Glu-5K0904a
Glu-5K0904b
Glu-5K0905
Glu-5K0906
Glu-5K1001a
Glu-5K1001b
Glu-5K1002
Glu-5K1003
Glu-5K1004a
Glu-5K1004b
Glu-5K1005
Glu-5K1006
Glu-5K1007
Glu-5K1008

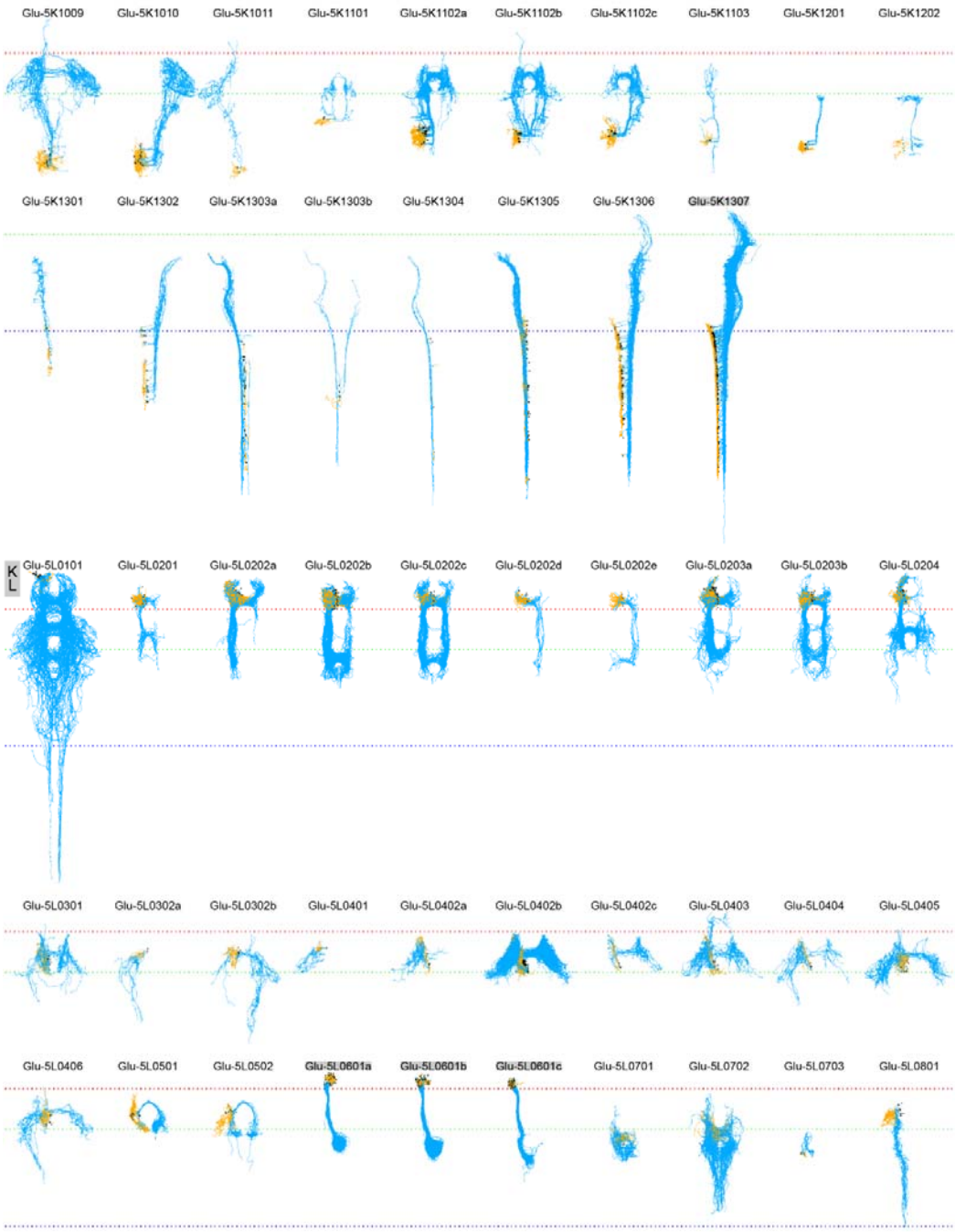
Glu-5K1009
Glu-5K1010
Glu-5K1011
Glu-5K1101
Glu-5K1102a
Glu-5K1102b
Glu-5K1102c
Glu-5K1103
Glu-5K1201
Glu-5K1202
Glu-5K1301
Glu-5K1302
Glu-5K1303a
Glu-5K1303b
Glu-5K1304
Glu-5K1305
Glu-5K1306
Glu-5K1307
K
L
Glu-5L0101
Glu-5L0201
Glu-5L0202a
Glu-5L0202b
Glu-5L0202c
Glu-5L0202d
Glu-5L0202e
Glu-5L0203a
Glu-5L0203b
Glu-5L0204
Glu-5L0301
Glu-5L0302a
Glu-5L0302b
Glu-5L0401
Glu-5L0402a
Glu-5L0402b
Glu-5L0402c
Glu-5L0403
Glu-5L0404
Glu-5L0405
Glu-5L0406
Glu-5L0501
Glu-5L0502
Glu-5L0601a
Glu-5L0601b
Glu-5L0601c
Glu-5L0701
Glu-5L0702
Glu-5L0703
Glu-5L0801

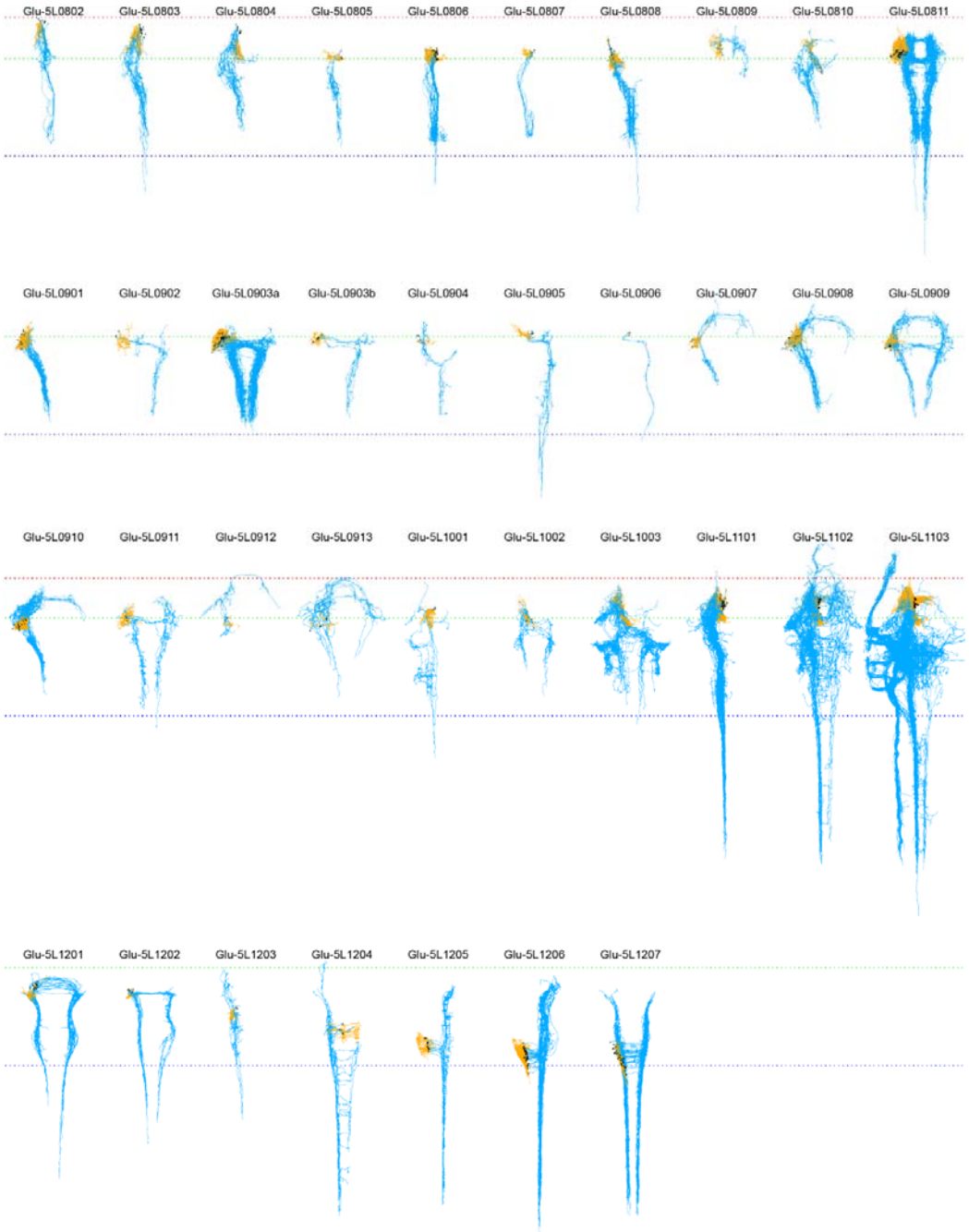
Glu-5L0802
Glu-5L0803
Glu-5L0804
Glu-5L0805
Glu-5L0806
Glu-5L0807
Glu-5L0808
Glu-5L0809
Glu-5L0810
Glu-5L0811
Glu-5L0901
Glu-5L0902
Glu-5L0903a
Glu-5L0903b
Glu-5L0904
Glu-5L0905
Glu-5L0906
Glu-5L0907
Glu-5L0908
Glu-5L0909
Glu-5L0910
Glu-5L0911
Glu-5L0912
Glu-5L0913
Glu-5L1001
Glu-5L1002
Glu-5L1003
Glu-5L1101
Glu-5L1102
Glu-5L1103
Glu-5L1201
Glu-5L1202
Glu-5L1203
Glu-5L1204
Glu-5L1205
Glu-5L1206
Glu-5L1207

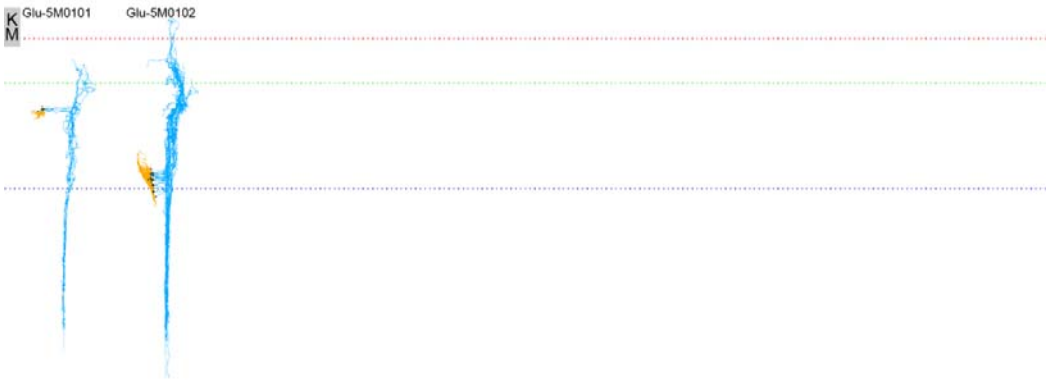
KM
Glu-5M0101
Glu-5M0102

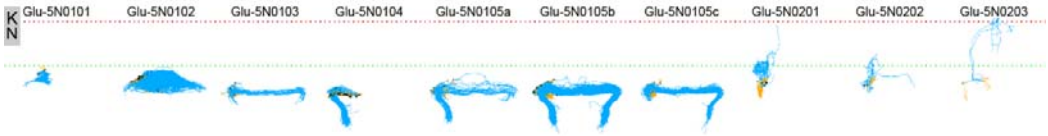
KN
Glu-5N0101
Glu-5N0102
Glu-5N0103
Glu-5N0104
Glu-5N0105a
Glu-5N0105b
Glu-5N0105c
Glu-5N0201
Glu-5N0202
Glu-5N0203

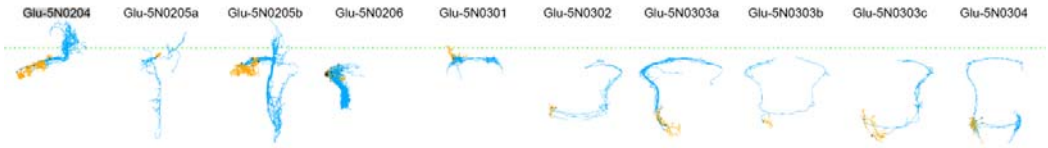
Glu-5N0204
Glu-5N0205a
Glu-5N0205b
Glu-5N0206
Glu-5N0301
Glu-5N0302
Glu-5N0303a
Glu-5N0303b
Glu-5N0303c
Glu-5N0304

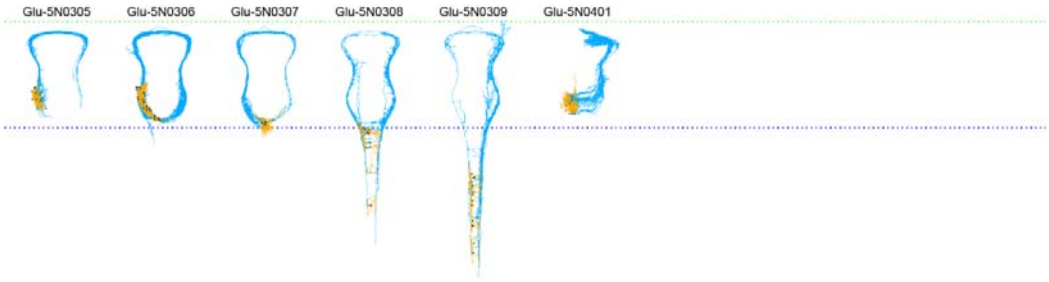
Glu-5N0305
Glu-5N0306
Glu-5N0307
Glu-5N0308
Glu-5N0309
Glu-5N0401

b

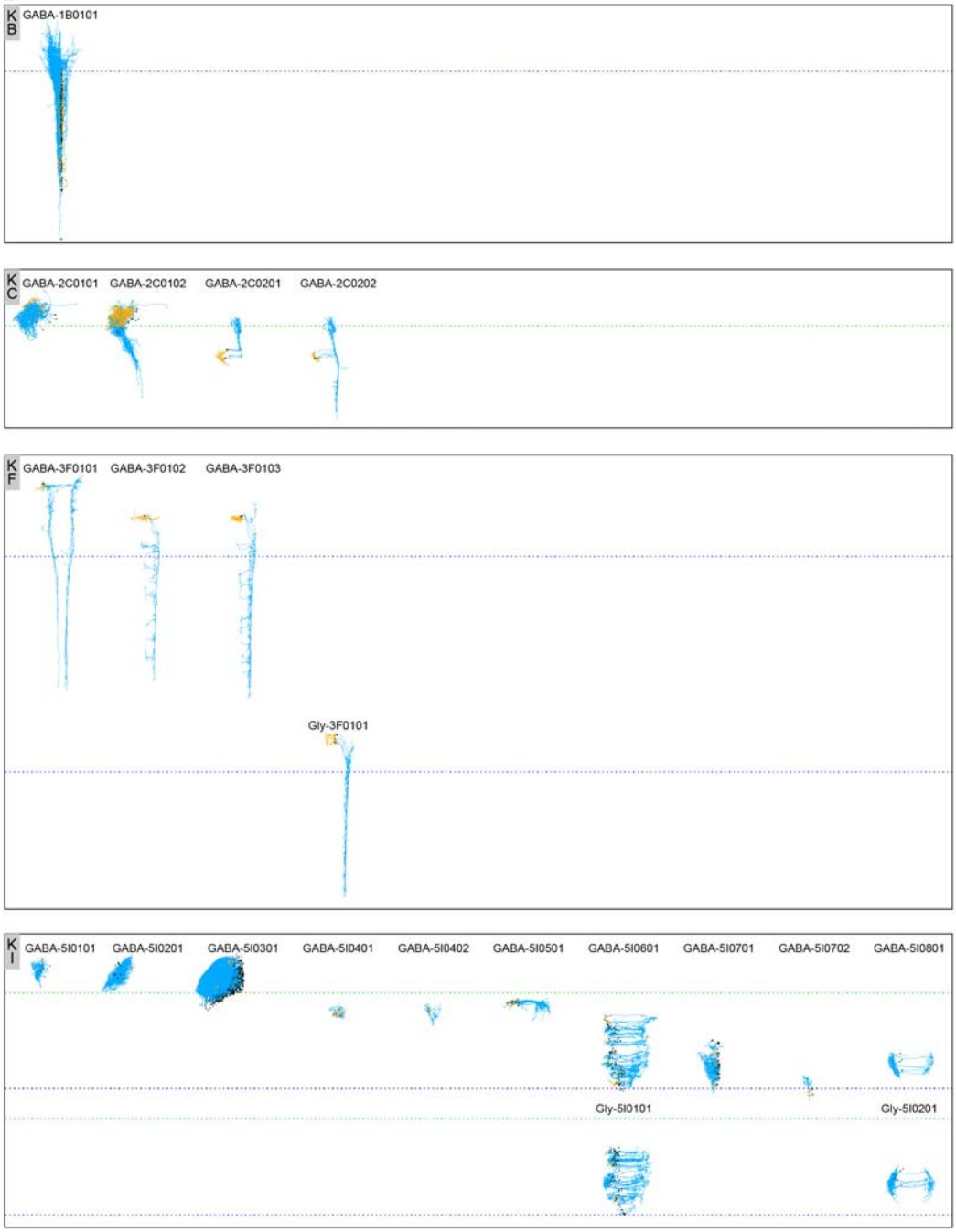
KB
GABA-1B0101
KC
GABA-2C0101
GABA-2C0102
GABA-2C0201
GABA-2C0202
KF
GABA-3F0101
GABA-3F0102
GABA-3F0103
Gly-3F0101
KI
GABA-5I0101
GABA-5I0201
GABA-5I0301
GABA-5I0401
GABA-5I0402
GABA-5I0501
GABA-5I0601
GABA-5I0701
GABA-5I0702
GABA-5I0801
Gly-5I0101
Gly-5I0201

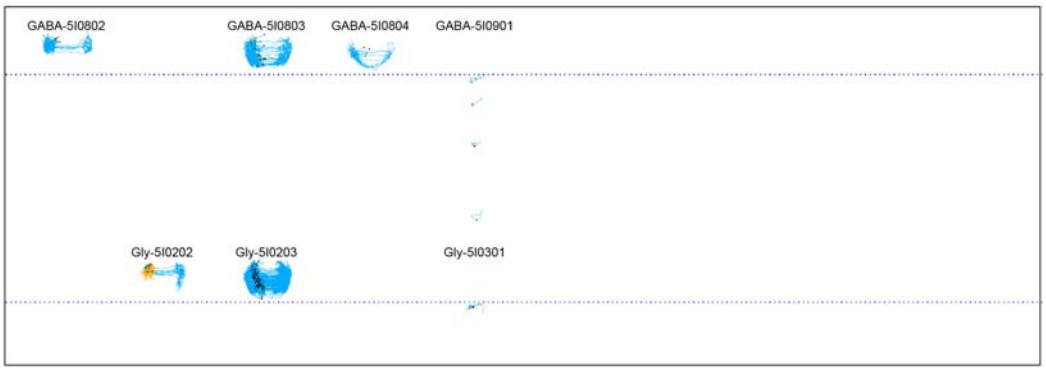
GABA-5I0802
GABA-5I0803
GABA-5I0804
GABA-5I0901
Gly-5I0202
Gly-5I0203
Gly-5I0301

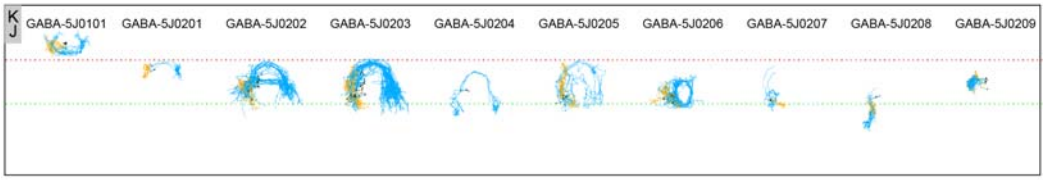
K
J
GABA-5J0101
GABA-5J0201
GABA-5J0202
GABA-5J0203
GABA-5J0204
GABA-5J0205
GABA-5J0206
GABA-5J0207
GABA-5J0208
GABA-5J0209

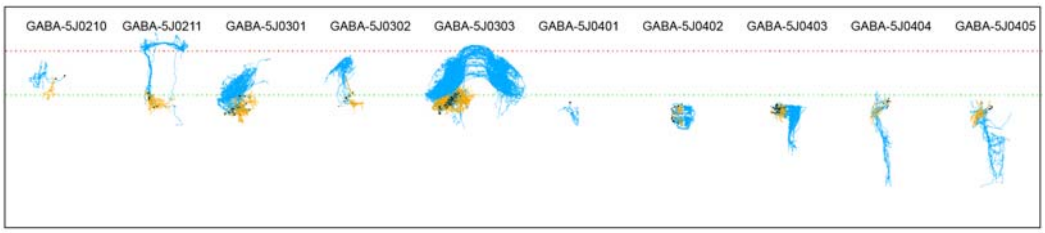
GABA-5J0210
GABA-5J0211
GABA-5J0301
GABA-5J0302
GABA-5J0303
GABA-5J0401
GABA-5J0402
GABA-5J0403
GABA-5J0404
GABA-5J0405

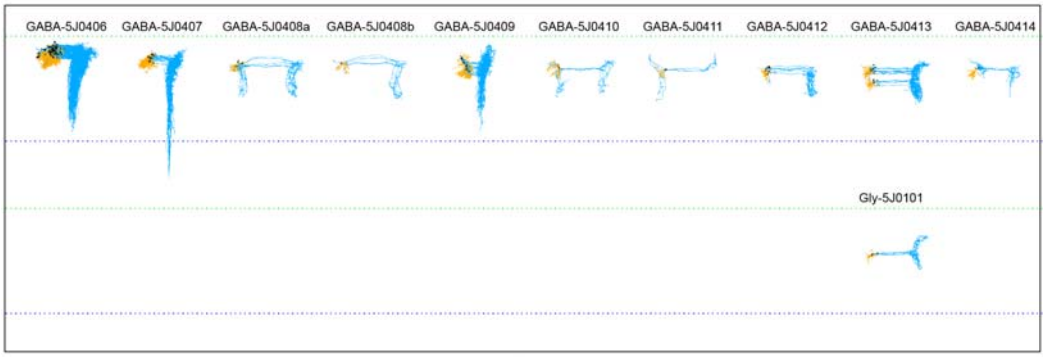
GABA-5J0406
GABA-5J0407
GABA-5J0408a
GABA-5J0408b
GABA-5J0409
GABA-5J0410
GABA-5J0411
GABA-5J0412
GABA-5J0413
GABA-5J0414
Gly-5J0101

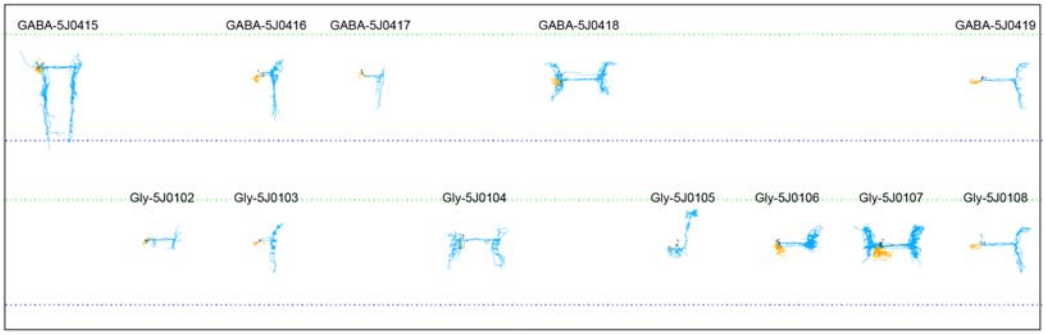
GABA-5J0415
GABA-5J0416
GABA-5J0417
GABA-5J0418
GABA-5J0419
Gly-5J0102
Gly-5J0103
Gly-5J0104
Gly-5J0105
Gly-5J0106
Gly-5J0107
Gly-5J0108

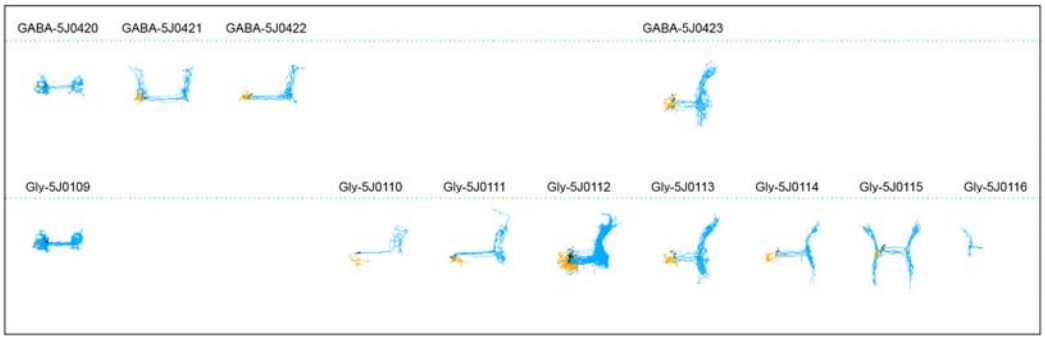
GABA-5J0420
GABA-5J0421
GABA-5J0422
GABA-5J0423
Gly-5J0109
Gly-5J0110
Gly-5J0111
Gly-5J0112
Gly-5J0113
Gly-5J0114
Gly-5J0115
Gly-5J0116

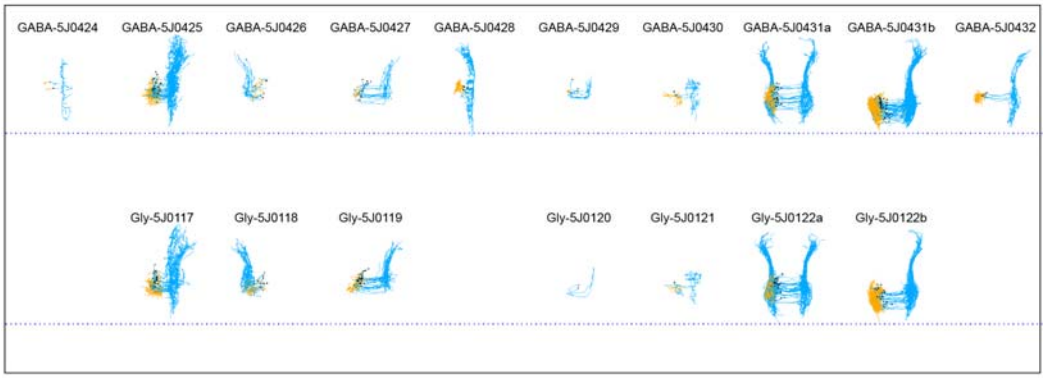
GABA-5J0424
GABA-5J0425
GABA-5J0426
GABA-5J0427
GABA-5J0428
GABA-5J0429
GABA-5J0430
GABA-5J0431a
GABA-5J0431b
GABA-5J0432
Gly-5J0117
Gly-5J0118
Gly-5J0119
Gly-5J0120
Gly-5J0121
Gly-5J0122a
Gly-5J0122b

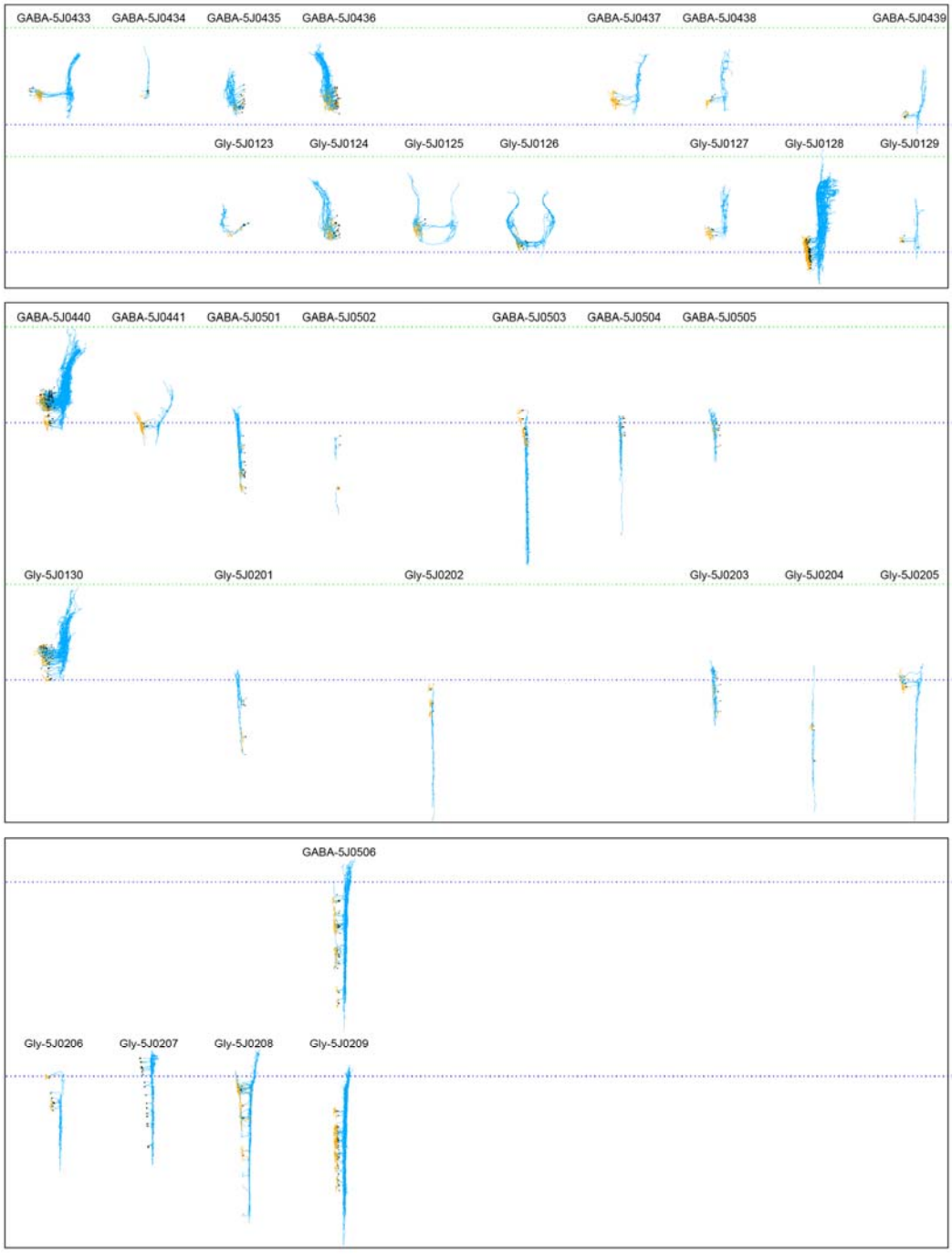
GABA-5J0433
GABA-5J0434
GABA-5J0435
GABA-5J0436
GABA-5J0437
GABA-5J0438
GABA-5J0439
Gly-5J0123
Gly-5J0124
Gly-5J0125
Gly-5J0126
Gly-5J0127
Gly-5J0128
Gly-5J0129
GABA-5J0440
GABA-5J0441
GABA-5J0501
GABA-5J0502
GABA-5J0503
GABA-5J0504
GABA-5J0505
Gly-5J0130
Gly-5J0201
Gly-5J0202
Gly-5J0203
Gly-5J0204
Gly-5J0205
GABA-5J0506
Gly-5J0206
Gly-5J0207
Gly-5J0208
Gly-5J0209

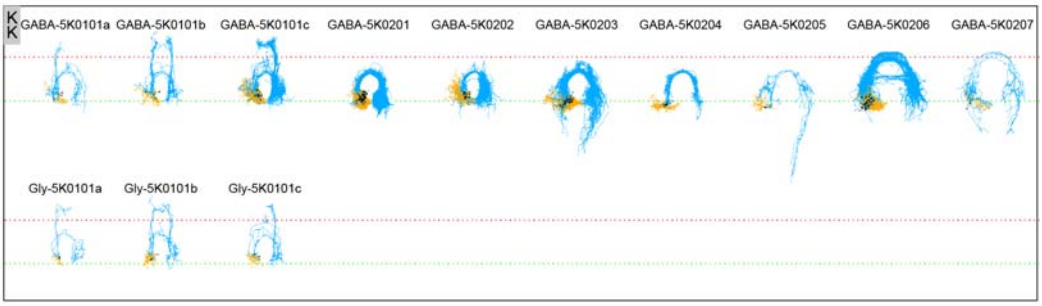
KK
GABA-5K0101a
GABA-5K0101b
GABA-5K0101c
GABA-5K0201
GABA-5K0202
GABA-5K0203
GABA-5K0204
GABA-5K0205
GABA-5K0206
GABA-5K0207
Gly-5K0101a
Gly-5K0101b
Gly-5K0101c

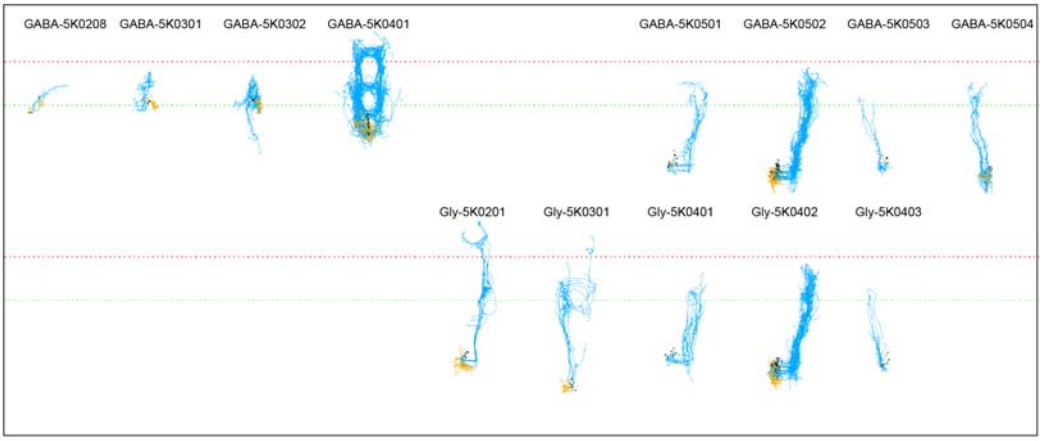
GABA-5K0208
GABA-5K0301
GABA-5K0302
GABA-5K0401
GABA-5K0501
GABA-5K0502
GABA-5K0503
GABA-5K0504
Gly-5K0201
Gly-5K0301
Gly-5K0401
Gly-5K0402
Gly-5K0403

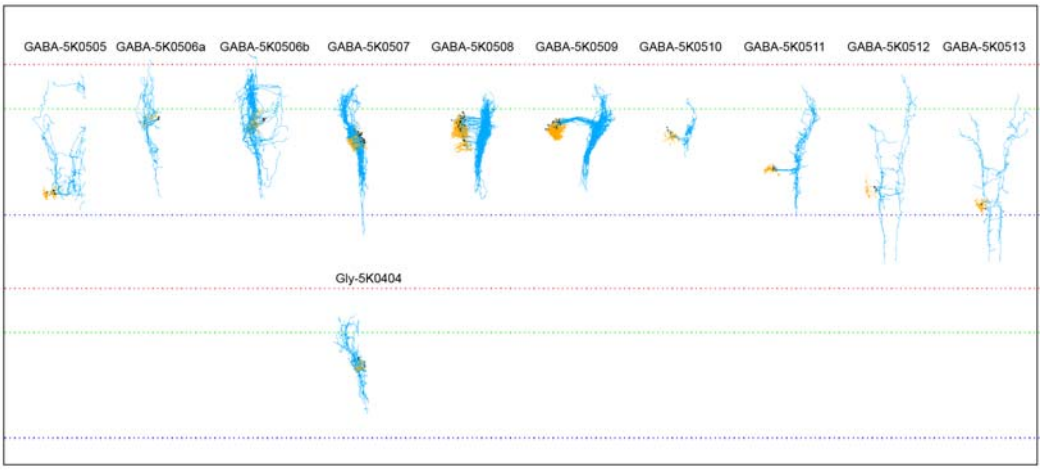
GABA-5K0505
GABA-5K0506a
GABA-5K0506b
GABA-5K0507
GABA-5K0508
GABA-5K0509
GABA-5K0510
GABA-5K0511
GABA-5K0512
GABA-5K0513
Gly-5K0404

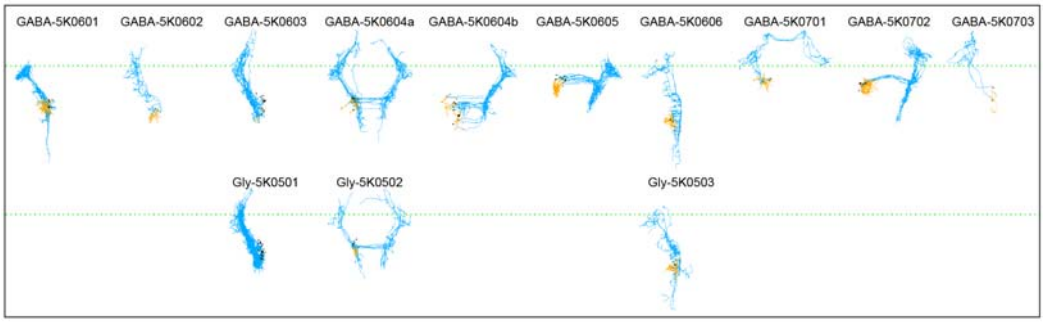
GABA-5K0601
GABA-5K0602
GABA-5K0603
GABA-5K0604a
GABA-5K0604b
GABA-5K0605
GABA-5K0606
GABA-5K0701
GABA-5K0702
GABA-5K0703
Gly-5K0501
Gly-5K0502
Gly-5K0503

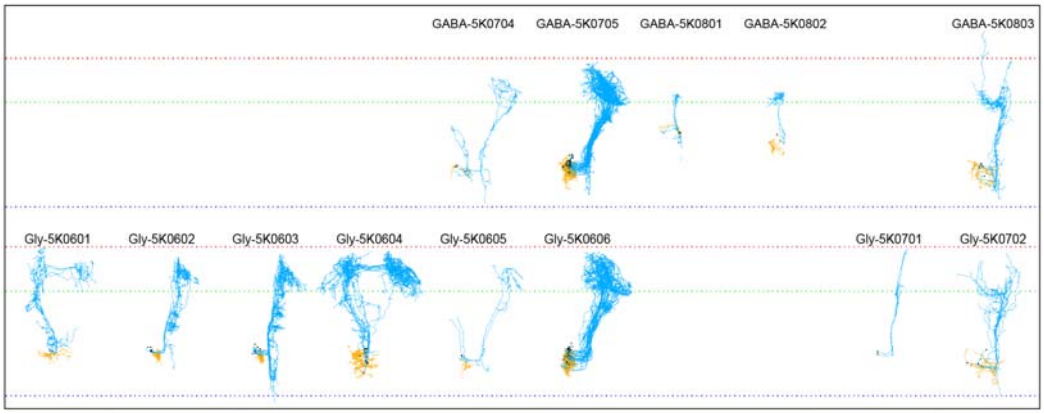
GABA-5K0704
GABA-5K0705
GABA-5K0801
GABA-5K0802
GABA-5K0803
Gly-5K0601
Gly-5K0602
Gly-5K0603
Gly-5K0604
Gly-5K0605
Gly-5K0606
Gly-5K0701
Gly-5K0702

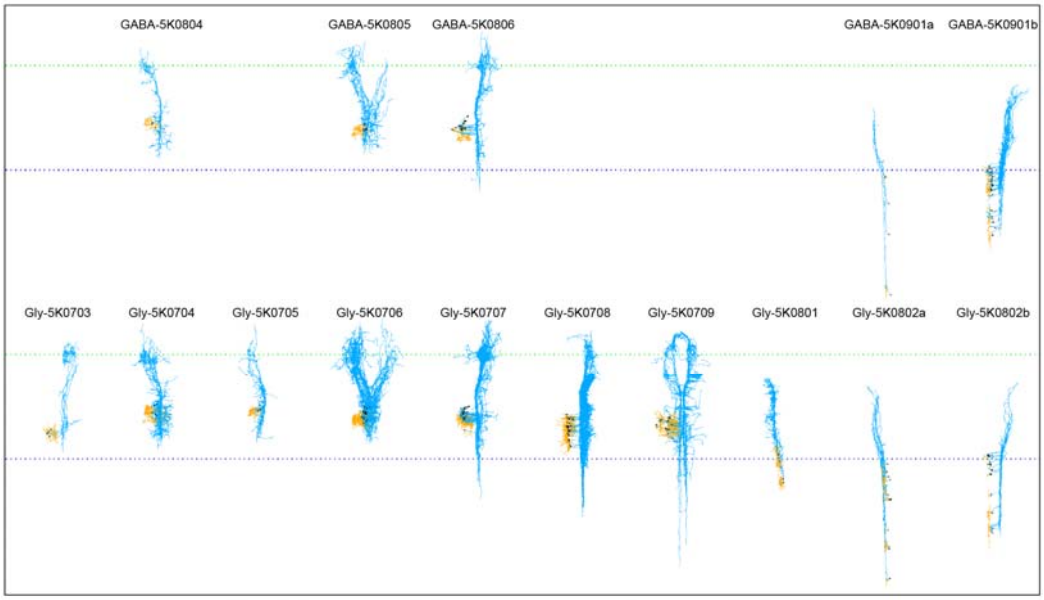
GABA-5K0804
GABA-5K0805
GABA-5K0806
GABA-5K0901a
GABA-5K0901b
Gly-5K0703
Gly-5K0704
Gly-5K0705
Gly-5K0706
Gly-5K0707
Gly-5K0708
Gly-5K0709
Gly-5K0801
Gly-5K0802a
Gly-5K0802b

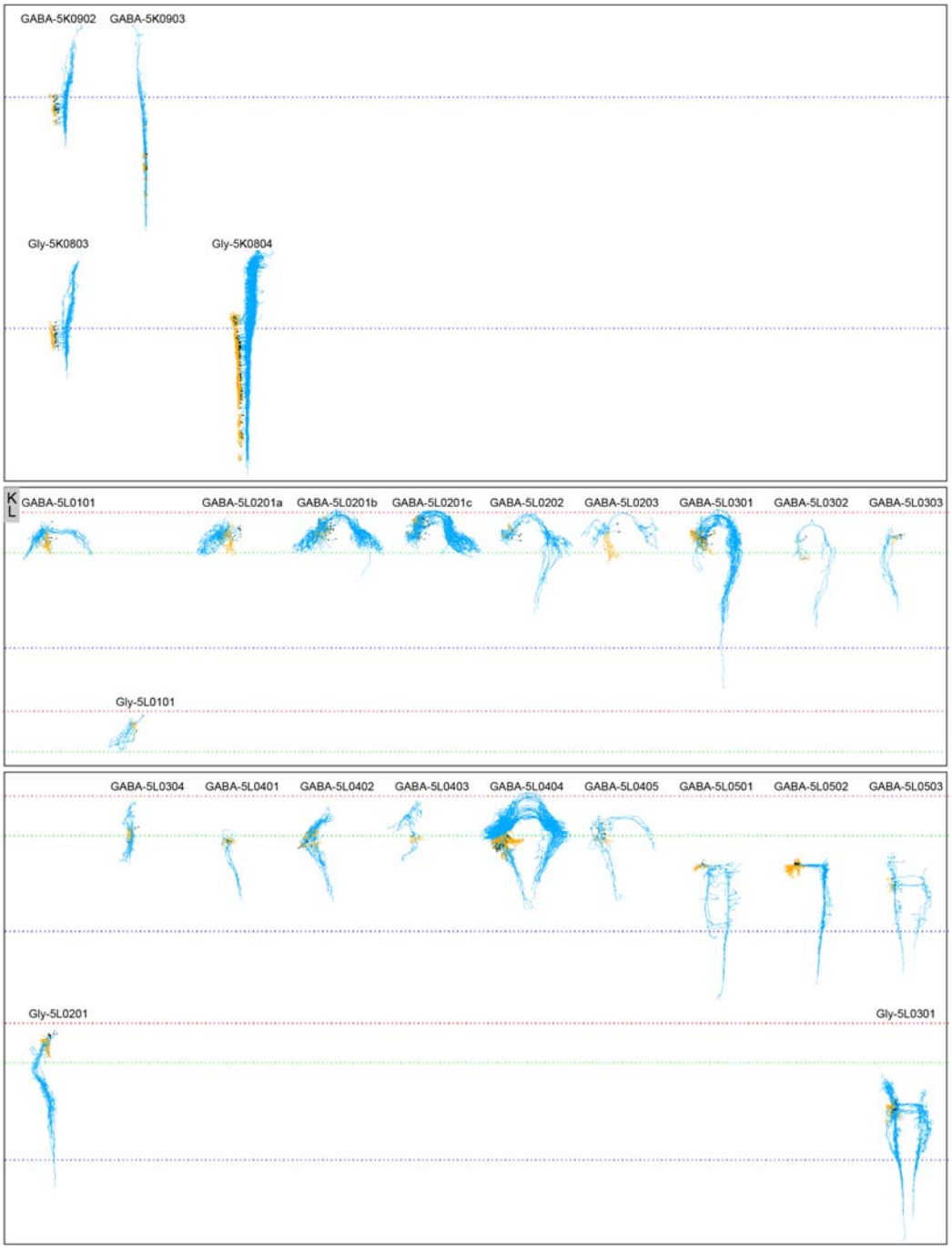
GABA-5K0902
GABA-5K0903
Gly-5K0803
Gly-5K0804
KL
GABA-5L0101
GABA-5L0201a
GABA-5L0201b
GABA-5L0201c
GABA-5L0202
GABA-5L0203
GABA-5L0301
GABA-5L0302
GABA-5L0303
Gly-5L0101
GABA-5L0304
GABA-5L0401
GABA-5L0402
GABA-5L0403
GABA-5L0404
GABA-5L0405
GABA-5L0501
GABA-5L0502
GABA-5L0503
Gly-5L0201
Gly-5L0301

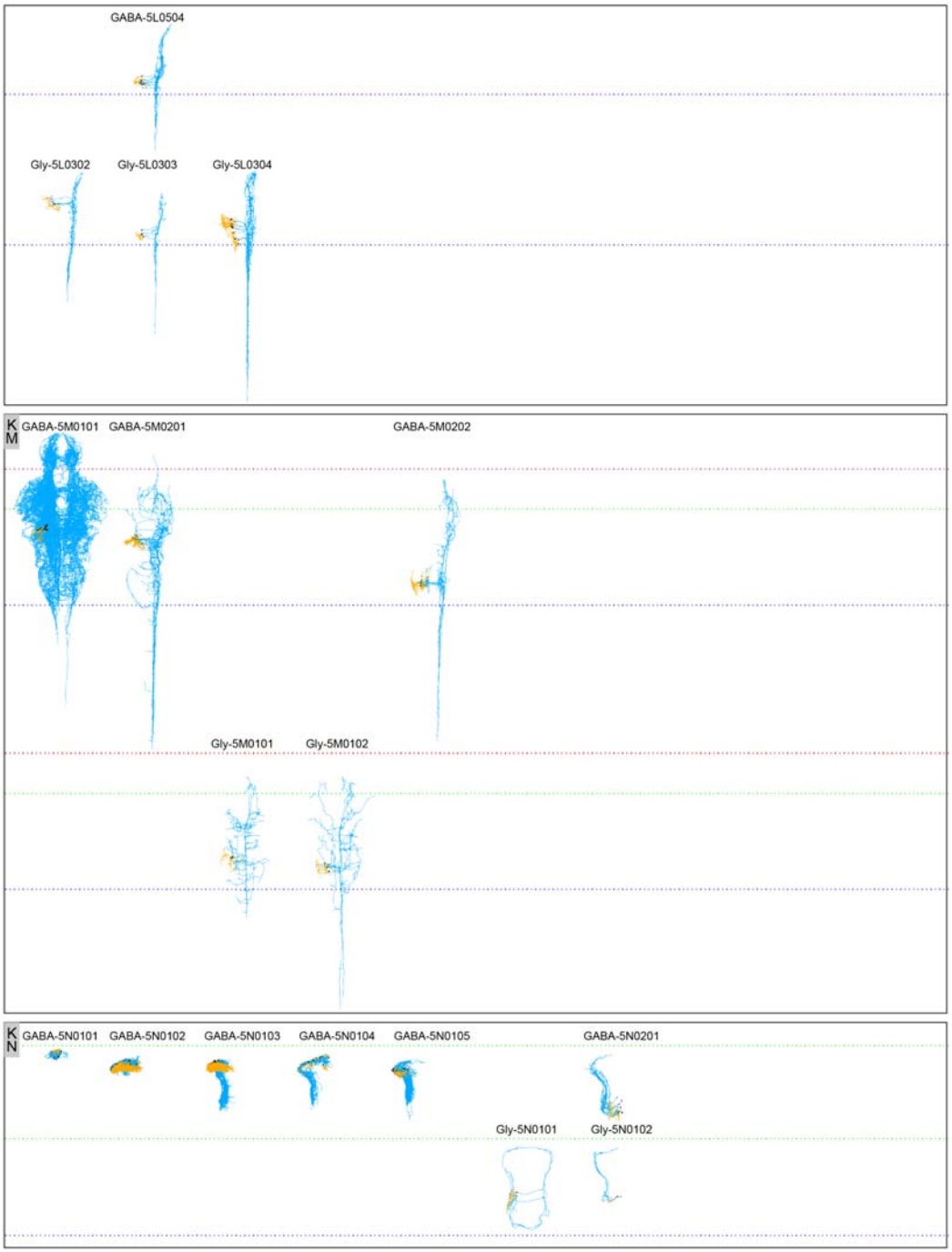

Extended Data Fig. 6 | Overview of E and I morphotypes.

a,**b**, Volume rendering (dorsal view) of 348 excitatory (**a**), 164 GABAergic, and 88 glycinergic inhibitory (**b**) morphological subtypes displayed in ontological order. In **b**, GABAergic and glycinergic neurons are displayed in alternating rows, with vertically aligned positions indicating corresponding inhibitory morphotypes used to generate the inter-cell-type connectome shown in Fig. 7 and Extended Data Fig. 9. Each subtype ID (up to 11 characters) encodes its neurotransmitter identity, division (1–5), category (A–N), class (two-digit numbers), type (two-digit numbers), and subtype (a lowercase letter). Morphotypes used for

dendrite-axon classification accuracy assessment (see Results) are indicated with a gray background in the ID.

Scale bar: 100 μm. KA–KN denote 14 categories. A, anterior; V, ventral. HSB, hindbrain-spinal cord boundary; MHB, midbrain-hindbrain boundary; TDB, telencephalon-diencephalon boundary.

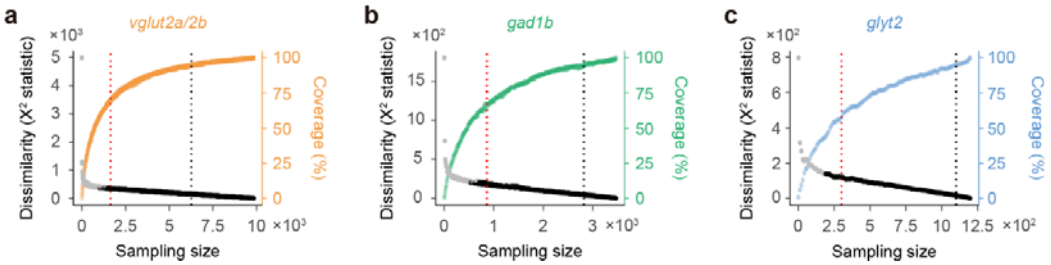

Extended Data Fig. 7 | Assessment of cell type coverage.

a-c, Scatterplot showing the cell type distribution dissimilarity (left *y*-axis; gray dots, $P < 0.05$; black dots, $P > 0.05$; maximum X^2 statistic) between randomly sampled and full classified populations, and the cell type coverage (right *y*-axis, color-coded dots, minimum value), based on 1000 randomly selected cell groups. Sampling sizes with a 10-cell step range from 1 to the total classified cells for *vglut2a/2b* (**a**, 9,774 neurons), *gad1b* (**b**, 3,411 neurons), and *glyt2* (**c**, 1,116 neurons) populations. Dashed red line, sampling size at the breakpoint; dashed black line, sampling size at which 95% cell type coverage is reached.

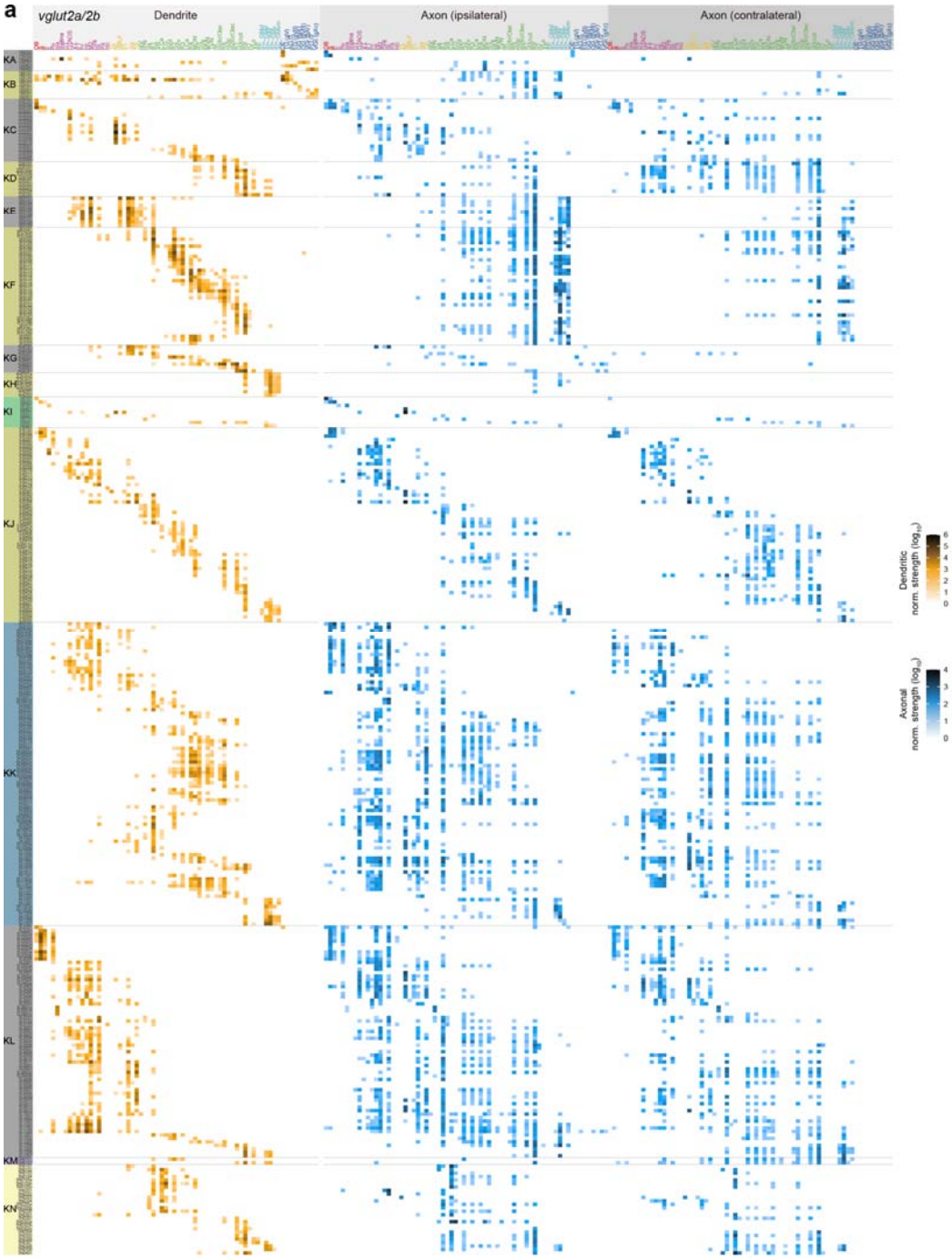
a
vglut2a/2b
Dendrite
Axon (ipsilateral)
Axon (contralateral)
KA
KB
KC
KD
KE
KF
KG
KH
KI
KJ
KK
KL
KM
KN
Dendritic norm. strength (log10)
Axonal norm. strength (log10)

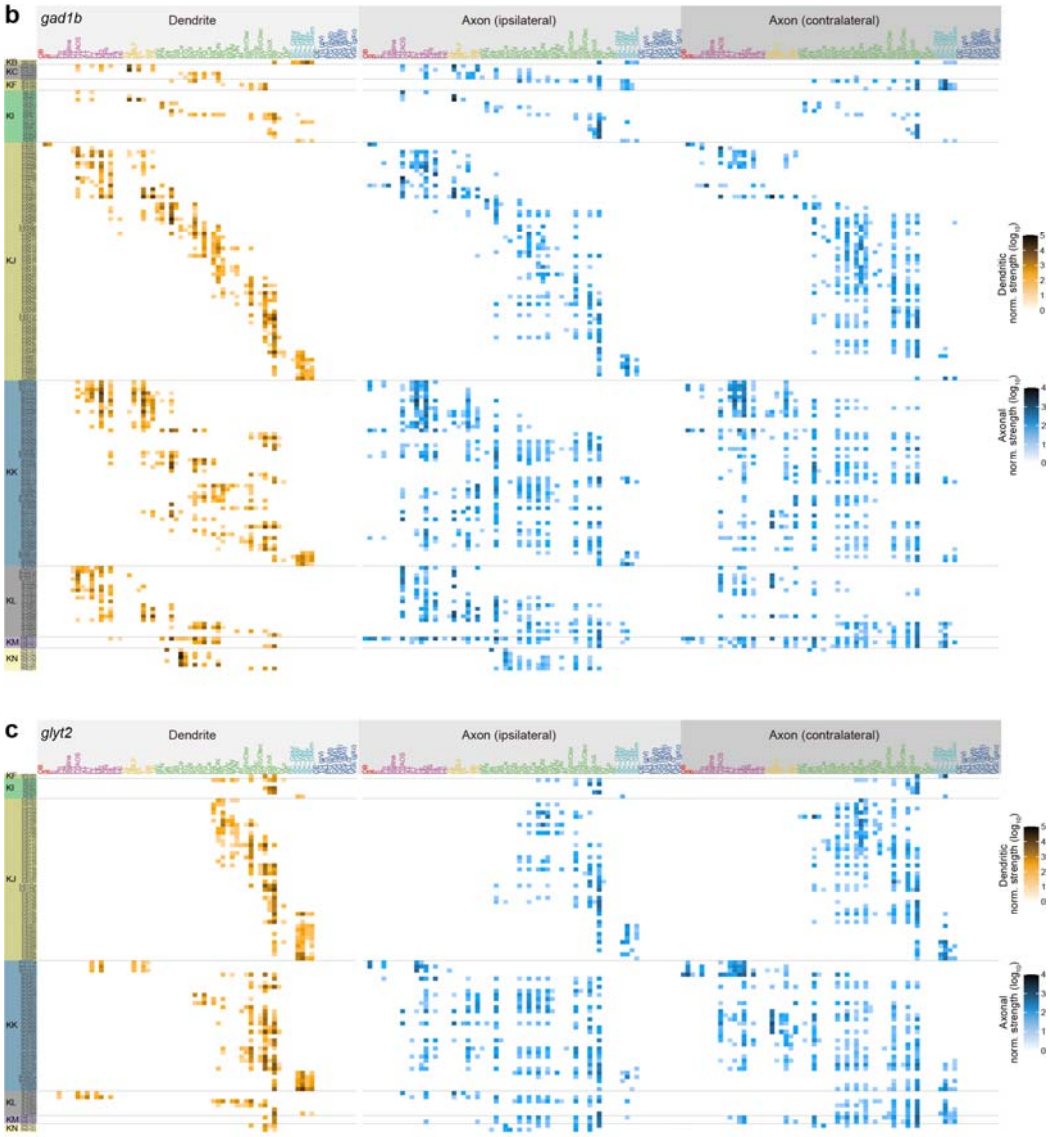

Extended Data Fig. 8 | Dendritic recipient and axonal projection matrices of E and I morphological subtypes.

a–**c**, Quantitative recipient (left), ipsilateral projection (middle), and contralateral projection (right) strengths of each morphological subtype in *vglut2a/2b* (**a**, 348 subtypes), *gad1b* (**b**, 164 subtypes), and *glyt2* (**c**, 88 subtypes) neurons across 68 anatomical regions. Regions are ordered by primary subdivision (Tel, Di, M, H, SC) and then by anteroposterior centroid. Morphotypes are displayed in ontological order, and KA–KN indicate 14 categories. Matrices show $\log_{10}$-transformed strengths normalized by the number of cells.

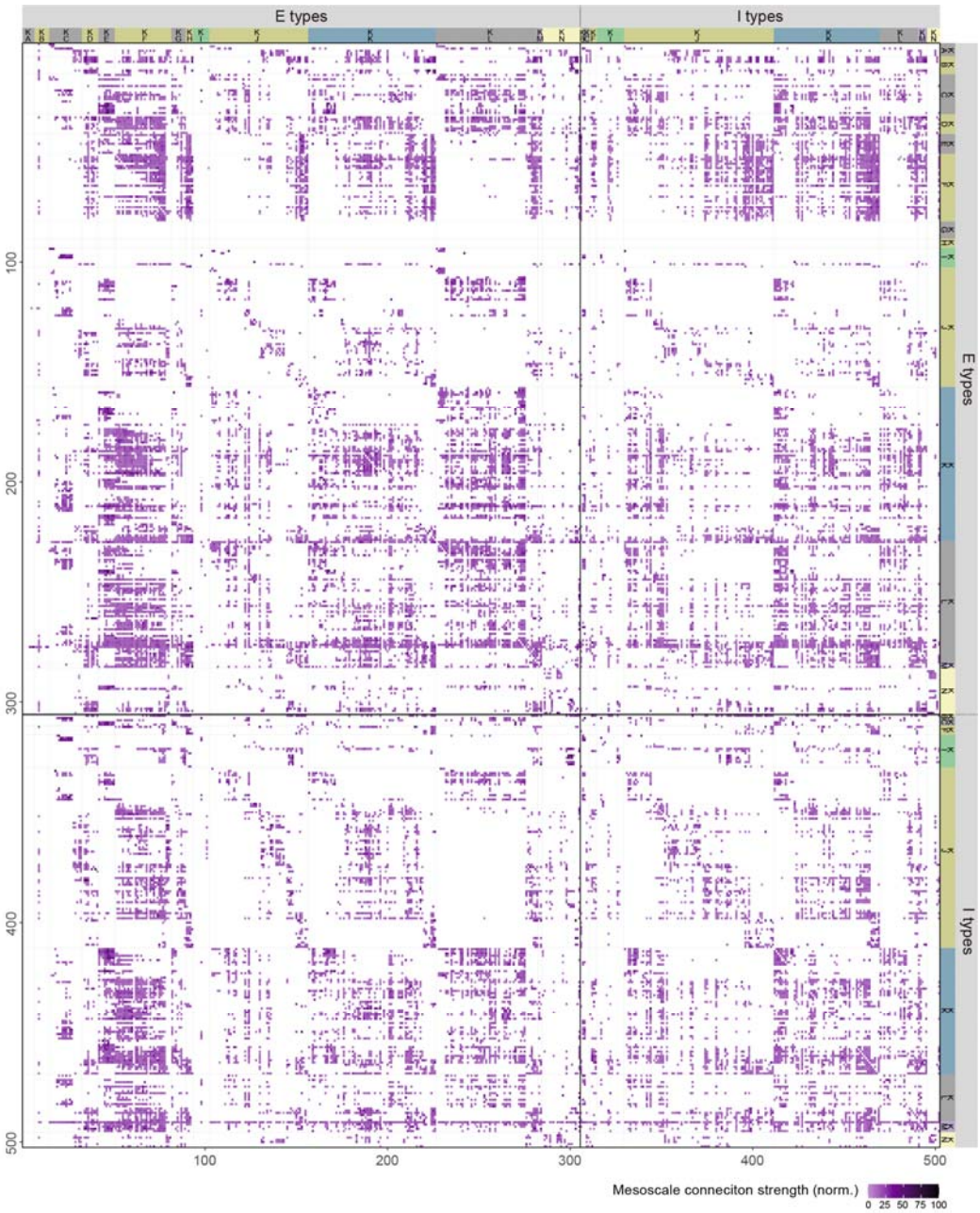

Extended Data Fig. 9 | Inter-cell-type mesoscale connectivity matrix.

Directed and weighted connection strengths between 502 types, displayed by E and I groups and in ontological order (n_E = 305, n_I = 197). Matrix values represent the pairwise mesoscale connection strength from row to column types, normalized by the number of connected neuron pairs. Connections were filtered by requiring neuronal participation ≥20% in at least one member of each connected morphotype pair, and both divergence and convergence indices >1, resulting in 33,660 directed connections

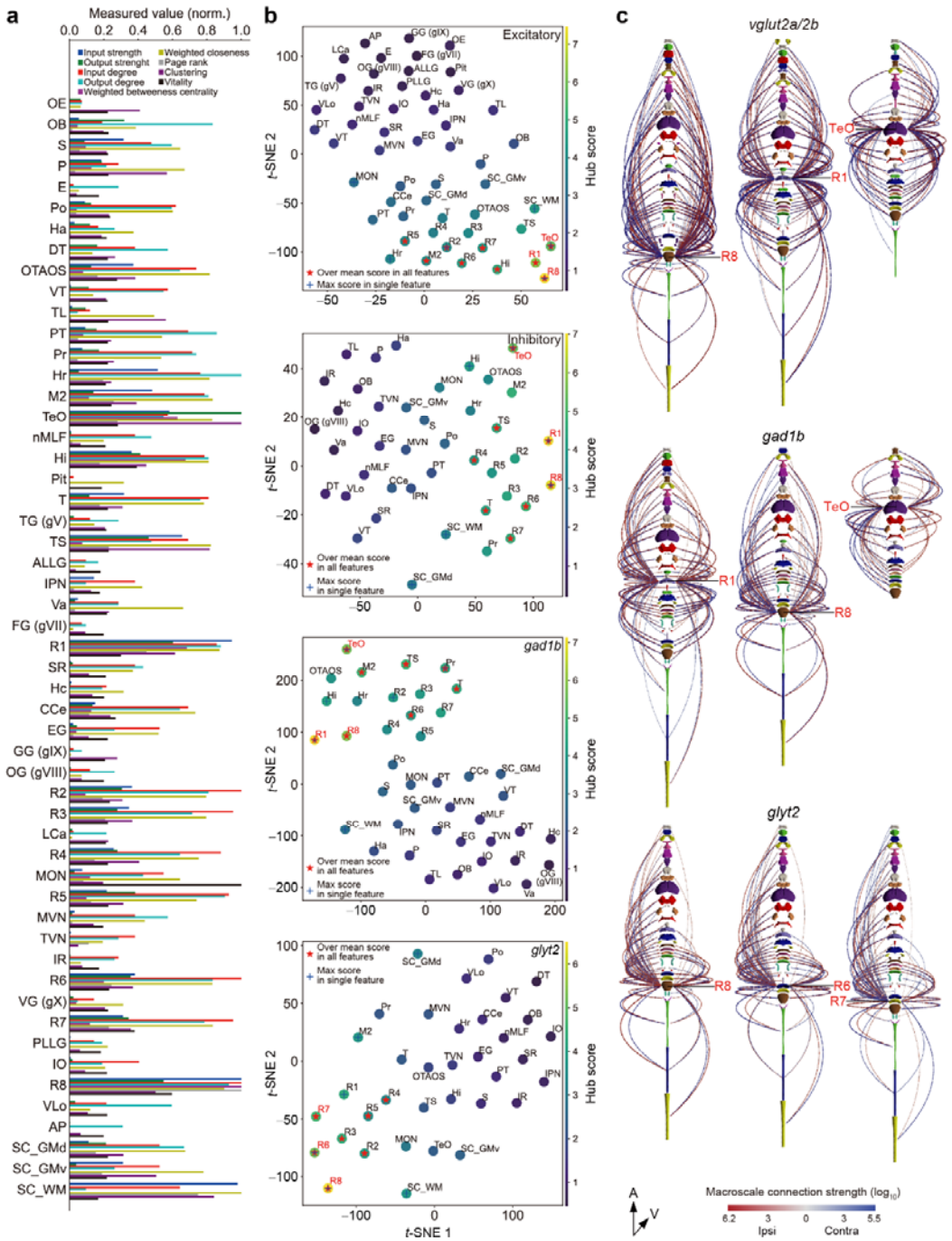

Extended Data Fig. 10 | Analysis of hubs in the interregional network.

a, Nine network metrics, including input strength, output strength, input degree, output degree, weighted betweenness centrality, weighted closeness, page rank, clustering, and vitality. Only E network-relevant data are shown.

b, t-SNE plots of regions, based on the nine network metrics. Top, E (*vglut2a/2b*); upper middle, I (*gad1b* and *glyt2*); lower middle, *gad1b*; bottom, *glyt2*. Perplexity = 20. Regions are color-coded by hub score. Red star indicates hub regions with above-mean values across all metrics, and blue crosses mark regions with the highest score in any single metric (with

overlaps across some metrics). The top three hub regions (highest overall hub scores) are labeled in red.

c, Regional input-output diagrams of the top three hub regions for *vglut2a/2b* (top; R8, R1, and TeO), *gad1b* (middle; R1, R8, and TeO), and *glyt2* (bottom; R8, R6, and R7) neuron networks. Parabolas represent directed ipsilateral (red) and contralateral (blue) connections between regions, which are arranged linearly based on their anteroposterior centroid coordinates. Right parabolas indicate descending connections, while left parabolas indicate ascending connections. The parabola's height and color tone both represent macroscale connection strength. A, anterior; V, ventral.

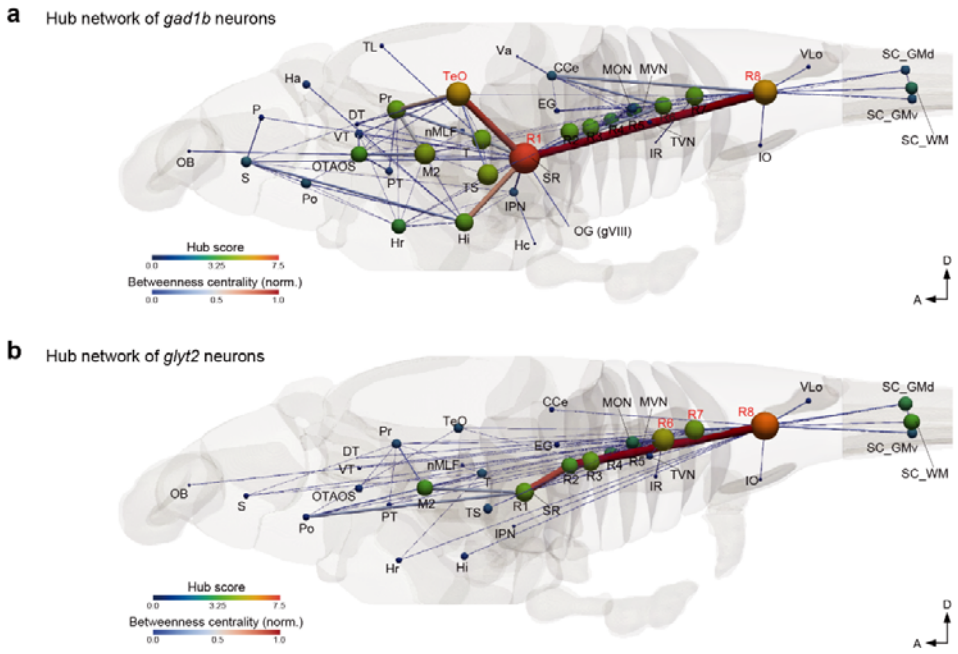

Extended Data Fig. 11 | Analysis of network hubs and information flow in the interregional network.

a,**b**, Inhibitory hub networks constructed from *gad1b* (**a**) or *glyt2* (**b**) neurons. Each node (sphere) represents one of 53 regions (retina excluded), with its color and size indicating its hub score. The color and width (normalized betweenness centrality) of the edge both reflect its importance in the information flow among regions. The names of the top three hub regions are in red. A, anterior; D, dorsal.

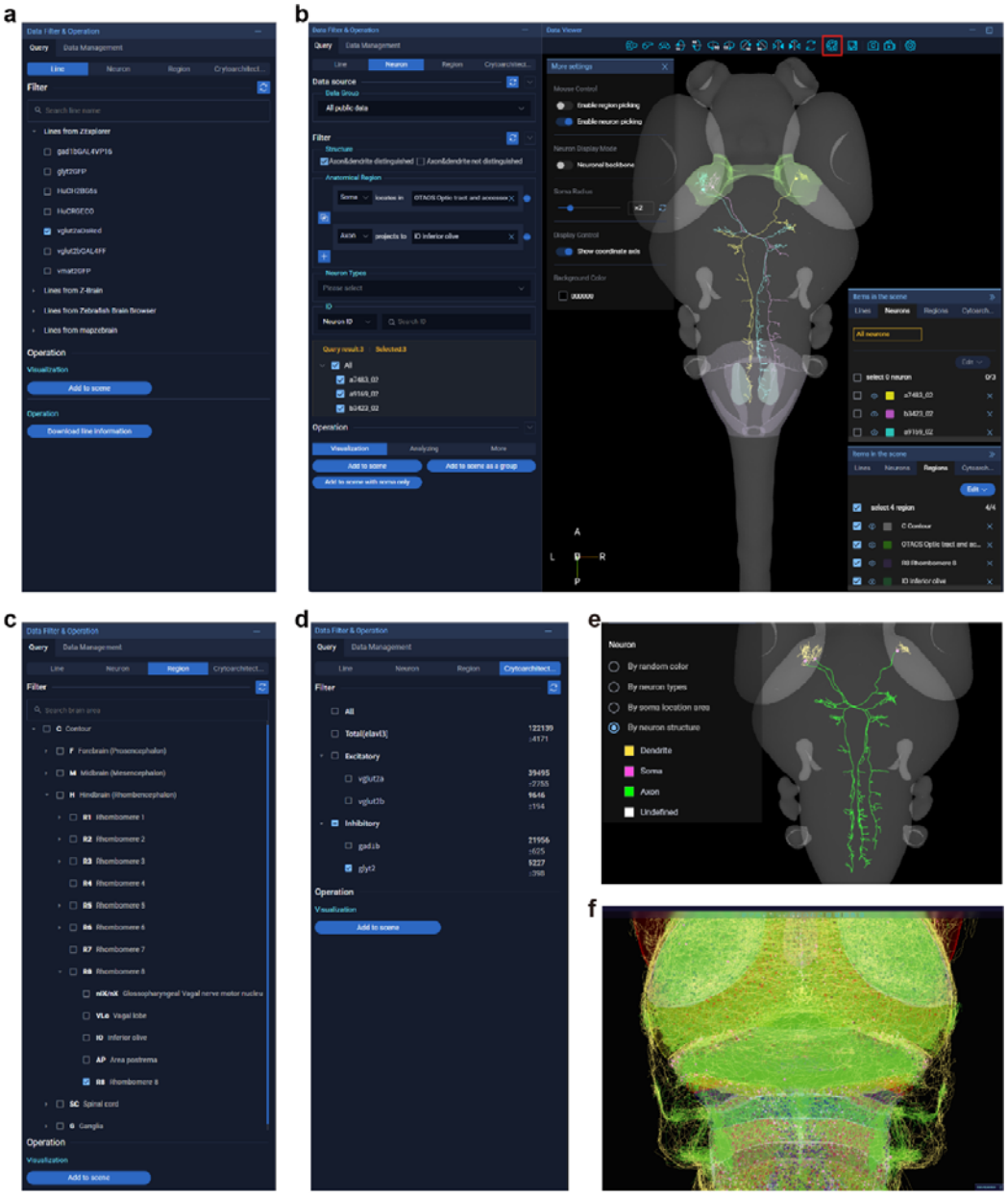

Extended Data Fig. 12 | A web portal for exploring all datasets in the CPS.

a, Interactive panel for selecting aligned line image datasets from ZExplorer, Z-Brain, ZBB, and mapzebrain to display in the 3D viewer.

b, Interactive panel for selecting interested neuron tracings (left) and corresponding 3D view showing both tracings and anatomical regions (right). Users can query neurons based on soma and axon position using "overlap/exclude/AND" operations, and adjust color or visibility for individual or grouped tracings using the "item in the scene" panel.

c, Interactive panel for selecting anatomical regions in the CPS to display in the 3D viewer.

d, Interactive panel for selecting cytoarchitecture data of specific cell types for visualization.

e, Neuron tracings visualized with different color schemes for cellular compartments (soma,

dendrite, axon; menu toggled by clicking the red-boxed icon in **b**).

f, Example of an integrated 3D view for the combination of >10,000 neuron tracings, brain regions, and cytoarchitectures of *vglut2a*, *vglut2b*, *gad1b*, and *glyt2* neurons.

See also https://zebrafish.cn/LM-Atlas/EI.